EFFECTIVE DOSE ENHANCEMENT USING GOLD AS A RADIATION SENSITIZER: A MONTE CARLO STUDY

BY

NABEEL GARGANO AHMED

THESIS

Submitted in partial fulfillment of the requirements
for the degree of Master of Science in Nuclear, Plasma, and Radiological Engineering
in the Graduate College of the
University of Illinois at Urbana-Champaign, 2011

Urbana, Illinois

Master's Committee:

Associate Professor Magdi Ragheb, Chair
Assistant Professor Ling Jian Meng

ABSTRACT

Despite years of research, a significant gap remains between the cancer burden requiring treatment and the mechanisms currently available in clinical settings. Although great strides have been made in improving radiation therapy, the issue of non-specific irradiation of healthy tissue still persists. One of the most promising modalities currently being explored involves using contrast material to enhance the radiation sensitivity of a tumor. Such treatment aims to create a gradient in the photon attenuation coefficients of the tumor compared to those of the surrounding healthy tissue. The goal of generating such a variation is to dramatically increase the amount of effective dose received by the tumor without increasing the amount received by the surrounding healthy tissue. Several contrast materials have been explored for this application with iodine and gadolinium receiving generating significant interest. Following the promising results achieved by utilizing gold nanospheres in murine models, interest in gold has correspondingly increased.

This work examines several variables as they might pertain to the effectiveness of using gold as a radiation-sensitizing agent. Physical considerations involving the incident photon energy, geometric considerations involving the depth of the tumor, and concentration considerations involving the amount and distribution of gold around the tumor site have all been explored. Results were tabulated by comparing the amount of energy deposited per unit mass in the gold-bearing tumor volume compared to the surrounding healthy tissue and this ratio was termed the effective dose enhancement factor (DEF). Using a gold concentration of 7 mg per kg of tumor resulted in DEF values ranging from 62%, when a 100 keV photon beam was modeled, to less than 1%, when applying a 2 MeV photon beam. Varying the depth of tumor had less effect than expected as increasing the depth from 5 cm to 15 cm only increased the effective dose enhancement from 16% to 19% when using a 250 keV photon beam. Varying the in situ gold concentration had the most significant effect as expected and DEF values increased by a factor of four from 18% to 76% as concentration was increased from 7 mg/kg to 40 mg/kg. The results obtained from using a more detailed geometric and concentration

model and considering realistic distribution patterns may be of use when designing future in vivo studies. The results of the distribution and penetration models may be used to predict the effective dose profiles for tumor masses that are resistant to nanoparticle influx.

Monte Carlo simulations were developed using Cartesian geometry and all material specifications and gold concentration data were obtained from the literature. Tissue and tumor were treated as homogeneous mixtures of their component elements, and gold nanoparticles were modeled as homogenous distributions where specified. Flux and energy deposition calculations were performed using Monte Carlo N-Particle Code version 5.1.51.

ACKNOWLEDGEMENTS

I would like to thank my advisor, Dr. Magdi Ragheb, for his insight and direction as the ideas for this work developed, and for his continued guidance and support throughout my time at the University of Illinois. Additionally, I would like to thank Dr. Ling J. Meng for his insight and feedback while reviewing this work. I would also like to thank Dr. James F. Stubbins for allowing me to develop my interests as they led to this work. I would be remiss not to thank my parents for all of their support and guidance in allowing me to follow my passions as I went from student to teacher back to student. And finally, none of this would have been possible without the love and support of my wife, Anne, as I strove to complete this work.

TABLE OF CONTENTS

LIST OF FIGURES

LIST OF TABLES

Chapter I
Introduction

According to the World Health Organization, cancer is one of the leading causes of death in the world, with about 8 million deaths (13% of all deaths) attributed to the condition in 2007. Rising from 7.4 million deaths in 2004, this number is projected to rise to an estimated 12 million deaths within the next two decades [1]. Although it is a very broad term applicable to a group of diseases affecting any part of the body, cancer can essentially be described as a rapidly proliferating mass of cells growing without bounds or control. Arising from chromosomal damage or genetic mutations in a single cell or small group of cells, cancer can progress from a lesion to a benign growth to a malignant tumor. This progression is dependent on the severity of the original mutation, continued exposure to carcinogenic factors, and treatment efficacy. Although the types and frequencies of cancer differ widely around the world, the most commonly hit areas of the body include the lungs, stomach, liver, colon, prostate gland and breasts.

A comprehensive study of risk factors for cancer determined that avoiding key risk factors could prevent the occurrence of about 30% of all cancer [2]. Although several of the factors listed such as tobacco and alcohol use, physical inactivity, and pollution may be avoidable, assuming that all carcinogenic factors – physical, chemical, and biological – can be eliminated is not realistic. In addition, some studies suggest inheritable genetic factors in the occurrence and development of cancer. Consequently, even in ideally achievable environmental circumstances, a significant cancer burden remains to be treated.

Several treatments have been tried over the years with varying levels of success including surgery, chemotherapy and radiotherapy. The goal of each of these treatments is to remove or kill the tumor cells while minimizing inadvertent damage to the surrounding healthy cells. To that end, the calculations and results described in this work should prove useful in improving tumor-specific radiation doses without increasing the

dose to the surrounding tissue. The goal of this work is to quantitatively describe the benefits and possible limitations of using gold as a radio-sensitizing agent in all radiotherapy applications. Significant work has been done to illustrate the benefits of using gold with implanted radiation sources due to the improved dose enhancement seen at lower photon energies. However, this work will demonstrate that dose enhancement of several tens of percent can be seen when gold is used as a sensitizing agent with photon energies typical of external beam therapy. In order to better understand the properties of each of the treatment modalities and the specifics that might affect the use of gold in treatment, the three main treatment options currently used to treat cancers are described below.

1.1 Current treatment options

The success of treatment modalities depends on the type, size and location of the tumors, and time lapse between onset and diagnosis of the condition. Regardless of overall efficacy, however, each of these treatments has several associated side effects. Surgery is dependent on, and often drastically limited by, the level of access to the tumor location. Deep tissue tumors may require significantly invasive surgery while those in difficult to reach locations like the brain may be completely inoperable. Chemotherapeutic agents, though minimally invasive, are extremely toxic and non-specific targeting of the drugs can cause severe cell damage to normal cells. Radiotherapy has similar problems with non-specificity. Although effective deep tissue treatments can be developed through creative use of external beam geometries, surface tissue can be subject to unwanted and widespread radiation in the process. Meanwhile, implanted seed brachytherapy treatments can require invasive surgery while radioisotope therapy can result in radiation deposition along the entire route from injection to tumor localization. Similarly, immunotherapy and hormone therapy can have undesirable side effects. While the specifics of each of these therapy regimens are not the focus of the work presented here, it is beneficial to understand the general principles underlying each

modality as gold-mediated radiation therapy may be combined to create synergistic treatment regimens based on tumor conditions.

1.1.1 Surgery

Although limited by tumor location, surgery is the only way to specifically ensure the removal of cancerous cells without killing healthy cells. Excision surgery is significantly invasive, however, and is only effective if the tumor is confined to one area of the body, i.e. has not metastasized. Metastatic tumors that have impacted multiple organs are often too widespread for excision to be an efficient treatment strategy. In addition, cancers that do not produce localized tumors, such as leukemia, are not treatable by surgery as there are no specific masses to remove.

Other modes of therapy are often combined with surgery in an effort to make the entire treatment regimen more effective. Neoadjuvant therapy is given prior to surgery in an attempt to reduce tumor size and ensure easier tumor removal. This may include a combination of chemotherapeutic agents and hormone therapies. Adjuvant therapy is given following surgery in an attempt to reduce the chance of relapse and recurrence. An example of such a synergistic treatment is the use of the Gliadel wafer for glioblastomas multiforme. The wafer, when placed directly onto the tumor site after excision surgery, delivers drugs through a controlled release mechanism [3]. The combination of tumor removal and controlled release chemotherapy has been documented to significantly reduce the spread of the tumor. Gold nanoparticle therapy may prove to be another tool for adjuvant or neoadjuvant therapy regimens.

1.1.2 Chemotherapy

Anti-oncogenic drugs have been the subject of intense research for several decades. Numerous drugs have undergone clinical trials and are available on the market. These drugs function by disrupting cellular function during key steps of the cell cycle in an effort to minimize or eliminate tumor proliferation. Anthracylines, such as

Doxorubicin, act through DNA-intercalation interactions that disrupt nucleic acid structures and inhibit the DNA replication functions of cancerous cells [4]. Taxanes, such as Docetaxel, act by stopping key steps in the mitotic process, thereby eliminating cell replication [5]. Effective as they are, these drugs do not distinguish between healthy cells and tumor cells. As a result, the delivery system for these drugs must be designed in such a way to take advantage of localized differences at tumor sites.

In an effort to improve treatment efficacies, there has been considerable work done in the areas of nanobiology and nanotechnology and their applications to medicine. The ultimate goal is to develop novel treatment mechanisms that are triggered by tumor-specific stimuli such that cancerous cells are specifically and preferentially targeted. Tumors are subject to Enhanced Permeation and Retention (EPR) effects and localized pH environments that can be used to uniquely identify them for treatment purposes. These properties, described in a later section, allow for the development of drug delivery systems that do not release the toxic agents before reaching the target sites. Other clinical studies have tried to take advantage of the highly vascular nature of rapidly proliferating tumors by using anti-angiogenesis treatments [6]. The targeting strategies used for chemotherapeutic agents can be easily modified for use with gold nanoparticle agents in clinical applications and the simulations described in this work assume gold nanoparticle transport using EPR effects.

1.1.3 Radiation therapy

In general, radiation therapy can be broken into three main categories: external beam therapy (teletherapy), implanted internal radiotherapy (brachytherapy), and Radio-Isotope Therapy (RIT). Additionally, there are two distinct types of radiotherapy procedures: photon therapy and particle therapy. Each radiotherapy procedure is designed to eliminate tumor masses by causing DNA damage in the nucleus of the tumor cells. Cells have inherent DNA repair mechanisms, but double-stranded breaks are generally irreparable. Photon therapy induces DNA damage indirectly by creating radical species in the tumor blood supply that then cause the DNA damage. Particle therapy,

generally involving neutrons, protons, or other charged particles, can deposit enough energy at the tumor site to directly cause the double-stranded DNA damage.

Each of the three types of radiation therapy techniques is ultimately designed to destroy tumor cells while protecting healthy cells. The goal of using a selectively sensitizing agent is to enhance the ratio of dose given to the target cells compared with the healthy cells. Gold has been proposed as a potent radio-sensitizing agent in this regard due to its high-Z nature and general biocompatibility. Described below are the three main types of radiation therapy with comments on how the use of gold might improve treatment efficiency.

Teletherapy: External beam therapy is the most common form of radiation therapy in current medical use. Table 1-1 describes medically relevant x-rays based on peak tube voltage.

Table 1-1: Classification of x-rays based on beam voltage

Terminology	Beam voltage	Max. photon energy
Diagnostic x-rays	20 kV – 150 kV	150 keV
Orthovoltage x-rays	200 kV – 500 kV	500 keV
Megavoltage x-rays	1 MV – 25 MV	25 MeV

The prevalence of x-ray machines in use for imaging purposes makes an orthovoltage x-ray source easily available in most hospitals – an orthovoltage x-ray source differs from a diagnostic x-ray source only in the applied terminal voltage. Megavoltage x-rays are normally generated using a commercially available linear accelerator (linac) and are used for most teletherapy procedures commonly in use today. X-rays are produced over an energy spectrum with the maximum beam energy dependent on the peak beam voltage. These spectra must be collimated using a variety of filters to obtain the energy and shape of the beam required. Cobalt units producing dichromatic beams of 1.17 MeV and 1.33 MeV can also be used to generate the necessary radiation beams. Here the discrete energy nature of the beam makes up for the fact that higher or lower energy beams cannot be produced.

Conventional beam therapy involves the use of two-dimensional beams targeted at a tumor site. The use of multiple beams from different directions allows physicians to tune the absorbed dose at the tumor site. While the most well established teletherapy procedure, conventional beam doses are limited by the sensitivity of adjacent healthy tissue that can receive substantial radiation doses during some high-dose treatments. A combination of high resolution imaging techniques (such as Magnetic Resonance Imaging and Computed Tomography) along with beam collimation has resulted in the use of conformal teletherapy. Here, the tumor volume and the corresponding radiation dose volume can be well defined and the dose delivered to nearby healthy tissue is reduced. Newer techniques are being developed to use beam modulation in real-time to help optimize the dose being delivered to the tumor site. Examples of these techniques include Intensity-Modulated Radiation Therapy (IMRT), which uses precise tuning of "beamlet" energy to improve the shape of the delivered dose, and Image-Guided Radiation Therapy (IGRT), which uses real-time imaging techniques to visualize and tune the delivered dose.

Teletherapy involving charged particles is a field of growing interest but is still significantly less developed than photon therapy. Electrons have a maximum dose deposition depth of less than 5 cm, which makes an electron beam well suited for treating surface lesions but not very useful for deep tissue tumors. Protons and heavier ion beams deposit energy near the end of the beam path as described by the Bragg peak shown in Fig. 1-1a. This peaking characteristic is useful for treating tumors at greater depths since the energy of the particles can be tuned to ensure maximum energy deposition precisely at the tumor site. However, this technique becomes problematic for tumors with a significant volume. Ion beams of different energies must be used to target the entire tumor volume and the summation of the energy deposition curves results in the Spread-Out Bragg Peak (SOBP) shown on Fig. 1-1b [7]. Thus, while the entire tumor volume can be irradiated, tissues shallower than the tumor can receive significant amounts of radiation dose. By comparison, the energy deposited by a photon beam decays exponentially after the peak value, and a significantly smaller fraction of energy is

deposited at depths shallower than the target volume. Thus, the beam energy can be tuned to ensure maximum dose at the required depth while minimizing collateral dose.

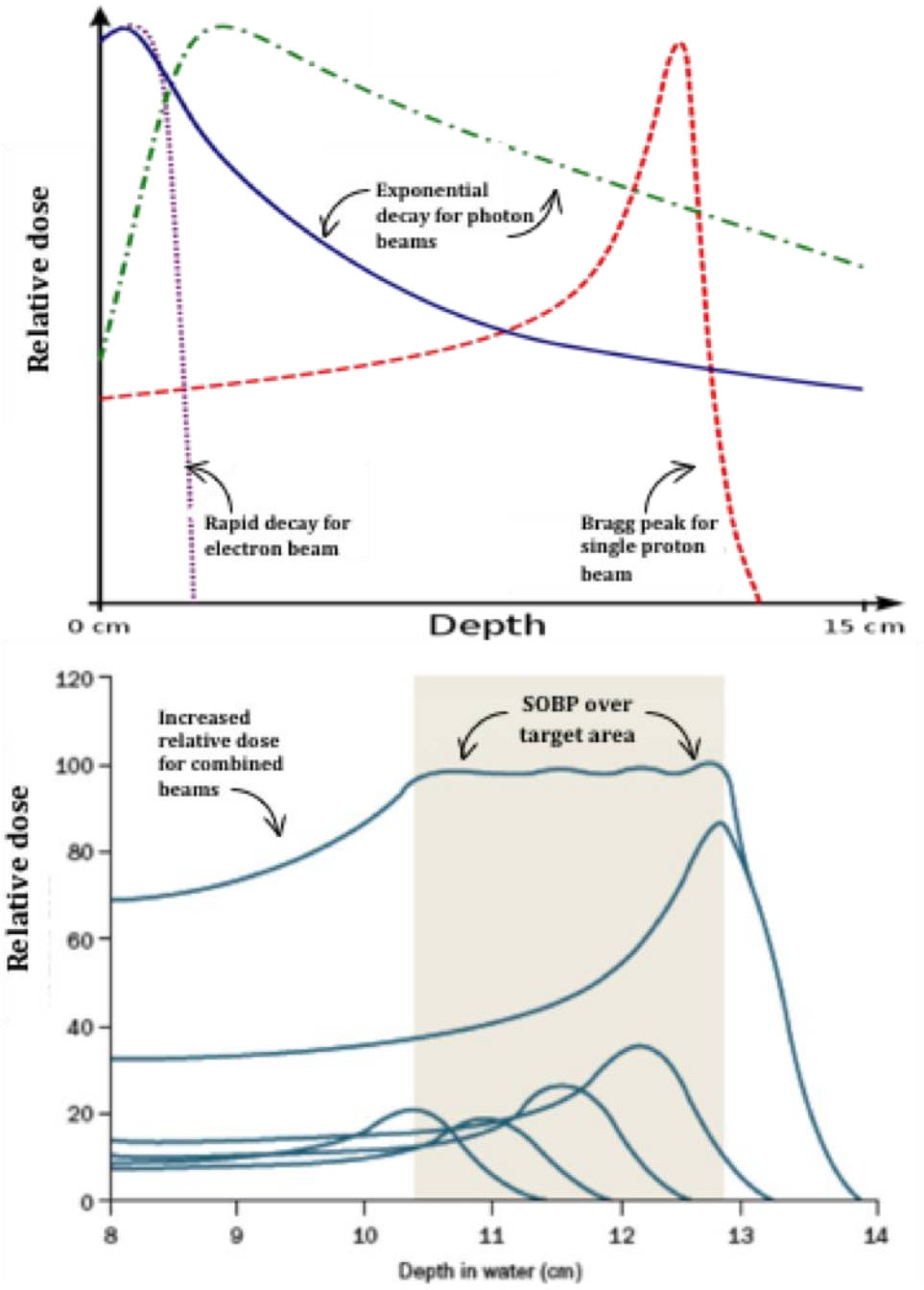

Figure 1-1: Relative dose deposition as a function of depth. Three different radiation types are shown. a. Exponential decay for photon beams compared to the Bragg peak characteristic for proton beam. b. Fractionated proton doses targeting a tumor volume can result in significant accumulation of effective dose at shallow depths. [Adapted from 7]

Brachytherapy: Internal radiotherapy involves the placement of a radioisotope inside or near the area needing treatment. The benefits of an implanted source stem from the fact that the radiation is impingent on a localized area and the dose to the surrounding healthy tissue is minimized. Since beam geometries and penetration depth are not influencing factors, the dose rate and source strength can be tailored specifically to the target tumor. Nevertheless, treatment efficacy is dependent upon the location of the tumor, as the placement of the source must avoid unaffected vital organs. As a consequence of the localized doses, brachytherapy has far fewer radio-toxicological side effects and has been successfully used to treat a variety of cancers including cervical, prostate, breast and skin cancers. The following isotopes have been used as radiation sources for brachytherapy:

Table 1-2: Commonly used sources for brachytherapy applications

Isotope	Principal γ-ray Energy
$Cesium^{137}$	662 keV
$Cobalt^{60}$	1.16 MeV, 1.33 MeV
$Iridium^{192}$	380 keV (mean)
$Iodine^{125}$	27.4 keV, 31.4 keV, 35.5 keV
$Palladium^{103}$	21 keV
$Ruthenium^{106}$	3.54 MeV

Radioisotopes with shorter half-lives can be used in the design of quasi-permanent brachytherapy treatments in which the radioactive seeds can be placed at the tumor site permanently with treatment duration limited by the radioactive decay of the isotope. Longer-lived radioisotopes can be used for temporary brachytherapy treatments in which the seeds are placed at tumor sites for up to 24 hours and then removed. Additionally, brachytherapy regimens can be designed to have variable dose rates depending on the source isotope used. Low-Dose Rate (LDR) brachytherapy involves radioisotopes with an absorbed dose rate up to 2 Gy/hr. By comparison, High-Dose Rate brachytherapy (HDR) can make use of sources with absorbed dose rates exceeding 12 Gy/hr. Tumor location and cancer type will determine both the duration of treatment and the type of source that is used for treatment.

Radio-Isotope Therapy: RIT involves the injection or ingestion of radioactive isotopes such that they preferentially accumulate at tumor sites. As a result, RIT may be considered a specialized form of chemotherapy as well. This therapy is commonly used to treat thyroid cancers and cancers of the neuroendocrine system – namely, cancers that do not respond well to surgery or have a high risk of recurrence after surgery. Additionally, RIT may be used to treat conditions that only affect specific portions of an organ such as bone metastases of certain cancers. Commonly used isotopes include I^{131} (has a thousand-fold accumulation preference for the thyroid compared to other organs), Y^{90} (has an affinity for peptide receptors to treat neuroendocrine tumors), and Sr^{89} (has an affinity for metastasis-affected bone over healthy bone). While RIT has been shown to successfully treat certain cancers, there is a danger of whole-body radiation delivery by damage to epithelial surfaces as the radioisotope travels through the body before reaching the targeted area. Affected areas may include the skin, oral, pharyngeal, and bowel mucosa depending on the targeted area.

1.2 Tumor properties

In order to determine how large of an improvement can be expected from the addition of gold to existing treatment options, it is important to understand the specific characteristics of tumors that differentiate them from healthy cells. Ideally, these unique attributes can be used to modify the radiation response of the affected area to ensure that only the tumor cells receive elevated doses of radiation while minimizing the dose to the surrounding tissue. There are three main properties of tumors that can affect the localized responses to radiation – leaky blood vessels, localized acidity, and hypoxia. Two of these properties, leaky vessels and acidity, are routinely used to develop targeting mechanisms for existing chemotherapy regimens. It is the third property, hypoxia, that proves the most problematic when determining radiation dose to tumors as described below. It is assumed that the advances in nanomedicine regarding effective drug delivery

systems using these properties can be applied to the transport of gold nanoparticles to tumor sites.

1.2.1 Enhanced Permeation and Retention (EPR)

The majority of tumors are composed of rapidly proliferating cells with little or no cell cycle regulation. This growth requires a significant increase in blood supply to the rapidly dividing cells and as a result, tumor cells over-express certain growth factors, such as Vascular Endothelial Growth Factor (VEGF) and Tumor Necrotic Factor (TNF), recruit additional blood vessels to the tumor site. The rapid, irregular, and unregulated development of blood vessels supplying the growing tumor cells results in a lack of proper alignment of the endothelial cells in the vessels. This, in turn, results in the presence of wide gaps in the vessels that give rise to the characteristic leaky vessel phenomenon associated with tumor masses. This leaky architecture coupled with the lack of a proper lymphatic drainage system means that any particle circulating in the blood supply that is smaller than the gaps will escape the leaky vessels at the tumor site as seen in Fig. 1-2 [8].

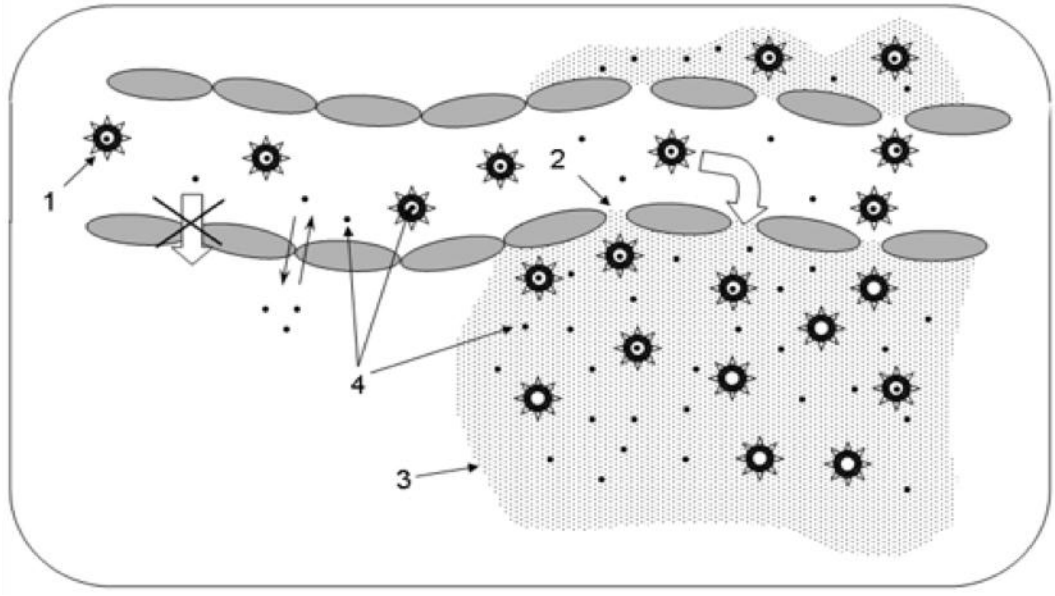

Figure 1-2: Nanoparticle extravasation through EPR effects. Leaky vessels proximal to tumor sites allow nanoparticles to pass through [8]
1: Nanoparticle is stable in circulation.
2: Gaps in the blood vessel near the tumor allow nanoparticle escape
3-4: After extravasation, nanoparticles accumulate at tumor site since they are too large to re-enter the vessel through the normal endothelial gap junctions.

Since the unregulated angiogenesis means there is no accompanying increase in lymphatic drainage at the tumor site, once a particle escapes a vessel at the tumor site, it will remain there. As a result, particles designed to be stable enough to remain in circulation for an extended period of time will eventually accumulate at the tumor site through this Enhanced Permeation and Retention (EPR) effect [9]. This effect has been successfully used in various different drug delivery systems and is assumed to be the primary targeting mechanism for the purposes of this study. Free circulating gold nanoparticles should accumulate at tumor sites resulting in a concentration of gold at the tumor site while the remainder gets cleared from the body through the renal system. Fenestrations in the leaky vessels can be as large as several hundred nanometers, and studies have shown that particles up to 100 nm can be used to passively target tumors [10, 11]. Additionally, a study by Chithrani et al. showed that cellular uptake of gold nanoparticles is most efficient using 50 nm particles while significant cellular uptake was seen for particles up to 72 nm in size [12].

1.2.2 Localized acidity

Another property that differentiates tumor cells from healthy tissue is localized acidity compared to physiological pH. Since the extracellular pH environment at tumor sites is slightly acidic (median pH of 6.5 compared to pH 7.4), a triggered release mechanism can be developed to ensure targeted drug delivery and reduce any associated non-specific toxicities [13]. The reasons for this localized acidity have been theorized in published literature but no conclusive theory has been established as the root cause. Nevertheless, the unique physical environment exists, has been used in treatment applications, and may potentially be used for gold transport in future developments.

1.2.3 Hypoxia

The tumor property that most significantly impacts the response to a radiation dose is the hypoxia that develops at the center of tumor masses. As mentioned above, tumor cells proliferate at an accelerated rate and rapidly recruit the formation of blood

vessels to supply the growing mass with nutrients. However, it is important to note that these blood vessels are only recruited at the surface of the tumor. The rapid growth actually results in the blood supply being choked off from the center of tumor mass resulting in a locally hypoxic environment compared to the periphery of the tumor and compared to normal cell structures.

The reason this significantly impacts radiation response is that oxygen is a fairly potent radiosensitizer. The radical ions created by photon beams, that subsequently cause DNA damage, are primarily comprised of oxygen species. As a result, a decrease in the amount of oxygen present at the tumor site decreases the effectiveness of the photon beams in destroying the targeted tumor cells. Higher dose delivery becomes necessary to surmount these hypoxia-induced effects. Several drugs have been used to combat this reduced radiation efficacy – they work by introducing pharmaceutical agents that mimic oxygen's ability to act as a radiosensitizer. One of the goals of this work is to show that implanted or accumulated gold at tumor sites can act as an extremely efficient radiosensitive agent. Corroborating work done in the past showing the effectiveness of using gold-modulated radiation therapy, the work presented here should provide a foundation for the various physiological dependences of using gold.

A final note on tumor-specific properties: Gold delivery and drug delivery mechanisms in general have not been addressed in the scope of this work. Nevertheless, as maximal nanoparticle uptake in cells occurs at sizes smaller than the upper limit of the EPR window at tumor sites, it is suggested that the size of the particles can be tuned to optimize the therapeutic and diagnostic efficiencies without adversely affecting delivery efficiency. As a result, all simulations described in this work assume particle sizes previously reported in both *in vitro* and *in vivo* murine studies, and do not address any site-specific delivery concerns. Those concerns must be and have been addressed in separate studies as discussed.

1.3 Radiation interactions with matter

Before discussing the mechanisms for localized dose enhancement at tumor sites, it is important to discuss the different processes through which the incident radiation interacts with the targeted tissue. Understanding the mechanisms in question can lead to a much better understanding of the relevant variables that need to be controlled in order to create a more effective treatment regimen.

Brachytherapy sources emit gamma rays in the tens of keV range, while teletherapy generally uses megavoltage x-rays in the MeV energy range. As a result, interaction cross-sections must be investigated over an energy range of 10 keV to 10 MeV. Plots of the specific interaction cross-sections for gold and tissue over this range are included in Appendix D. Photon beams with energy levels relevant to therapeutic applications can interact with human tissue in one of three main ways – the photoelectric effect, Compton scattering, and pair production. Although other modes of interaction are possible, the cross sections for human tissue only become statistically significant at energy levels that are several orders of magnitude higher, and so are assumed to be irrelevant in the scope of this work. The three modes of interaction considered physiologically relevant are discussed below:

1.3.1 Photoelectric effect

An incoming photon beam interacts via the photoelectric effect by colliding with an orbital electron of a target atom. The excited electron is ejected and an outer shell electron drops down to fill the vacancy. This transition is accompanied by the emission of soft x-rays that are deposited in the immediate vicinity of the interaction. Secondary emission occurs when the excited target atom returns to its ground state by emitting x-rays and Auger electrons. Ionization occurs due to the initially ejected electron as well as the subsequent Auger electrons. Photoelectric effect cross sections are directly proportional to the number of electrons in the target and inversely proportional to the energy of the incoming beam as shown in Equation 1-1.

$$\sigma_{pe} \approx C\frac{Z^5}{(h\nu)^{3.5}} \tag{1-1}$$

As a result, low energy $(h\nu)$ photon beams targeting high-Z materials produce significant localized dose due to the photoelectric effect. Since gold is a high-Z material (Z = 79) compared to normal tissue (Z = 6–10), the photoelectric effect may have a profound impact on the localized effects of applied radiation. The physical mechanism is illustrated in Fig. 1-3 and is most significant for beam energies below 100 keV**.** This is evident as the K-edge for gold exists at 80.7 keV as described in Table D-1 in Appendix D. Several brachytherapy sources have gamma emission spectra in the low keV energy range and so mostly interact with target tissues through the photoelectric effect. Beams that have lost their energy due to other interactions can interact through the photoelectric effect as well, so it is a relevant interaction mechanism for all radiotherapy beam energies.

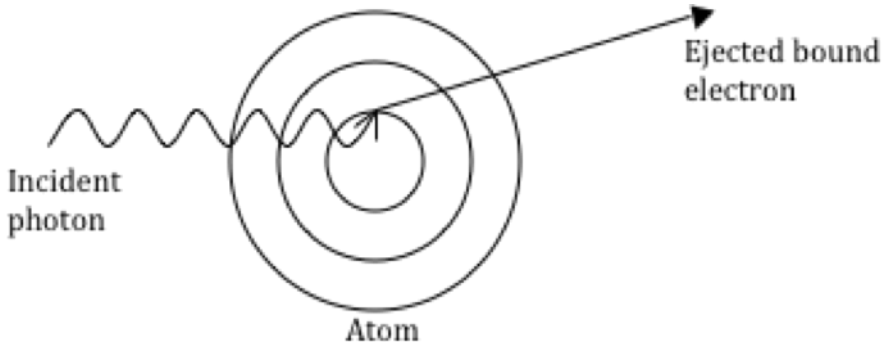

Figure 1-3: Photoelectric effect

1.3.2 Compton scattering

Photon beams undergo Compton Scattering when an incoming photon collides with an outer shell, or free, electron in the target material. Contrary to the photoelectric effect in which the photon energy is almost completely absorbed by the target electron, Compton Scattering involves the scattering of both the incident photon and the target

electron. The scattered electron can cause localized ionization while the scattered photon can undergo further interactions in the target material depending on the amount of energy it carries away from the collision. Although the Compton Scattering cross section is directly proportional to the number of electrons in the target atom, the dependence is linear as given in Equation 1-2.

$$\sigma_c \approx C \cdot Z \tag{1-2}$$

The physical mechanism associated with Compton Scattering is shown in Fig. 1-4 and can be compared to the Photoelectric effect described earlier. Due to the excess energy carried by the incident photon, it is scattered off the target atom instead of being absorbed as in the photoelectric effect shown in Fig. 1-3. While there is no explicit energy dependence show in Equation 1-2, the cross sections for Compton Scattering interactions dominate in the photon energy range most prevalent in radiotherapy applications. The cross-sections plotted in Figs. D-1 and D-2 show that Compton Scattering becomes the primary mode of interaction for photon energies in the 600 keV to 50 MeV range for pure gold, and between 30 keV and 3 MeV for healthy tissue. X-ray beams primarily used in teletherapy applications have an energy range of 1-20 MeV, and Compton Scattering cross sections dominate calculations of total absorption cross sections in that energy range.

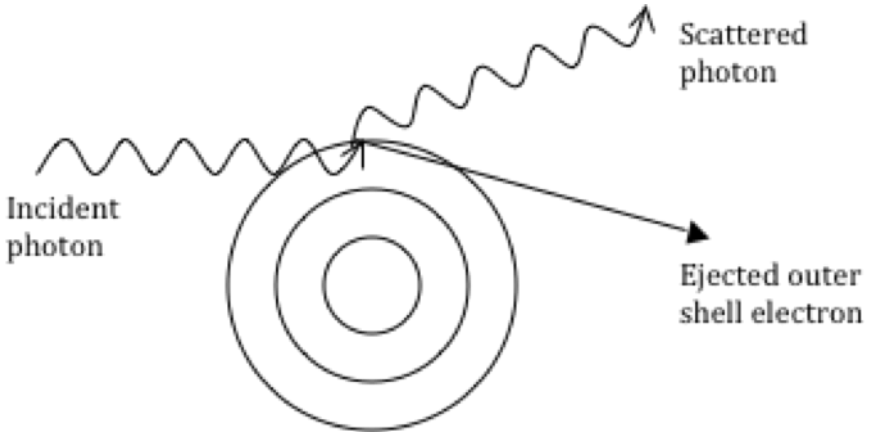

Figure 1-4: Compton scattering

1.3.3 Electron-positron pair production

This mechanism involves the interaction of an incident photon with the nucleus of a target atom instead of an electron. The incident photon collides with the nucleus and transfers all of its energy to the target. An electron and positron pair is ejected as a result of this collision, and each particle causes ionization in the surrounding tissue. As an antimatter particle, a positron cannot exist freely and collision with a free electron causes annihilation and two photons are produced that scatter in opposite directions. The cross section for pair production is directly proportional to the square of the atomic number of the target, as shown in Equation 1-3.

$$\sigma_c \approx C \cdot Z^2 \tag{1-3}$$

Due to the creation of the electron-positron pair, the cross-section for this mechanism has inherently associated threshold energy and is described below in Fig. 1-5. The energy threshold is equal to the sum of the rest masses of the electron and the positron, namely 1.02 MeV. The cross-sections increase as photon energy increases as described in the figures in Appendix D, but this process is not possible for incident photons with lower energy levels. The energy of the subsequently generated photons depends on the energy of the incident beam as it is imparted to the ion pair produced, and these secondary photons may then undergo further interactions in the target material based on their energy levels.

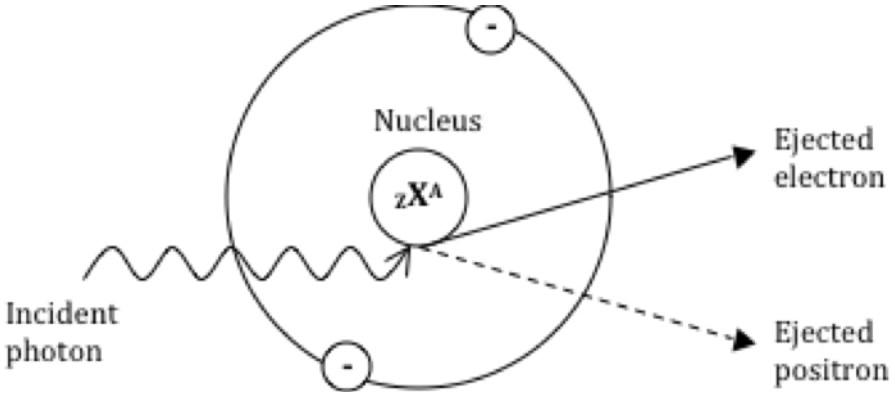

Figure 1-5: Electron / positron pair production

1.3.4 KERMA approximation and mass attenuation coefficient

The calculation of total mass attenuation coefficients is more useful to radiological applications than the individual interaction cross sections mentioned above. The benefit of calculating a single set of energy-dependent coefficients stems from the fact that it can then be used as a set of weighting factors when calculating the effects of photon beams incident on tissue. Since the component cross sections are dependent on the atomic number of the target material, the overall mass attenuation coefficient has a similar dependence. This dependence is what allows for the development of high-Z contrast materials for imaging and treatment purposes. The difference in the mass attenuation coefficients for gold and tissue are shown in Fig. 1-6; the total attenuation coefficients are plotted as a function of photon energy and include the three interaction mechanisms discussed above. The work described here makes use of the fact that the attenuation coefficients for gold and tissue differ by an order of magnitude or more over the range of photon energies normally available in hospital settings. Attenuation coefficient data is available from [14].

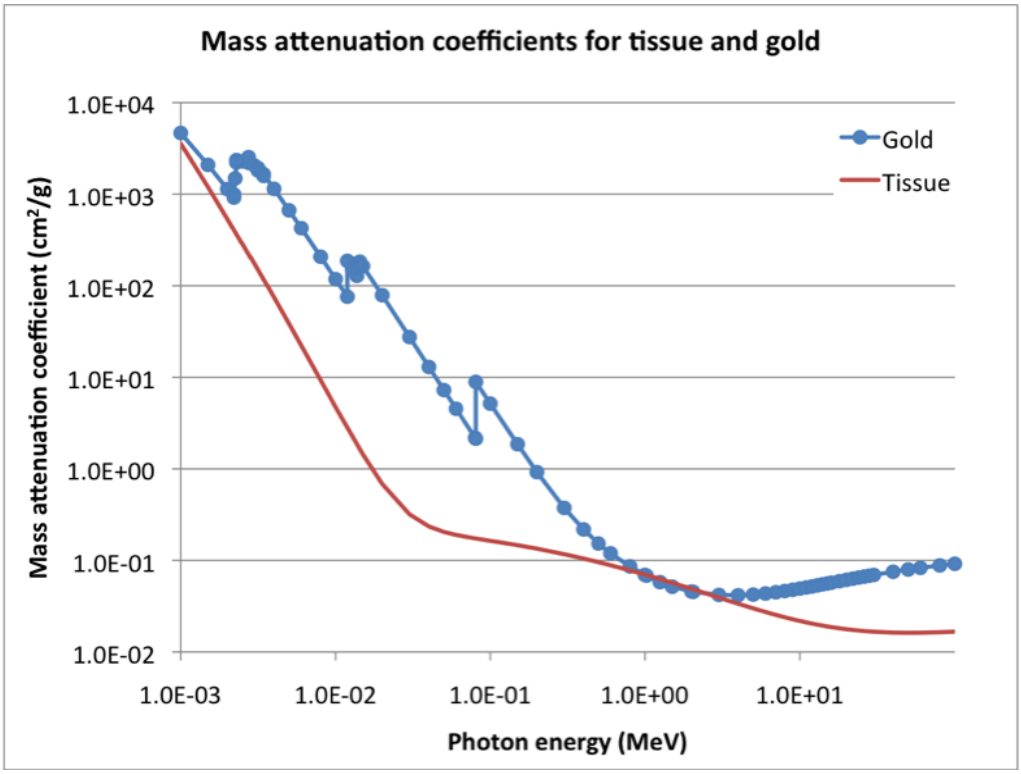

Figure 1-6: Difference in attenuation coefficients for gold and tissue

A quantitative method to estimate the amount of energy deposited as a result of the photon interactions described above is the KERMA approximation. KERMA is an acronym for the sum of all ***K***inetic ***E***nergies of those primary charged particles ***R***eleased by photons per unit ***MA***ss as defined in ICRU Report 33 [15]. This approximation assumes that any electrons induced by the incident photon beam come to rest in proximity to the interaction site and all primary electron-induced photons escape. It ignores any energy deposition due to any secondary charged particles and takes into account the cross-sections for the photoelectric effect, incoherent Compton scattering, and pair-production as seen in Equations 1-4 and 1-5 as described by Hubbell et al. [16]. However, it is important to note that the energy of the incident photon beam itself does not factor into the energy deposited other than the associated changes in interaction cross-sections.

$$KERMA = \varphi\, E \frac{\mu_{tr}}{\rho} \tag{1-4}$$

$$\frac{\mu_{tr}}{\rho} = \frac{\left(f_{pe}\sigma_{pe} + f_{cs}\sigma_{cs} + f_{pp}\sigma_{pp}\right)}{\rho} \tag{1-5}$$

As seen above, the coefficients can be calculated by taking the product of the photon fluence, the photon energy, and the mass-energy transfer coefficient μ_{tr}/ρ described in Equation 1-5. Consistent with the definition of the KERMA approximation, secondary photons and associated electrons are ignored in Equation 1-4. The *f* factors in Equation 1-5 represent the average fraction of photon energy that is transferred to the kinetic energy of charged particles in the other possible interactions and are given below in Table 1-3. The energy dependence of each of the interaction mechanisms is also evident in the expressions given below. The fluorescence energy χ depends on the distribution of electron vacancies produced during the interaction in question.

Table 1-3: Energy transfer fractions for calculating μ_{tr}/ρ

Interaction	*f* factor
Photoelectric effect	$f_{pe} = 1 - (\chi / E)$
Compton Scattering	$f_{cs} = 1 - (\langle E' \rangle + \chi) / E$
Pair Production	$f_{pp} = 1 - (2\, mc^2 / E)$

An alternative method of calculating energy deposition at photon interaction sites involves calculating mass-energy absorption cross sections. This method assumes that not all of the primary electron energy is deposited locally and is quantitatively represented by the (1–*g*) correction factor in Equation 1-6 where the value of *g* depends on the incident photon energy and the type of interaction. The relevant equations for *g* are given in [16] and significant errors become apparent for photon energies higher than 100 keV as seen in the figures included in Appendix D.

$$\mu_{en}/\rho = (1-g)\,\mu_{tr}/\rho \tag{1-6}$$

The two different approaches used to model the relevant physics in the Monte Carlo (MC) simulations described in this work can be compared to the two different methods described above. The preliminary MC models described in Chapter 4 approximate charged particle transport and so represent a small improvement on the KERMA approximation discussed here. The detailed models described in Chapter 5 use more detailed particle transport and thus incorporate improved physical accuracy. Details of the individual tallies used to record the results of the Monte Carlo simulation and specifics of the simulation code used, are discussed in Chapter 3. The argument is made for both the track-length average method of calculating energy deposition, as well as, the pulse-height detector approach.

Chapter 2
Literature survey

Since the physiological significance of the work presented here depends on the use of gold in clinical settings, it is prudent to review the various properties and biological applications of gold presently available in previous publications. The plethora of information available for gold is due to the fact that it has been considered a precious metal since the beginning of recorded history and has been used as a coinage standard and symbol of monetary wealth through the ages. In more recent times, its favorable physical and chemical properties have made it an attractive material option for various electronic, chemical, and biomedical applications. Furthermore, the recent explosion of interest in nanotechnology has led to a proportional increase in interest for precious metals including gold.

In the context of cancer treatment, gold has been primarily utilized in the scope of nanobiology and nanomedicine. Despite studies showing bulk gold to be biologically inert, various studies on gold nanostructure formulations have shown nano-gold to be inconsistently biocompatible depending on particle size and shape [17]. However, studies have shown several formulations with minimal inherent cytotoxicity and no stress-induced release of cytokines, indicating a well-defined window available for further research [18].

In addition to the passive targeting studies presented in this chapter, several studies have been published on the use of monoclonal antibodies to transport species of interest to targeted tumor sites. Monoclonal antibodies have the benefit of being targeted to specific extra-cellular markers on the surfaces of tumor cells. As a result, using these targeted antibodies can result in preferential accumulation of the gold nanoparticles at tumor sites with minimal accumulation in healthy tissue. This idea is discussed briefly in

this section and it is suggested that future work may extend the results presented here to include the improved tumor targeting available.

Since the proposal to use gold as a radio-sensitizing agent requires an *in vivo* concentration of nanoparticles, the various physical and chemical properties of the gold formulations must be well characterized. Given the extensive use of metallic gold, and the increasingly extensive use of gold nanostructures, these properties have been well documented and those relevant to this work are discussed below. Furthermore, the biocompatibility of specific nanostructures is also an important design consideration and the size- and shape-dependent factors leading to *in vivo* compatibility are discussed here. However, a key assumption for the work presented here depends on the biocompatibility of gold nanostructures. These properties are discussed below along with several passive and active mechanisms for specific tumor targeting of gold nanoparticles.

2.1 Physical, chemical, and nuclear properties

Bulk gold is a dense, lustrous, diamagnetic, transition metal that resists oxidative corrosion in both air and water. Although not chemically inert, it is the least chemically reactive of all metals and, in its pure form, is non-reactive to all body chemistries as it resists attack by all biologically relevant acids. It is the most electronegative metallic element, accounting for its lack of reactivity, and is one of the densest metals, $\rho = 19.30 \frac{g}{cm^3}$. The face-centered-cubic crystalline structure of gold results in a highly malleable and ductile nature, leading to relatively easy manipulation and well-ordered nanostructure formulation [19]. Most medical applications of gold are a result of the unique properties that emerge when dealing with nano-scale gold. These properties are often size-dependent and can be tuned to the specific application in question.

There are several physical property changes that can be expected as formulation size is decreased from the macroscopic scale to the nanometer scale. Obviously, as particle radius decreases, surface area increases dramatically relative to volume as

described in Equation 2-1. Associated with this increase in surface area and the corresponding increase in surface curvature, the melting point of nano-gold can be significantly lower than that of bulk gold [20].

$$\text{Surface area to volume ratio: } \frac{SA}{V} = \frac{4\pi r^2}{\frac{4}{3}\pi r^3} = \frac{3}{r} \tag{2-1}$$

Aside from these expected changes, one peculiar property change that occurs at smaller particle sizes is the emergence of magnetism. Although this change has not yet been seen in gold, it has been observed in nano-clusters of aluminum that is also non-magnetic in bulk form. Magnetic properties of nanoparticles have been used in several formulations and may prove useful for future studies with gold if the property can be identified in nano-gold. The increase in surface area will be significantly important in this proposal, as the amount of targeting ligands that can be adsorbed to the surface will be directly proportional to the particle surface area. Similarly, the amount of monoclonal antibodies that can be attached to gold, or vice versa, is a direct result of the relative sizes of these species. Additionally, as particle surface area increases, the probability of self-aggregation due to environmental triggers also increases which affects the efficacy of certain formulations. Consequently, property changes at the nano-scale become significant when determining the clinical significance of this study even if they are not directly utilized in the work given here.

In addition to physical property changes due to size reduction, there are several optical and electronic properties unique to nano-gold structures. One of the optical properties of nano-gold, known since antiquity, deals with the interaction of specific wavelengths of light with the nanostructures. As the size of the structure becomes smaller than the wavelength of the incident light, coherent oscillations of free electrons in the conduction band cause strong absorption of green light. This effect causes nano-gold to appear red, though the color can be tuned by carefully controlling particle size. The application of solutions of gold colloids of various sizes has been used to create vivid and brilliant colors in stained glass. These effects, commonly referred to as the surface

plasmon band (SPB), were first quantitatively described by Mie in 1908 and all subsequent studies have correlated the original theory posited by Mie [21]. Colloid solutions of gold nanoparticles exhibit an SPB around 520nm making it incredibly useful for cellular imaging applications since it lies outside the near-UV range of biological autofluorescence [22]. The maximum wavelength and bandwidth of the SPB is dependent on particle structure and size making it possible to tune the detectable wavelength by changing the nanostructures [23]. This property can be extremely useful to generate real-time images of subjects undergoing studies involving the use of gold, including clinical applications of the work presented here, without disrupting the parameters of the study.

Related to the described plasmon resonance, several studies have also explored the possibility of self-fluorescence of gold nanoparticles in the absence of external stimuli. Although a number of surface ligands have shown promise in their abilities to enhance this fluorescence, the scope of this study precludes detailed examination of these properties. SPB-related effects may be sufficient in future work to track the distribution of gold nanoparticles in the body. Similarly, studies concerning the size-dependent changes in the conductivity of gold are not discussed in this study.

As previously mentioned, gold is the most electronegative metal. This directly leads to it being the least chemically reactive metal, and is the reason it resists attack by most acids. The most common oxidation states of gold used in medical applications, Gold (I) and Gold (III), are stable in aqueous solution. This stability, in addition to the fact that gold is resistant to corrosion in both air and water, makes gold formulations extremely attractive candidates for medical applications. Biocompatibility and distribution studies, as well as specific uses of gold nanoparticles are described in detail later in this work.

The electronic configuration and nuclear structure of gold are the basis for its use as a contrast and radio-sensitizing agent in radiotherapy. The fact that gold has 79 protons and electrons makes it an ideal target for photoelectric-type interactions as σ_{pe}

has a very strong atomic number dependence as seen in Equation 1-1. When compared to healthy tissue that is mostly comprised of low Z elements such as hydrogen (Z=1), carbon (Z=6), nitrogen (Z=6), and oxygen (Z=8), gold can have a six to nine orders of magnitude higher cross section for the same photon energy. The specific cross sections are compared in Appendix D.

2.2 Structure and formulation

Michael Faraday was the first to describe the formulation of gold nanoparticles, in 1857, using a two-phase reduction of an aqueous solution of sodium tetrachloroaurate ($Na[AuCl_4]$) with phosphorus as the reducing agent, dissolved in a solution of carbon disulfide. His method yielded a wide distribution of particle sizes ranging from 3 nm to 30 nm. This was followed by the report by Turkevich of the now widely used citrate reduction method in which chloroauric acid ($HAuCl_4$) is reduced using trisodium citrate [24]. The trisodium citrate acts as both the reducing agent and the stabilizing ligand and varying the relative concentrations of $HAuCl_4$ and trisodium citrate results in very controlled nanoparticle sizes up to 200 nm [25, 26]. Besides citrate-stabilized nanoparticles, a widely studied area of interest is in thiol-protected gold nanostructures due to the broad versatility of thiol-based conjugation chemistries. Brust and Schiffrin first described the generation of thiol-protected gold nanoparticles in 1994 using a two-phase liquid-liquid system to form protected nanoparticles with diameters on the order of a few nanometers [27].

Modifications to the Brust-Schiffrin method have used a wide variety of other organic ligands to stabilize the gold nanoparticles including amines, phosphines, carboxylates, proteins, DNA, enzymes, and small drug molecules [28-32]. As polymer stabilization has been reported to greatly increase blood circulation times of nanoparticles, use of this mechanism looks promising for the purposes of this work. Polymers used as ‘stealthing’ ligands have included poly(vinyl pyridine), poly(ethylene glycol), poly(*N*-isopropyl acrylamide), and poly(methyl methacrylate) [33-38]. While the

specific properties of the polymers are different, the overall effects are similar in that the gold nanoparticles display monodispersity *in vitro*, are protected from self-aggregation *in vivo*, and have prolonged circulation times in the blood.

2.3 Cytotoxicity and biodistribution studies

Several toxicological studies on nanoparticle applications have been reported in various studies. These studies have used Inductively Coupled Plasma (ICP) Spectroscopy to determine and quantify the distribution of the gold nanoparticles. ICP Atomic Emission Spectroscopy (ICP-AES) uses the characteristic wavelengths of excited ions to determine the presence of specific metals in a sample. Along the same lines, ICP Mass Spectroscopy (ICP-MS) uses ICP to generate ions in the sample that are then separated and quantified using a coupled mass spectrometer. By isolating specific organs after gold nanoparticle treatment, the amount of gold present in the tissue can be determined by ACP-AES or ACP-MS after acid digestion of the tissue. These methods were primarily used to determine the amount of gold uptake in the distribution studies given below.

A recent review by Alkilany and Murphy contained a comprehensive summary of research done on the *in vitro* and *in vivo* cytotoxicity of gold nanoparticles [18]. The review included toxicity results for gold nano-spheres ranging in diameter from 0.8 nm to 250 nm, and nano-rods ranging in size from 40 nm x 18 nm to 65 nm x 15 nm. According to the studies reviewed, gold nano-spheres with a range of sizes (4, 12, and 18 nm in diameter) and surface moieties (citrate, cysteine, glucose, biotin, and cetyltrimethylammonium bromide (CTAB)) are non-toxic to human leukemia cell lines [39]. Further work describes the non-toxicity of spheres with 3.5 nm and 10 nm diameters to human immune cell lines [40]. In addition, nanoparticles smaller than 2 nm in diameter are toxic and show chemical reactivity, possibly due to surface agents, that are not present at larger sizes [41-43]. In vivo studies of nanoparticle size effect on toxicity, however, illustrate very different results.

Work done by Chen et al. showed both small (3 and 5 nm diameter) and large (50 and 100 nm diameter) nanoparticles are not toxic in mice while intermediate sizes (8 – 37 nm diameter) had lethal effects as shown in Fig. 2-1 below [44]. As a result, there is a window of *in vivo* toxicity for gold nanoparticle that can be avoided to develop effective delivery systems. Fortunately, work done by Chithrani et al. described receptor-mediated endocytosis (RME) as the primary mechanism for cellular uptake and maximal cellular uptake for transferring-coated gold nano-spheres with a diameter of 50 nm [12, 45]. Since this maximal uptake diameter falls outside the toxic window, the detailed models described in Chapter 5 used nanoparticle sizes of 50 nm to determine dose enhancement.

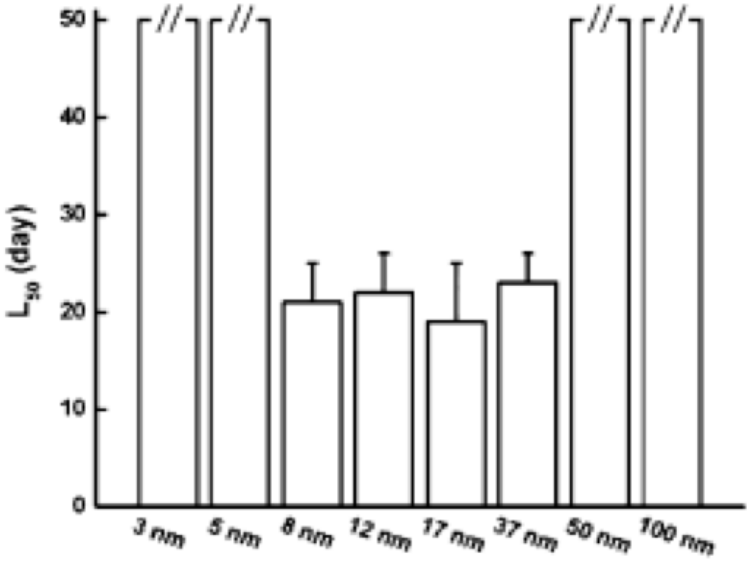

Figure 2-1: *in vivo* toxicity as a function of nanoparticle diameter. Only particle sizes between 8 and 27 nm displayed toxicity. [44]

2.4 Active targeting strategies

While work to improve passive targeting of tumor cells is ongoing, significant effort is being made to develop active targeting methods as well. A large amount of research is being undertaken on the use of monoclonal antibodies (mAb) to bind to tumor

cell surfaces in an effort to recruit the immune system and administered pharmaceutical agents to the target. The immune system normally responds to foreign species by differentiating between native and non-native. Since tumor cells are essentially native to the patient, the normal immune response is insufficient to attack these cells. However, due to cell cycle and proliferation irregularities, tumor cells display several unusual antigens that may be used to target these cells. Since these antigens are physiologically inappropriate based on cell type, antibodies specifically tailored to those antigens may be used to ensure specific delivery of therapeutic agents.

The benefit of using monoclonal antibodies to transport gold nanoparticles to tumor sites can result in significant accumulation in tumor cells while minimizing the diffusion into healthy cells. As mentioned earlier, the Enhanced Permeation and Retention (EPR) mechanism can be used to transport any nanoscale particles to tumor sites. Without active targeting, however, there is still a chance that the gold may undergo cellular uptake into the surrounding healthy cells instead of specifically into the targeted tumor cells. Labeling gold with appropriate monoclonal antibodies can result in specific binding to the extracellular markers of tumor cells and therefore specific uptake into the targeted tumor cells. This mechanism has been used to specifically direct chemotherapeutic agents and can be similarly used to direct the gold nanoparticles.

As shown in Fig. 2-2 below, several different treatment options become available once the antigens displayed on the tumor cell surface have been correctly identified and the corresponding antibodies have been conjugated to the treatment agent [46]. A cursory literature survey yielded over 200 monoclonal antibodies that have been approved or being investigated for clinical use. As a result, it is becoming increasingly possible to accurately determine which antibody may be necessary to specifically target tumor cells without any passive leakage of the therapeutic agent into neighboring healthy cells. The effects of minimizing passive diffusion are discussed below in Chapter 5, and it may be possible to entirely prevent this diffusion with appropriate use of a monoclonal antibody conjugation in the future.

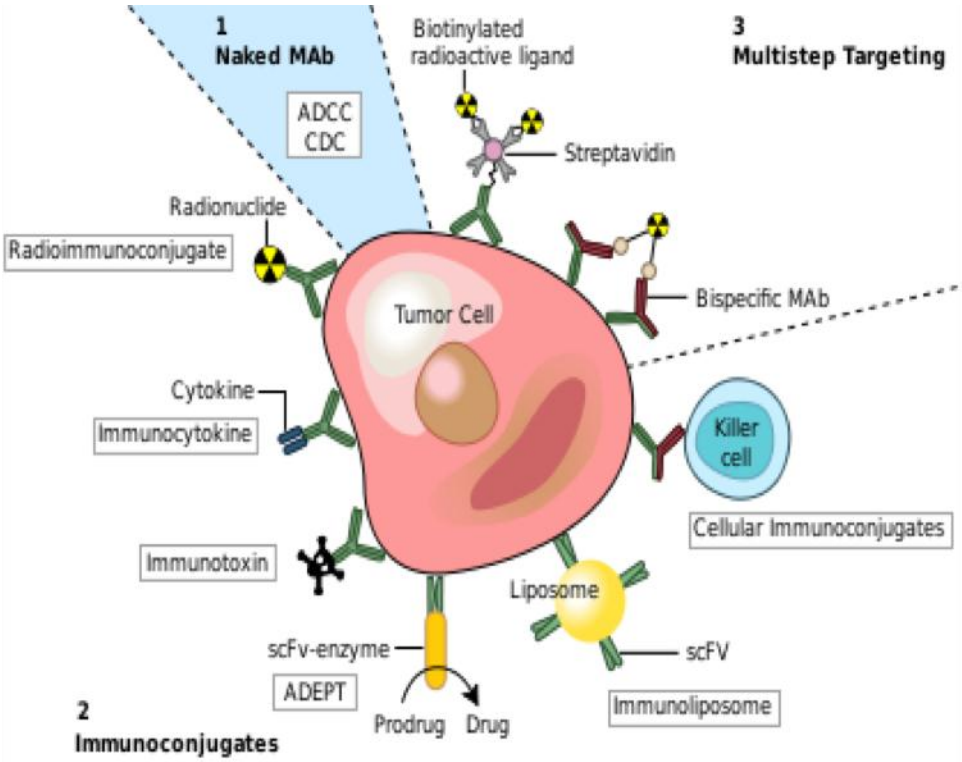

Figure 2-2: Active nanoparticle targeting using mAb. Multiple therapeutic agents can be conjugated to mAb to specifically target a tumor cell. Adapted from [46].

2.5 History and current applications

Although Faraday described the formulation of gold nanoparticles as early as 1857, the use of gold for medical applications was not posited until German physician and microbiologist Robert Koch first highlighted the possibility in 1905 when he described the antibacterial effects of gold cyanide on tubercle bacilli [47]. His discovery led to further research in gold compounds for medicinal purposes and, in 1929, French physician Jacques Forestier published his seminal work on the anti-arthritic activity of gold compounds [48]. Since the 1970s there has been considerable interest in the relevant biochemistries of gold complexes and research has included the use of gold salts to treat rheumatoid arthritis, colloidal gold solutions as *in situ* imaging agents, gold nanoparticle probes as biological markers, and radiolabeled gold particles as therapeutic agents for cancer treatment [49, 50]. Gold's high density, very high electrical

conductivity, and electron production ability also lend it to scanning electron microscopy applications for improved spatial resolution [51].

Although gold has been the focus of widespread research for several decades in the fields of cancer imaging and treatment, only recently has it been used in conjunction with the advances of nanomaterial research. Gold nanostructure assembly can be very tightly tuned to develop a variety of structures including nanoparticles, nanorods, nanocages, and nanoshells with sizes controlled on the order of nanometers. Due to the relative ease of fabrication, several studies have been conducted to test the biocompatibility of various gold nanostructure formulations and optimal ranges have been established for particle size, shape, and aspect ratio. In addition, due to the ease with which ligands can be conjugated to the surface of structures, many different surface modifications have been studied for therapeutic and diagnostic applications. Gold has shown promise in drug targeting applications due to its affinity for surface adsorbed proteins, and in imaging applications due to its uniquely tunable optical characteristics using Raman scattering.

2.5.1 Nanomedicine

Bio-nanotechnological advances have resulted in relatively widespread use of gold nanoparticles. Molecular labeling using AuNP has been a popular choice for developing sensitive detection techniques. As mentioned earlier, a variety of species can be adsorbed to the surface of nanoparticles including antibodies, peptides, and proteins [32, 51, 52]. The optical properties of gold nanoparticles, when differentiated from naturally fluorescent biological molecules, can provide significant improvement in the detection schemes. Additionally, since these optical properties are dependent on particle size and aspect ratio, the assays can be finely tuned depending on the target [53]. The possibilities of being able to image drug delivery in real time have led to increasing interest in ‘theranostic’ applications in which therapy and diagnosis are combined into the same overall treatment scheme.

Due to the many favorable properties of gold at the nano-scale, AuNPs have become increasingly popular as delivery agents to regulate biological processes as of late [54]. Kumar et al. described an intracellular imaging platform utilizing multifunctional AuNPs that combined imaging and cytosolic drug delivery [55]. These 'nanosensors' included antibodies specific to actin and biotin to induce the binding capacity of the AuNP, and successful targeting resulted in the expression of an optical signal. Similarly, Chan et al. demonstrated the down-regulation of a receptor over-expressed in several breast cancers using antibody-conjugated AuNPs using the mechanisms for monoclonal antibody AuNP tagging that were discussed earlier [56]. Eghtedari et al. appended PEG molecules to similar antibody-conjugated AuNP to increase their stability *in vivo* and extend particle lifetime in blood [57].

A visual representation of a multifunctional gold nanoparticle is shown below in Fig. 2-3. Here, several functional moieties are displayed on the surface of the AuNP with targeting and delivery capabilities. Ideally, the target cells preferentially express the cell surface markers for the included antibodies and therefore, accumulate the AuNP exclusively. Once the cell-surface antigens recruit the AuNP, the delivery peptides can be cleaved to induce optical signals or deliver drugs.

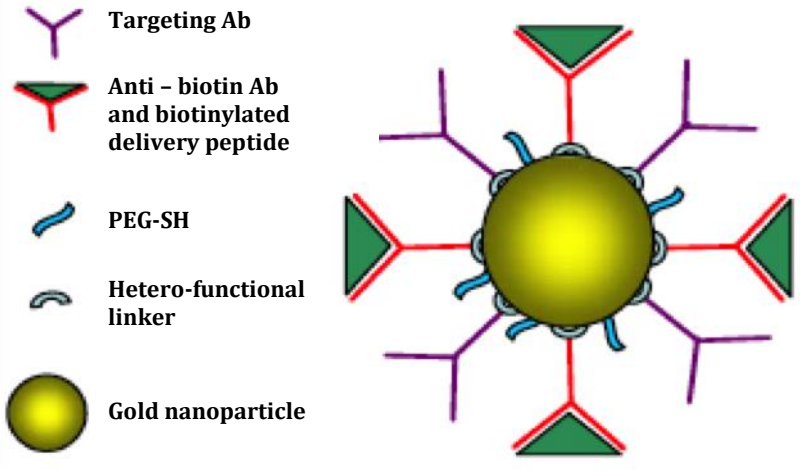

Figure 2-3: Multifunctional AuNP designed for targeting, delivery and imaging. [Adapted from 55]

2.5.2 Drug delivery

In addition to cell labeling, AuNPs may also serve as drug vectors if designed to be stable in the circulatory system, but lose stability when the target organ is reached [58]. Since typical nanostructure synthesis involves citrate-stabilized intermediates, the overall surface charge tends to be negative [12]. This allows for favorable charge interactions with the amine domains of proteins and results in surface adsorption of proteins. This in turn, results in an improved ability to cross cell membranes and therefore an improved ability to deliver coupled drug molecules to intracellular spaces. Additionally, it is this adsorption ability that is used to conjugate the various antibody markers to the nanostructure surface as mentioned previously. As a result, highly specific targeting can be achieved using surface markers that may be unique to the target in question.

The discussed membrane interactions are only relevant if the drug vectors are able to reach the target site. As a result, the EPR effects discussed above become necessary considerations when designed delivery systems for targeting tumors. For nuclear targeting to be possible, particle influx through nuclear pores must be possible, which only occurs for particles that are less than 40nm in diameter [59]. Work by Feldherr et al. has shown the utility of gold nanoparticles as efficient vectors for both intracellular and nuclear delivery [60-62]. Conjugating known nuclear localization signals to particle surfaces results in facilitated particle uptake via receptor-mediated endocytosis [63]. Other examples of drug delivery vector design have involved the use of AuNP-peptide complexes to create multifunctional vectors. Tkachenko et al. used bovine serum albumin coupled to AuNP surfaces to successfully target HepG2 human hepatocarcinoma cells [30]. Future work may incorporate the therapeutic applications discussed here with the gold-mediated mechanisms described in this work.

2.5.3 Imaging

Gold nanoparticles are promising candidates in photo-diagnostic applications because of their tunable optical properties, ease and robustness of conjugation and appreciable biocompatibility [18, 58, 64]. For the past two decades, detection methods have been based on either particle aggregation, changes in local refractive index or vibrational differences in surface-enhanced Raman scattering [54]. Colorimetric assays, for instance, based on a red shift upon nanoparticle aggregation, are extremely sensitive in comparison to conventional methods based on molecular fluorophores. Mirkin and others have taken advantage of this method to detect sub-picomolar levels of oligonucleotide, DNA binders and cancer cells *in vitro.* An example of these favorable aggregation interactions can be seen in Fig. 2-4, from the works of Mirkin et al. [65-67]. Although the use of gold nanoparticles is limited in clinical settings due to specificity and toxicity concerns, it is conceivable that improvements in those areas – several of which are discussed above – may result in these techniques being used to determine nanoparticle uptake during the various gold-mediated radiation studies described here.

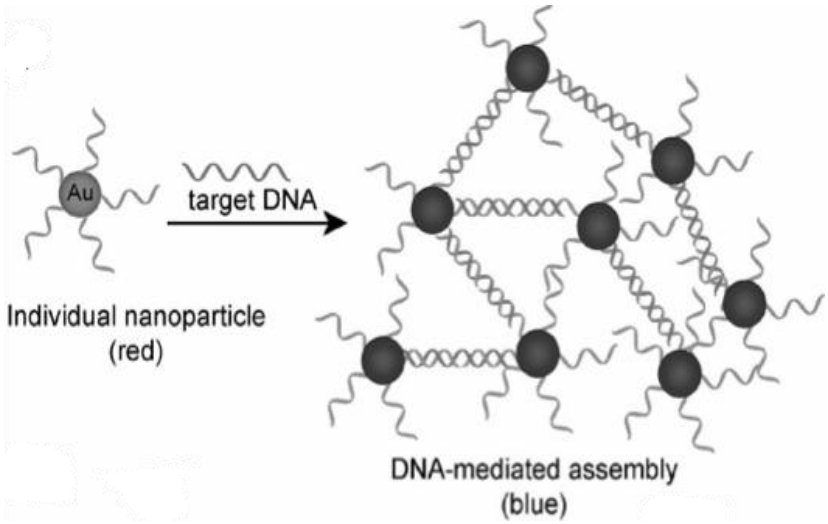

Figure 2-4: Colorimetric assay using gold nanoparticles. Images are based on aggregation-dependent red-shift [65]

2.6 Studies using gold as a radio-sensitive agent

The idea of using a high-Z element as a radio-sensitizer is not a new one. Matsudaira et al. first demonstrated the use of iodine as a radio-enhancer more than three decades ago [68]. Since then, there has been considerable interest in determining the specific impact of iodine as a contrast material for both imaging and therapeutic purposes with several *in vivo* and simulation studies generating promising results [69-72]. Additional work has been to study the effects of gadolinium-based contrast agents as well to study the possibility of using the platinum-based chemotherapy agent Cisplatin as a possible contrast agent [72, 73]. While each of these studies has shown promise for the use of contrast agent mediated radiotherapy, several clinical issues arise when attempting to design treatment options using iodine contrast agents (low molecular weight leading to rapid clearance), Cisplatin (inherent cytotoxicity), or gadolinium contrast agents (low atomic number). As a result, recent interest in using contrast media to improve radiation response has focused on the use of gold as the contrast agent.

Gold has shown promise in radiation treatment applications as a radiosensitive material for dose enhancement in both surface and deep-tissue tumors. The high-Z nature of gold (Z=79) means that it should have favorable interaction cross-sections for all scattering types compared to normal tumor tissue that is comprised primarily of oxygen (Z=8), hydrogen (Z=1), carbon (Z=6), and nitrogen (Z=7). Therefore, it is theoretically possible to use site-specific gold to act as a type of amplifier for incident radiation as it would have a much higher affinity for photoelectric and scattering interactions, and correlated energy deposition, compared to the surrounding tissue. Previous studies have shown increases in local photon absorption of up to three orders of magnitude through the photoelectric effect using iodine and gadolinium [70, 71, 74, 75]. Using gold as the contrast agent should yield similarly beneficial cross section improvements. Given below is a brief review of the in vivo and simulation studies done in which a high-Z element has been used a radiosensitive agent.

2.6.1 *In vivo* and *in vitro* murine studies

Hainfeld et al. reported what was potentially the first and most significant *in vivo* study of using gold as a radiosensitive agent in 2004 [76]. Mice displaying mammary carcinoma cells were injected with 1.9 nm gold nanoparticles (AuNP) and tumor accumulation of 7 mg of gold per gram of tumor tissue was observed. Irradiation using 250 kVp x-rays resulted in a 66% increase in one-year survival rates of cancer-bearing mice when compared to irradiation without the implanted gold. Illustrating proof-of-concept, this study was followed by several subsequent studies that attempted to validate these conclusions and further explain the mechanisms involved.

Hainfeld et al. followed up their initial work with a subsequent murine study aimed at determining the utility of gold nanoparticles as contrast agents for x-ray imaging purposes [77]. Using similarly sized AuNP (1.9 nm), the study showed that there was extensive gold retention in the tumors after blood clearance due to the EPR effects. Since gold has a three-fold higher absorbance at 100 keV compared to iodine, the study surmised a ten-fold or more increase in contrast gain when using gold as the contrast media. The implication of this study are vast as it points to the possibility of using gold as both a real-time imaging contrast agent as well as a radiosensitive agent after tumor localization.

The clinical applications of small-diameter nanoparticle studies like the two Hainfeld studies were cast in doubt by the work published by Butterworth et al. that demonstrated that 1.9 nm AuNP cause cell death by multiple mechanisms including increased apoptosis due to oxidative stress [78]. This observation had a two-fold implication. On the one hand, it presented a problem when attempting to quantify the radio-sensitivity associated with small-diameter AuNP since cell death could be attributed to non-radiation related events. On the other hand, the posited oxidative stress would result in a reduction of tumor hypoxia and therefore an increase in the inherent radiation sensitivity of the tumor. Ultimately, the work confirmed earlier studies that stated that small diameter gold nanoparticles are toxic leading to the conclusion that

larger diameters must be investigated for gold-mediated radiotherapy [18, 44]. These findings confirmed the work published by Chen et al. describing the upper limit of the toxicity window, but were in disagreement on the lower bounds described earlier in Fig. 2-1.

In an effort to elucidate the effects of larger diameter AuNP, and to clarify the disagreements on nanoparticle size in earlier studies, Chithrani et al. demonstrated the effects of nanoparticle size on their effectiveness as radiosensitive agents [79]. Cellular uptake and corresponding radio-sensitivity of AuNP of three different diameters (14 nm, 50 nm, and 74 nm) were compared *in vitro* for both low- and high-energy photon beams. The study, reiterating previous work, showed maximal cellular uptake for 50 nm gold nanoparticles [12]. Cells were then irradiated with 105 kVp, 220 kVp, 660 kVp, and 6 MVp photon beams and the radiation-induced double-stranded DNA breaks were quantified using different cell-culture assays. Dose enhancements of 66%, 43%, 18%, and 17% were observed respectively indicating that the increase in AuNP cellular uptake drastically improves radiation response even at higher photon energy levels. The results of this study directed the decision to use 50 nm gold nanoparticles for the purposes of the detailed model described later in this work.

2.6.2 Monte Carlo simulations

In order to quantitatively corroborate the results of the above-mentioned *in vivo* studies, a series of Monte Carlo simulation studies have also been carried out for various contrast media. These studies have focused on clarifying the mechanisms inherent in contrast media dose enhancement and have mostly assumed the physical parameters described in the *in vivo* studies mentioned.

Though not related to gold, it is useful to mention a simulation study published by Robar et al. which examined the possibility of dose enhancement using gadolinium and iodine contrast agents [73]. The use of MeV photon beams was explored using Monte Carlo simulations, and the effects of beam flattening filters and contrast agent

concentrations were studied. Although dose enhancement of up to 70% was seen with contrast media concentration of 1g/ml, such tumor concentrations are not clinically feasible. For the potentially achievable concentration of 30 mg/ml, dose enhancement of up to 15.8% and 23.1% was seen for iodine and gadolinium respectively using a 2 MeV photon beam. Smaller increases (3.9% and 4.4% respectively) were observed for high quality beams in the 10 MeV – 24 MeV range. Although using less effective contrast agents, this study provided a quantitative framework in which to study future contrast materials.

Following the seminal work by Hainfeld, and following the example of the Robar study, a series of Monte Carlo simulations have been conducted using various computer codes, target geometries, and contrast media. Although the results have varied significantly depending on the specifics of the study, each simulation has borne out, to some degree, the general claim that gold nanospheres can act as radiation enhancing agents in clinical treatment settings and that they are more effective that previously studied gadolinium- and iodine-based materials.

One of the first studies following Hainfeld's work was conducted by Cho to attempt to quantitatively validate the Hainfeld study [74]. Three different photon energies were tested for teletherapy applications and one brachytherapy setup was modeled as well. Relatively modest dose enhancement was achieved for 4 MeV and 6 MeV photon beams (3.2% and 7.4% respectively at maximum gold concentrations of 30 mg/g). However, a dose enhancement of between 200% and 550% was seen for a 140 kVp photon beam (7 mg/g and 30 mg/g tissue-gold concentrations respectively). Such significant dose enhancement has not been replicated in subsequent models and it has been theorized that neglecting to model discrete gold nanoparticle distributions may be the cause for the over-enhancement of the recorded dose [80]. For the brachytherapy model, dose enhancement of up to 30% was measured, and an improvement of at least 2% was observed for every gold concentration when compared to similar concentrations of gadolinium contrast agents.

A subsequent study by Cho et al. was then published that sought to more precisely define the effects of AuNP in brachytherapy models [81]. Using a 50 kVp photon source, a I^{125} source, and a Yb^{169} source yielded macroscopic dose enhancement ranging from 44% to 116%. Using a tumor-gold concentration of 18 mg/g, the broad photon energy spectrum of Yb^{169} yielded the highest dose enhancement suggesting that the photons may be interacting at multiple orbital-edge energy levels.

Most recently, Garnica-Garza assumed CM concentrations of 10 mg/g and used the electron-photon coupled transport MC code PENELOPE with an optimization algorithm to obtain a dose enhancement of 38% for a prostate cancer model [72]. This model assumed a uniform concentration of gadolinium in the tumor, and explored contrast agent leakage, and non-uniform loading of the tumor. While using gadolinium instead of gold, this study did attempt to model a physiologically accurate simulation geometry and measure doses delivered to non-tumor volumes.

The results of these published Monte Carlo studies were used to direct the development of the MC simulations described in this work. The code, geometric models, and physical parameters are described in the chapters that follow. The preliminary model assumes the physical parameters of the first Hainfeld study, and extends the work done by Cho by detailing several teletherapy schemes. The effects of varying photon beam energy, *in situ* gold concentration, and tumor depth are explored in detail. The detailed model integrates the cell uptake results published by Chithrani et al. and attempts to quantitatively model the *in vitro* results described in the study described earlier. The effects of non-homogenous gold distribution and lack of nanoparticle specificity are also explored in this model. Both Monte Carlo models represent an improvement in scope and detail compared to the studies referenced above and should provide a detailed framework for *in vivo* and phantom studies to follow.

Chapter 3

Motivation for MCNP5 simulations of radiation-tumor interaction

In order to determine the effects of using gold to improve dose response at a tumor site, several Monte Carlo simulations were run using MCNP5 – the particle transport code developed and maintained by Los Alamos National Laboratory [82]. Several published studies have shown an *in vivo* improvement of tumor mitigation in murine models accompanied by relatively limited quantitative modeling data. As a result, a comprehensive MC model was developed in order to try and quantitatively corroborate the qualitative results shown in the Hainfeld and Chithrani studies [76, 79] and the quantitative results shown elsewhere [74, 81].

A preliminary model was first developed to clarify the variables having a significant impact on the radiation dose delivered at a specified tumor site. Hainfeld reported possible dose enhancement at *in situ* gold concentrations of 0.7% - 1.2% by mass [76]. Additionally, Robar et al. reported contrast media concentrations approaching 3% by mass [73]. These physical parameters were used as the framework for the preliminary model. Cho et al. only reported source strength dependence for brachytherapy applications [74]; the preliminary model described in Chapter 4 illustrates the effects of varying the energy spectra of external photon beams. Work done by Van den Heuvel discussed beam energy considerations but used water as the background media [83]. The results obtained in this work should reflect a more accurate biological model as described in Chapter 4.

The majority of reviewed MC studies have measured the effects of the gold concentrations originally published in the Hainfeld studies. However, the Chithrani study showed significant improvement in cellular uptake with larger (50 nm) nanospheres, and subsequently reported different gold concentrations [79]. As a result, the detailed model factored updated *in situ* gold concentrations, as well as, non-homogenous gold distribution, resulting from lack of nanoparticle penetration, and non-specific

nanoparticle targeting. The relative importance of each component was studied to determine the significant factors.

Although the specifics of each model differ, the physical quantities measured and the method of comparing gold-containing tumor tissue, bare tumor tissue, and healthy tissue remain the same. Internal material specifications differ among models depending on the variable being tested, but the geometry for each case assumes a rectangular prism of tissue. A parallel beam of photons incident on one face of the prism is simulated such that the tissue slabs present orthogonally to the beam axis. Detailed diagrams of the geometries used in each model are given in Appendix A. MCNP5 allows for the measurement of various tallies in given target cells and three different tallies were used over the course of these simulations. The results for the F4 and F6 tallies were recorded for the preliminary models, while the results for the modified F8 tally were recorded for the detailed model. A description of the tallies used is given below.

3.1 MCNP5 Tallies

The first tally used in this work is the F4 tally that measures particle flux due to each incident photon in units of particles/cm^3. Equation 3-1 describes the physical quantity measured and values are scored as particle weight multiplied by track-length per unit volume. Since $N(\vec{r},E,t)ds$ can be interpreted as the track length density, the average flux can be estimated by summing the track lengths over all photon energies over a specified volume. Tracking a large number of particle histories results in a large number of contributions to this tally leading to increased reliability for the track length estimate.

Table 3-1: Relevant equations for F4 particle flux tally

Tally	Score	Physical quantity	Eq.
F4	$W\frac{T_l}{V}$	$\bar{\phi}_V = \frac{1}{V}\int dE \int dt \int dV \int d\Omega\, \psi(\vec{r},\Omega,E,t)$ $= \frac{1}{V}\int dE \int dV \int ds\, N(\vec{r},E,t)$	(3-1)

The second tally used is the F6 tally that measures energy deposition per unit mass in each tissue cell by using track length measurements convolved with a heating function as given by Equation 3-2. This heating function is obtained by summing the average energy deposition for all particle interactions at a given particle energy and is given by Equation 3-3. As mentioned earlier, using this heating function method with the simplified physics model is analogous to applying the KERMA approximation discussed in Chapter 1 since the electrons are assumed to deposit their energy locally. Energy deposition for this tally is measured in units of MeV/g and the tally is scored as particle weight multiplied by track length and atomic density per unit mass weighted by the interaction cross-sections and the heating function.

Table 3-2: Relevant equations for F6 energy deposition tally

Tally	Score	Physical quantity	Eq.
F6	$W\,T_l\sigma_t(E)H(E)\frac{\rho_a}{m}$	$H_t = \frac{\rho_a}{m}\int dE\int dt\int dV\int d\Omega\;\sigma_t(E)\,H(E)\,\psi(\vec{r},\Omega,E,t)$	(3-2)
		$H(E) = E - \sum_{i=1}^{3} p_i(E)\left[\bar{E}_{i,out}(E)\right]$	(3-3)

Finally, the third tally used was the modified F8 tally that measures energy deposition by performing a pulse height count. Instead of recording particle track length, the results of this tally are analogous to the counts recorded by a physical detector. The tally maintains an energy account for each cell and adds or subtracts energy based on the number and energy of particles crossing the boundaries of a cell. Since the kinetic energy of each particle is recorded, neglecting electron transport results in the KERMA approximation while accounting for electron transport should result in a more physically accurate measurement of effective dose if the inherent microscopic approximations in MCNP5 are overcome. The results from this tally were divided by the mass of each cell to obtain units of MeV/g analogous to those obtained from the F6 tally. Equation 3-4 describes the calculations performed to generate the tally results in MCNP5.

Table 3-3: Relevant equation for *F8 modified pulse height tally

Tally	Score	Physical quantity	Eq.
*F8	$E_D \times W_C$	Pulses binned at discrete energy levels	(3-4)

The constants and variables used in Equations 3-1 through 3-4 are given in Table 3-4 below. The tally values for healthy tissue, in the absence of gold, were taken to be the baseline against which the various other simulations were compared to calculate the dose enhancement factor using Equation 3-5 given below.

Table 3-4: Variables and constants used to calculate F4, F6, and *F8 tallies

W	=	Particle weight
W_C	=	Collective weight for a particle history
T_l	=	Track length (cm)
V	=	Volume (cm^3)
$\vec{r}, \hat{\Omega}, E, t$	=	Position vector (cm), direction vector, energy (MeV), time (10^{-8} s)
$\bar{\phi}_V$	=	Average flux in a cell
H_t	=	Total energy deposition in a cell (MeV/g)
$\sigma_t(E)$	=	Total microscopic cross section (barns)
$H(E)$	=	Heating number (MeV/collision)
E_D	=	Total energy deposited by a particle history
ρ_a	=	Atomic density (atoms/barn-cm)
m	=	Cell mass (g)
ψ	=	Angular flux
$p_i(E)$	=	Probability of interaction at energy *E* $i=1 \rightarrow$ Compton scattering $i=2 \rightarrow$ Pair production $i=3 \rightarrow$ Photoelectric absorption
$\bar{E}_{i,out}(E)$	=	Average exiting gamma energy for interaction *i* at energy *E*.

Although only three main photon interactions are listed at the bottom of Table 3-4, other interaction probabilities may be considered for photon energies high enough to have significant cross-sections for those interactions.

3.2 Effective Dose Enhancement Factor

The primary quantitative tool used to analyze the results of the difference cases was the calculation of a localized Dose Enhancement Factor (DEF). This factor was determined by comparing the amount of energy deposited in each slab in the presence of gold (E_{Au}) against the baseline (E_B). This ratio was then used to determine whether adding gold to the tumor site had any effect on improving the radiation response at the tumor site. The equation used to calculate DEF is given below.

$$DEF = \frac{Energy\ deposited\ in\ tissue\ layer\ containing\ gold}{Energy\ deposited\ in\ bare\ tissue\ layer} = \frac{E_{Au}}{E_B} \qquad (3\text{-}5)$$

The results of Equation 3-5 were then recorded as a function of distance in each simulation and the results were plotted below for the different variables tested. A DEF value of 1 indicates no change in the amount of dose received compared to normal, healthy tissue. A DEF value greater than 1 indicates an increase in the effective dose for a particular tissue cell, while a value less than 1 indicates a decrease in the dose.

3.3 Preliminary Monte Carlo Model

The preliminary model used to obtain the results discussed in Chapter 4 is an approximation of actual human physiology. However, the geometry used should be sufficient to demonstrate the significant physics applicable for this treatment approach, and to evaluate the geometrical effects on effective dose estimates. In order to model a deep-tissue tumor, simple slab geometry was used. A rectangular prism with a side length of 20 centimeters was used to represent the subject tissue (phantom) as shown in Fig. 3-1. Although the size of the phantom exceeds most physiological dimensions, it was chosen in order to get insight on effects of tumor depth on dose enhancement. In order to determine any depth dependence, the phantom was split into 2 cm thick slabs with identical material properties and dimensions. All tissue compositions were

referenced from Report 89 of International Council of Radiation Protection and are summarized in the attached appendices [84]. For the purposes of this model, the composition of tumor tissue was taken to be the same as that of healthy muscle tissue. As a result, the only differences in material composition for any given simulation of this model were due to the presence of a specified concentration of gold within a slab. The gold was assumed to be colloidal and distributed homogenously throughout the specified tissue slab.

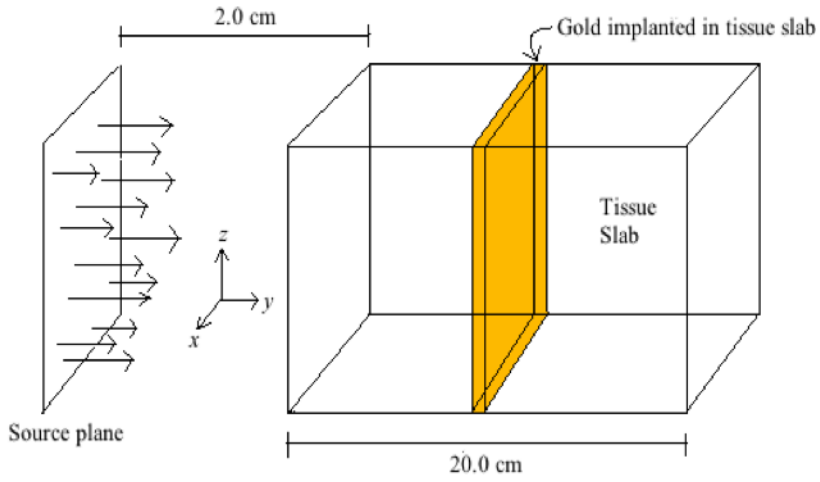

Figure 3-1: Geometry used in preliminary model MCNP simulations

Three different simulations were run using this model. In each case, one of the variables was modified in order to ascertain the relative effects of the variable on the dose received by the target cells. The variables tested in the preliminary model include beam energy, tumor depth, and *in situ* gold concentration. The results of the preliminary models were used to guide the development of the detailed model, as the relevant boundary conditions for the variables were determined. For the purposes of the preliminary model, the thick-target bremsstrahlung (TTB) approximation is used and primary electrons are assumed to slow down locally. However, secondary photons are not ignored in this model making it better than the simple KERMA approximation. Electron transport is not ignored in the detailed model, as described below, which furthers improves the physical accuracy of the model.

3.4 Detailed Monte Carlo Model

The depth dependence simulations were designed to illustrate the importance of limiting the amount of tissue present between the incident surface and the targeted tumor. Since the gold contrast media effectively shields the tissue behind the tumor from excess radiation, the photon beam deposits significantly less energy after encountering the tumor volume. For these reasons, this detailed model does not vary the depth of the simulated tumor with the assumption that clinical teletherapy schemes would be designed to make use of the most efficient beam geometry to minimize the depth of the tumor. However, the overall size of the tissue model is reduced to better approximate physiological dimensions and a 0.5 cm skin layer is added. Additionally, the resolution of the model is improved to include 1 cm slices throughout and further improved to 0.25 cm sliced within the tumor boundaries. As a result, the overall model geometry is a refined version of the preliminary model and is shown in Fig. 3-2 below.

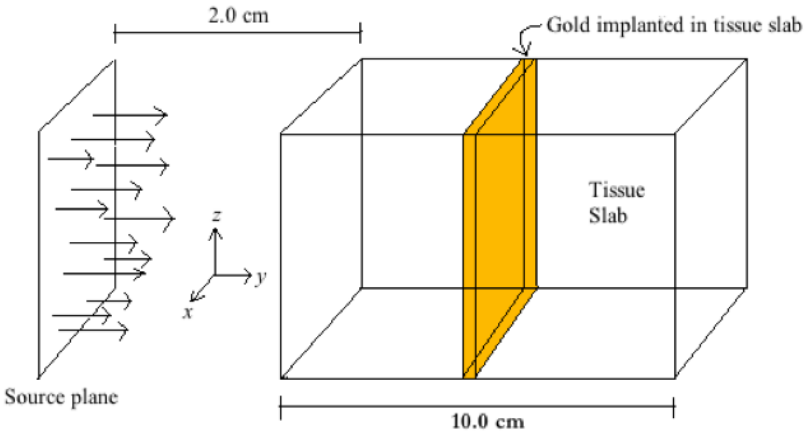

Figure 3-2: Geometry used in detailed model simulations

In an effort to improve the physical accuracy of the detailed model, both photon and electron transport was taken into account. Both primary and secondary photons are accounted in this model since primary electron transport was fully tracked. This results in significant improvement over the preliminary model where secondary photons were tracked but electrons were not, and further improvement over a KERMA approximation where all electron energy is locally deposited. As described above, the modified F8 tally

was used to model the improvement in the physical approximations as all energy deposition in a target cell is recorded. As both photon and electron transport are included, the results of this tally should be more accurate than the earlier assumptions. In order to gauge the level of improvement, the concentration dependence model was run using the new geometric parameters mentioned above. Higher gold concentrations were calculated from the descriptions of the Chithrani study discussed in detail in Chapter 5.

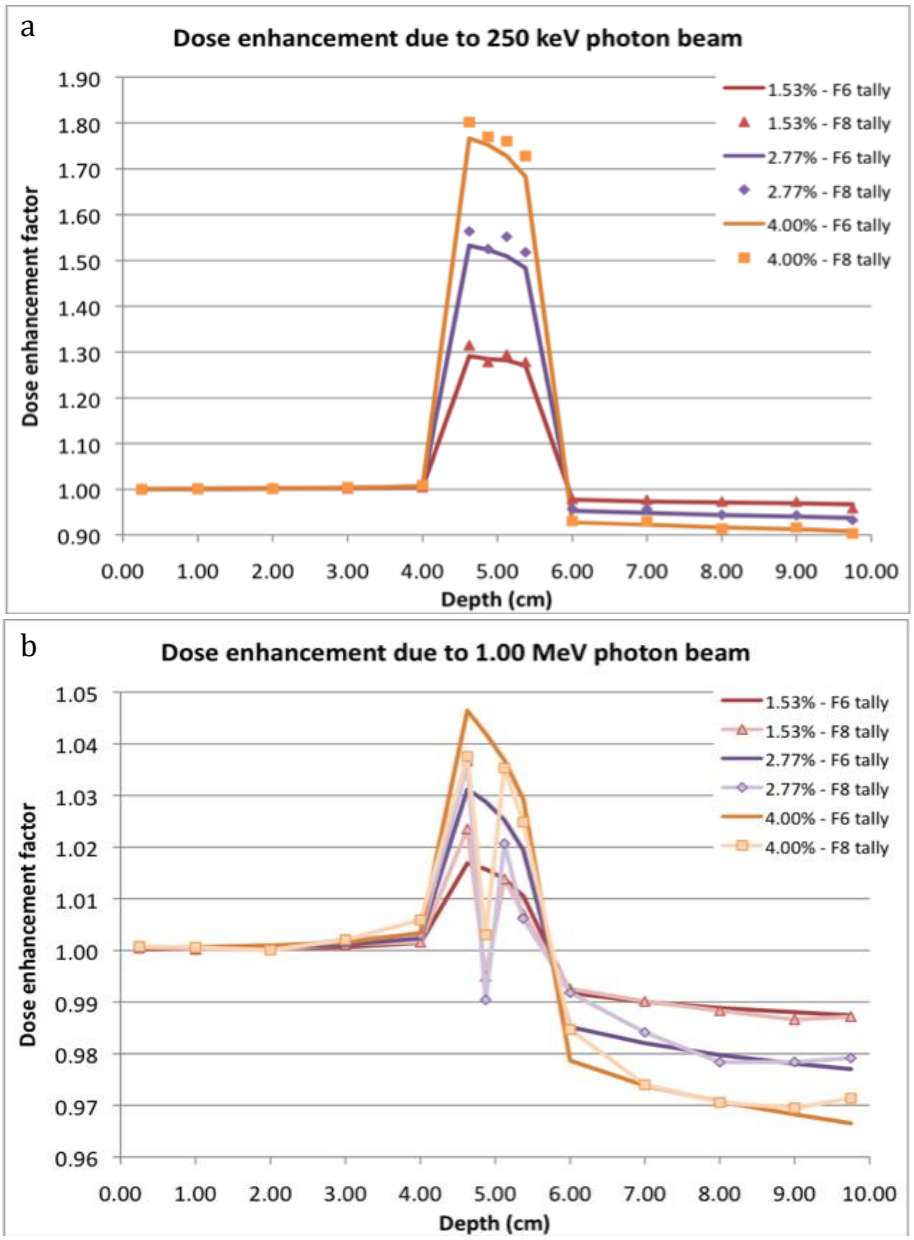

Figure 3-3: Differences in DEF values calculated using F6 and F8 tallies. (a) 250 keV photons , (b) 1.00 MeV photons.

The results of this simulation are given in Fig. 3-3 above. It is important to note that the width of the peaks shown is an artifact of the plotting routine and is not physically relevant. Plotting additional points in the 4.00 – 4.50 cm and 5.50 – 6.00 cm depth ranges would result in a significantly sharper peaks as gold is only present at depths of 4.50 – 5.50 cm. As evident in Fig. 3-3a, using the *F8 tally yields higher energy deposition by each tracked photon in the tissue region with implanted gold when using 250 keV photons. However, using 1.00 MeV photons results in the *F8 tally drastically underestimating the energy deposition as seen in Fig. 3-3b. The reason for this inconsistency stems from the fact that the F6 tally is an average over all particle histories in a given simulation while the *F8 tally records individual events instead of averages. Fluctuations in energy loss rates are not microscopically correlated to account for the production of secondary photons. The target cell may be large enough to smooth out these fluctuations for the 250 keV photons, while that is not the case for the 1.00 MeV photons. In the absence of microscopically accurate event modeling, the results given for the simulations that follow use the F6 tally for all energy deposition calculations. Future work may refine the geometric parameters of the study to such an extent that microscopic interactions are simulated accurately. The *F8 may be used in such future work to accurately measure dose deposition.

The following chapters discuss the physical and geometric parameters for each model in detail followed by the results that were observed. All figures shown are not to scale and included for ease of reference only. Detailed geometric figures for the various simulations are included in Appendix A. Sample input files used to for each MCNP5 simulation are included in Appendix B along with sample output files. Each case included 1.5×10^5 particles histories and the results that follow are averaged in terms of each incident particle. As a result, while the energy scale given on the figures below is in the eV range, the results can be scaled for any beam intensity as the number of photons available in a typical photon beam can be varied for specific treatments.

Chapter 4

Preliminary model for gold-mediated effective dose enhancement

The preliminary model was designed to provide a benchmark set of results to which various parametric modifications could be compared. Since the gold concentrations levels were maintained at values used in published *in vivo* studies, the quantitatively obtained effective dose enhancement values can be correlated to the enhanced survival rates seen in those studies. In addition, these results should compare favorably against other Monte Carlo studies of effective dose enhancement as described earlier in Chapter 2.

Given below is a description of each of the simulations run for the preliminary model along with a representation of the overall geometric setup used. The main quantitative tools used for comparison are the effective Dose Enhancement Factor described in the previous chapter as well as a measure of relative flux. In order to determine the relative intensity of photon flux in the presence of gold, a calculation similar to that involving the dose enhancement factor was carried out. The governing equation for these calculations is given below.

$$Relative\ flux = \frac{Photon\ \ flux\ \ in\ \ gold-bearing\ \ cell}{Photon\ \ flux\ \ in\ \ cell\ \ with\ \ no\ \ gold} \tag{4-1}$$

4.1 Photon energy dependence

The first variable tested was the strength of the beam incident on the side of the tissue slab. The gold concentration in the 'tumor' slab was kept at a constant 0.7% by mass that is consistent with the Hainfeld murine studies that documented a demonstrable improvement in treatment when tumor gold concentration was 7 mg per gram of tumor tissue (7 mg/g). As no appreciable cell death was observed in the absence of applied

radiation for any of the concentrations used in the Hainfeld study, it is assumed that potential cytotoxicity issues are not significant and are ignored for the purposes of this work. Additionally, the location of the 'tumor' slab was kept at a constant depth of 9 centimeters. Although slabs are 2 centimeters thick, the recorded values were plotted at the midpoint of the slabs for consistency. As a result, the target slab was located between 8 and 10 centimeters away from the beam-incident surface as shown in Fig. 4-1.

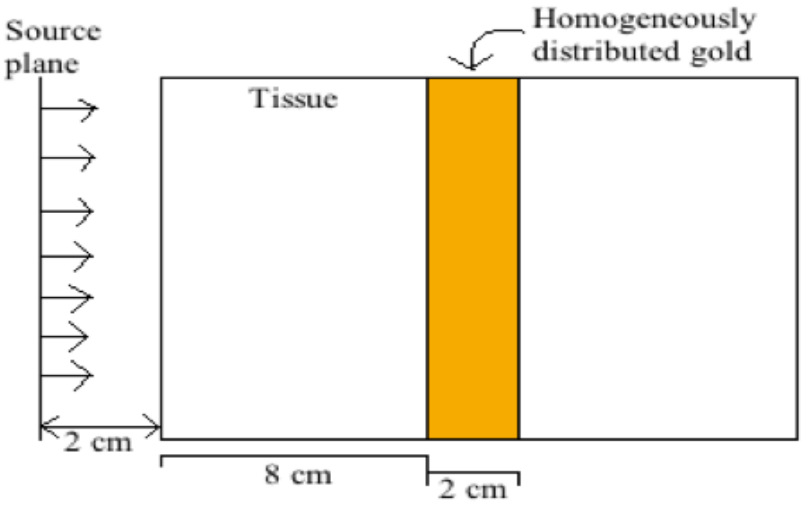

Figure 4-1: Representative geometry for photon energy dependence

The results of this simulation were used to bracket the tested beam energy levels based on a dose enhancement of at least 1% $(DEF \geq 1.01)$. This was the only filtering criterion used at this time and no comment or consideration is given to the clinical significance of the resulting range of beam energies. Discussions of clinical significance and application are deferred to the discussion of the more detailed simulations performed. Subsequent simulations were designed with more precise spatial and energy parameters after reviewing the results of the first preliminary model. These preliminary results along with their relative importance and physical significance are given below. For the photon energy dependence model, the flux (F4) and energy deposition (F6) tallies were recorded for photon energies ranging from 100 keV to 2.00 MeV. While most common radiotherapy procedures use photon beams with considerably higher energy levels, as the

results that follow demonstrate, the best dose enhancement is seen at lower energy levels due to the fact that mass attenuation coefficients for tissue and gold differ significantly in that range as discussed earlier and seen in Fig. 1-6.

Mass attenuation coefficients begin to diverge again at photon energies higher than 5 MeV, which lends credence to the results reported in the literature using higher energy beams. However, generation of megavoltage beams requires expensive linear accelerator systems not found in most hospitals, and so the decision to restrict the energy window was motivated by availability of said beams in common hospital settings. Alternatively, the characteristic gamma emissions from a Co^{60} source (1.17, 1.33 MeV) are easier to obtain and may be available for widespread use. In order to provide a more comprehensive set of energy-dependent results, the range of beam energies was expanded to cover the characteristic Co^{60} energies.

It is important to note that each of the photon sources described in the Monte Carlo models that follow is a mono-energetic source. In practice, photon sources generally have a broad energy distribution and this characteristic may be incorporated into more detailed models that may follow this work. However, it is possible to apply filters on x-ray machines commonly available in hospitals to generate a photon beam that resembles a mono-energetic source. Further work may be warranted to assess the specific effects of filter-reduced photon flux on the results discussed below.

Energy levels for the first simulation were varied from 250 keV to 2.00 MeV with an interval step of 250 keV. An additional 100 keV source was included to better capture the effects of using photon energy near the K-edge of gold at 80.7 keV. Fig. 4-2 plots the photon flux profile in the tissue phantom as a function of tissue depth for each of the photon energy levels modeled.

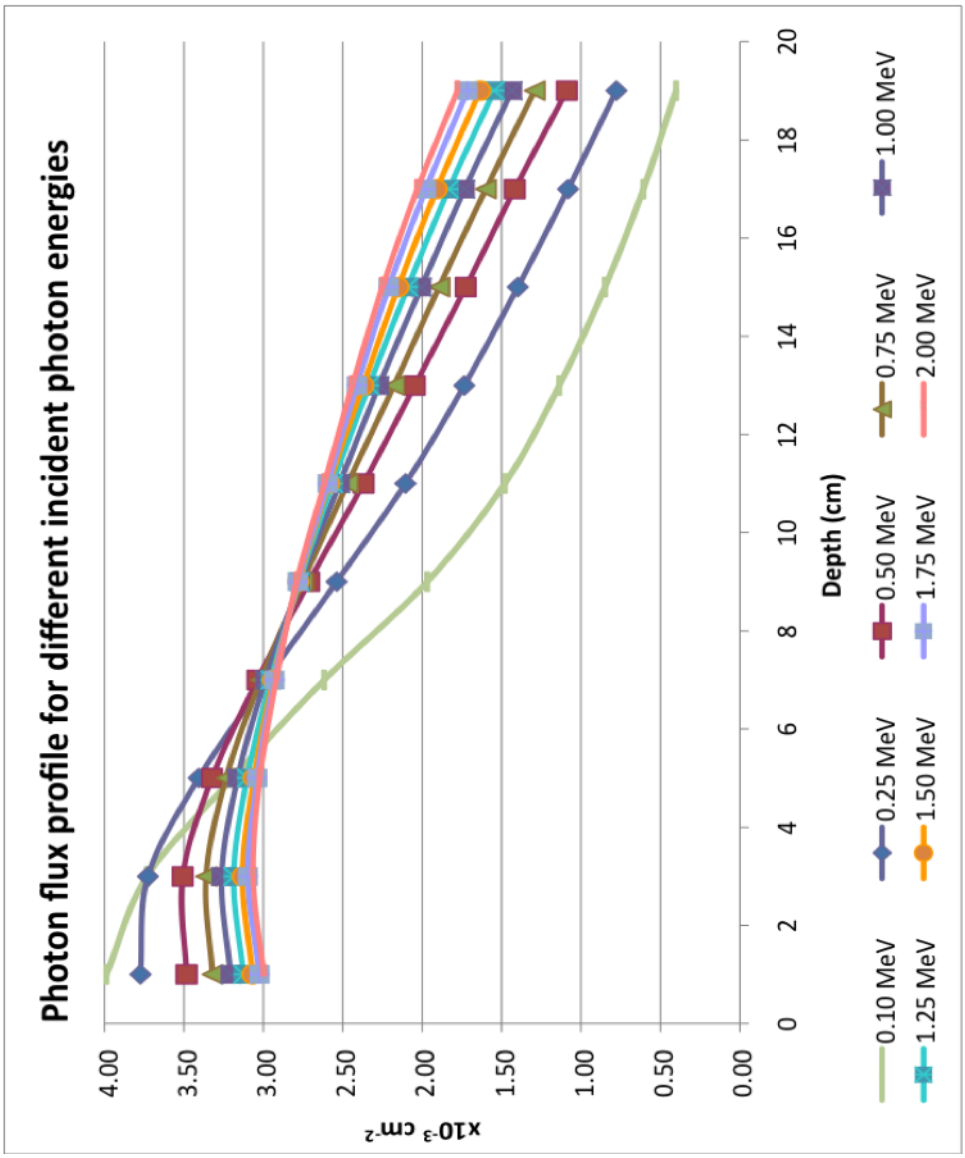

Fig 4-2: Photon flux profile for different incident photon energies. Beam attenuation described by track-length estimate of photon flux for various photon energies

As seen in Fig. 4-2, the flux drops as a function of depth as would be expected due to beam attenuation by the tissue. Similarly, the changes in attenuation are important as they point to the dominant physical mechanisms at work in the slabs of tissue. The flux follows a decay pattern that is consistent for each of the photon energies modeled with the magnitude of the decay increases as the photon energy decreases. Since attenuation coefficients follow a similar decay scheme, these results are as expected. The distinctly steeper decay for the 100 keV photon beam may be due to the fact that the photon beam energy is approaching K-edge of the tissue-gold mixture. The increase in cross section for photoelectric interactions may explain the increase in photon attenuation in the tissue phantom.

The changes in attenuation based on the energy of the incident beam can also be illustrated using a relative measure as in Fig. 4-3 below. Here, the flux due to the different beam strengths is shown relative to the flux in a tissue sample with no gold – a value of 1.00 would represent no change. For the case of the 100 keV photon beam, the relative flux drops drastically in the gold-containing tissue cell – centered on the 9 cm mark. A decrease of 9.1% is seen when comparing the flux before and after the beam encounters the tumor gold. The decrease in relative flux is significantly less pronounced for the higher energy beams – the drop over the same span of tissue depths is only about 2.2% for the 250 keV beam. As beam energy increases, the drop in relative flux is further reduced to less than 1% (when using the 2.00 MeV beam) resulting in a loss of utility as far as a dose-enhancement response is concerned. This loss of utility directly corresponds to the fact that mass attenuation coefficients for gold and tissue are virtually identical at that photon energy as seen in Appendix D. Using photon energies higher than 5 MeV may yield an additional window of utility as attenuation factors for gold and tissue begin to diverge at those energy levels. However, discussion of megavoltage photon beams is left for future consideration.

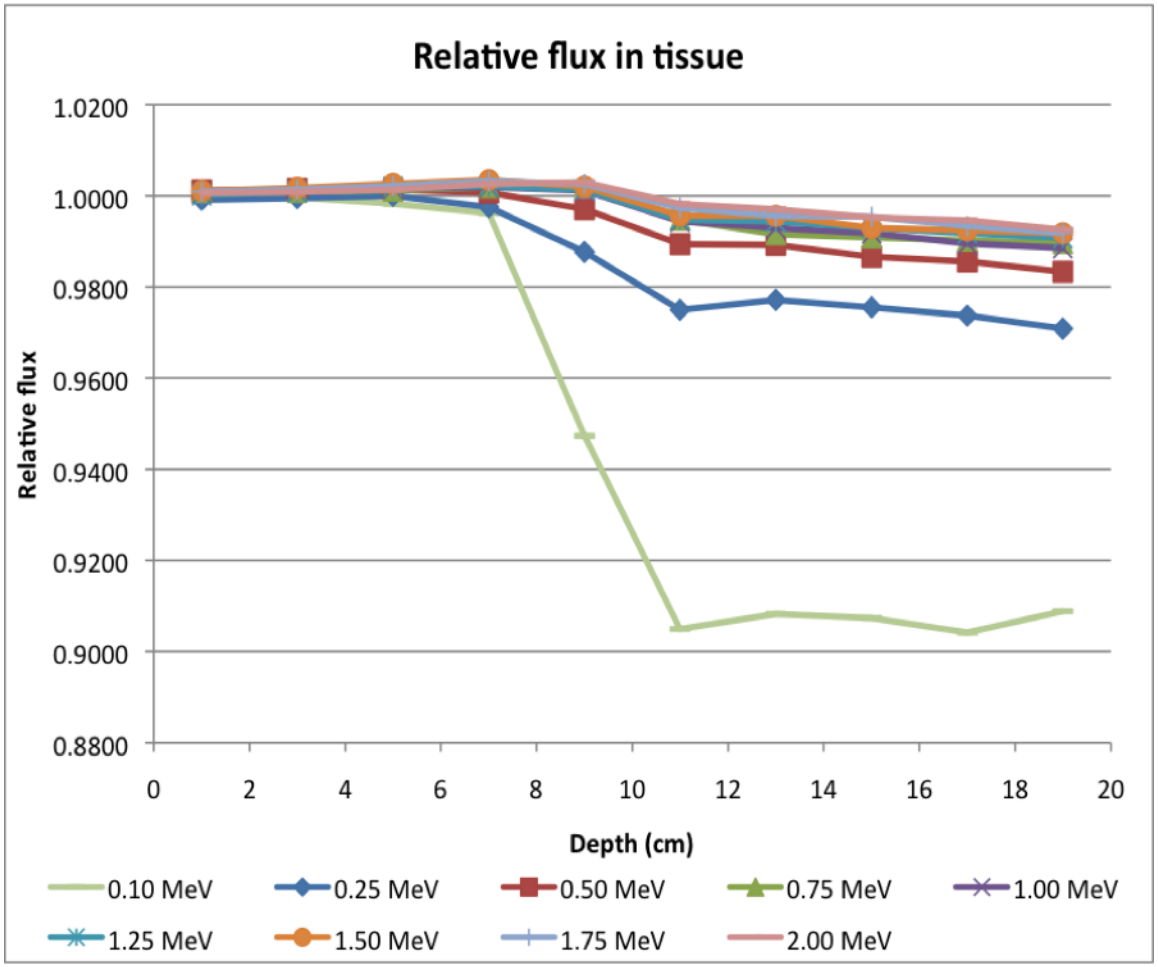

Figure 4-3. Relative flux profile for different incident photon energies. Attenuation described in terms of relative photon flux as a function of tissue depth for different photon energies.

Corresponding to the depth-dependent flux attenuation that can be seen in Figs. 4-2 and 4-3, the energy deposition as a function of tissue depth has an overall negative slope as well as seen in Fig. 4-4. The slope of the energy-depth curve remains relatively constant for photon energies higher than 1.00 MeV implying that there is no significant improvement in effective dose enhancement. Meanwhile, sub-MeV energy beams show peaks in the energy-depth curve corresponding to an increase in the effective dose deposited in the gold-bearing tissue cells. In order to better highlight this difference, a dose enhancement factor was calculated for each energy level using Equation 3-4 and the results are plotted in Fig. 4-5. As can be seen, there is a very significant increase in localized energy deposition due to the presence of gold at the tumor site. DEF values ranged from 1.62, for the 100 keV beam, to 1.003, for the 2.00 MeV beam. These results were used to bracket the energy range of further models since MeV photon energies resulted in dose enhancement of less than 1% and were determined to be ineffective for teletherapy in the scope of this study.

The most significant attenuation was seen for the 100 keV beam since proximity to the K-edge of gold results in a photoelectric effect interaction cross section that is several orders of magnitude higher compared to the 250 keV beam. However, the Monte Carlo simulations reported by Garnica-Garza showed that photon beam spectra with peak energies below 150 keV would result in unacceptably high skin irradiation [72]. As a result, the 100 keV beam was not considered in the models that follow. As mentioned above, beam energy higher than 1.00 MeV resulted in dose enhancement of less than 1% and so was also not considered for the subsequent models. While photon energies higher than 5 MeV were not simulated in this model, it is conceivable that they would result in DEF values higher than 1.00 as discussed earlier. The scope of this work is limited to orthovoltage x-ray beams but future work may consider higher energy levels for comparison as well. Additional consideration is given to potential issues arising from the choice of low-energy photon beams in Chapter 6.

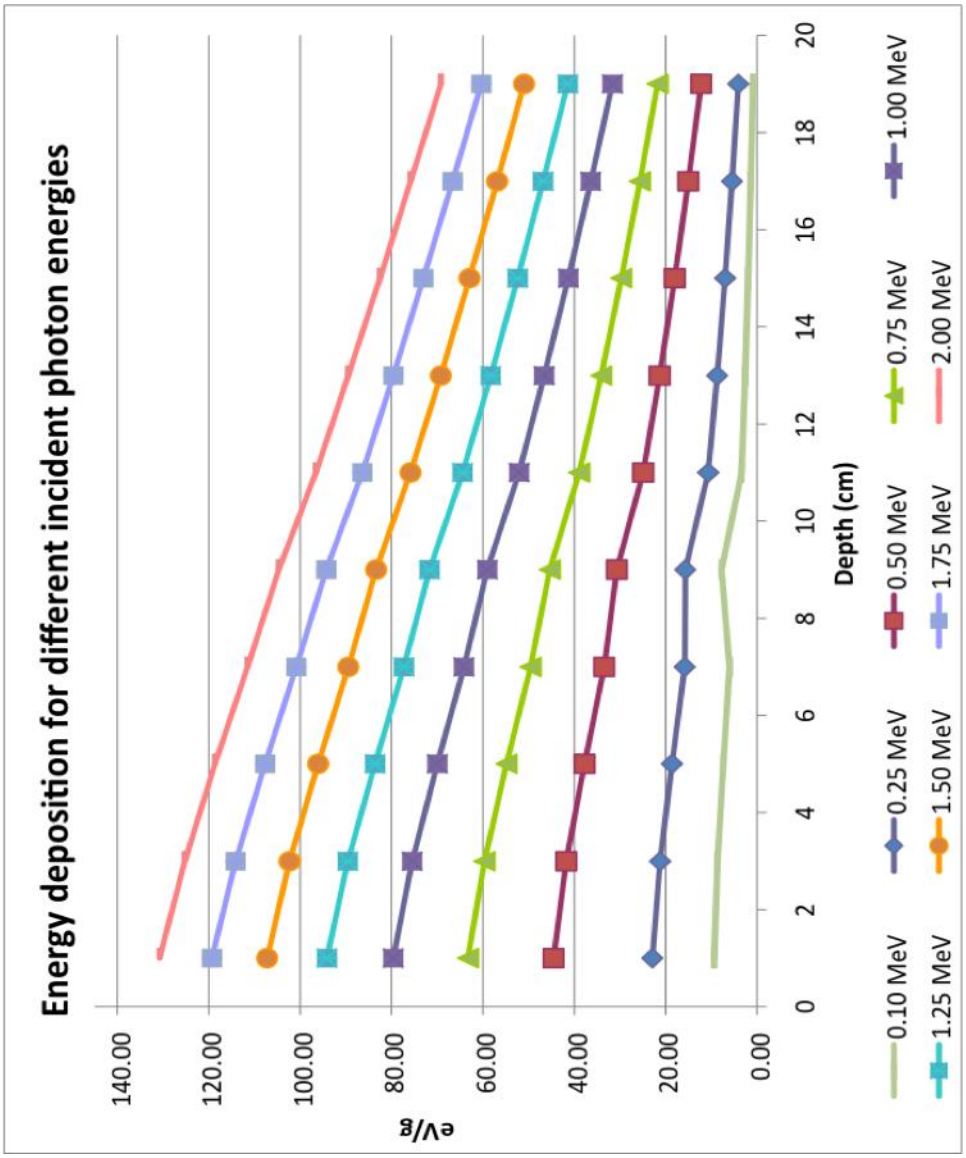

Figure 4-4: Energy deposition profile for different incident photon energies. Beam attenuation described by energy deposited per photon as a function of tissue depth.

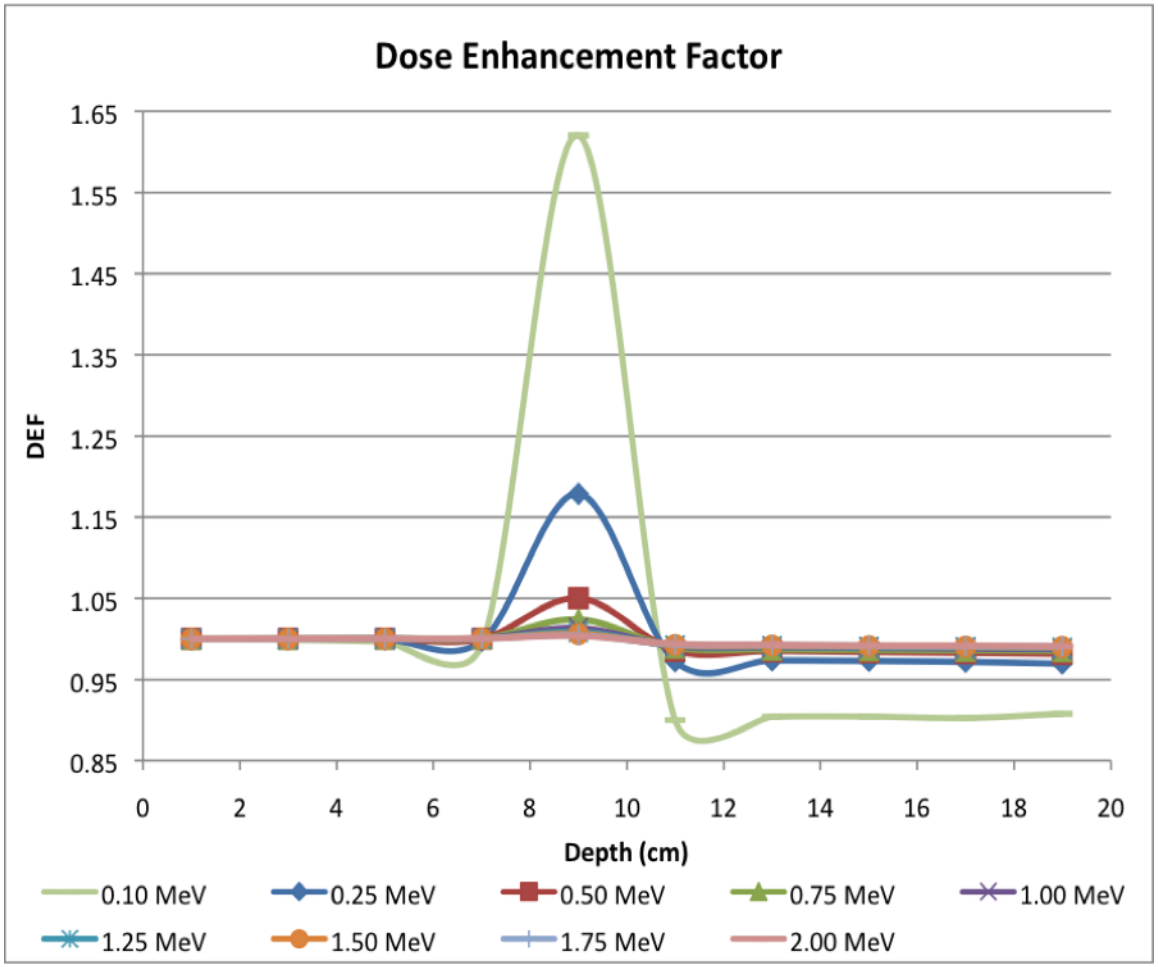

Figure 4-5: Dose Enhancement Factors for different incident photon energies. DEF values plotted as a function of beam energy

4.2 Tumor depth dependence

The second variable tested for possible effects on the DEF was the depth of gold-laden tumor in the tissue sample. As discussed earlier, gamma ray interactions in the body reach a peak energy deposition and then drop off exponentially. As a result, the depth of the target in the tissue sample should have an effect on the relative improvement on the delivered dose. A shallower target area should result in higher incident photon energy and correspondingly result in a lower amount of energy deposition. Conversely, a deeper target area should result in incident photons losing energy in the tissue before encountering the target and correspondingly result in a greater energy deposition in the target area. In order to determine what magnitude of improvement could be expected due to these factors, the depth of a single tumor slab was defined as 5 cm (A), 9 cm (B), or 15 cm (C) away from the irradiated surface of the tissue as shown in Fig. 4-6. Similar to the earlier model, the results of this model were used to describe more precise spatial geometries for subsequent models.

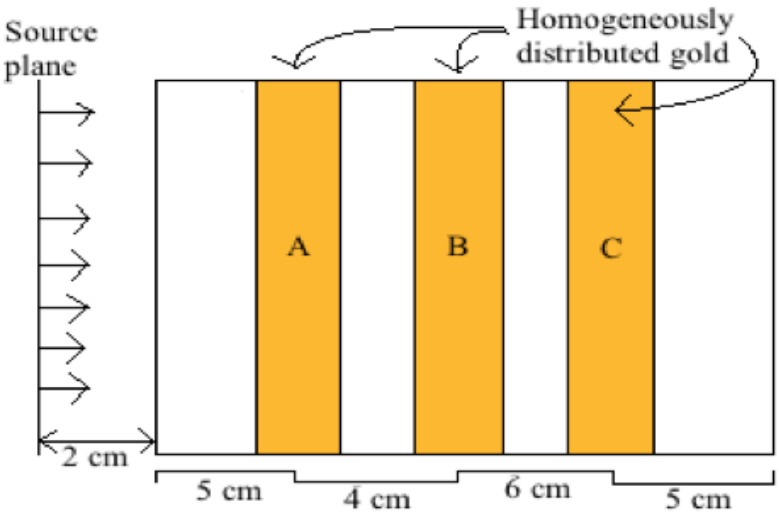

Figure 4-6: Representative geometry for tumor depth dependence

In order to gain sufficient insight into the effects of tumor depth, the gold-tumor slab was placed at the three different depths in the tissue and the flux and energy deposition tallies were recorded. Shown below in Fig. 4-7 a-c, the relative flux profile in

the tissue changed drastically depending on tumor depth. It is important to note that the results shown below are flux measurements relative to the flux with no gold in the tissue slab and not absolute measurements. Also, the data shown in Fig. 4-7e is the same as that in Fig. 4-5 with only those beam energies included that fall within the defined filtering criteria.

Since the gold slab has a much higher attenuation coefficient than the surrounding tissue, it makes sense that the flux should drop off behind the gold. This is clearly evident in each of the depths tested as the relative flux drops below 1.00 in the sections sampled after the gold. It is interesting to note that although each tissue slab experienced the same 1% – 3% reduction in relative flux over the entire tissue depth, the decrease occurs only after the photon beam encounters the gold. As a result, the tissue behind the gold sees the same reduction in flux, but no beam-gold interaction effects are evident in the tissue before the gold. This profile makes sense since the interaction has not yet occurred for those cases, but also means that the benefit of using gold as a radiosensitizer is diminished. The deeper the gold, the larger the volume of tissue that is subject to the unmodified photon flux experienced in the absence of gold.

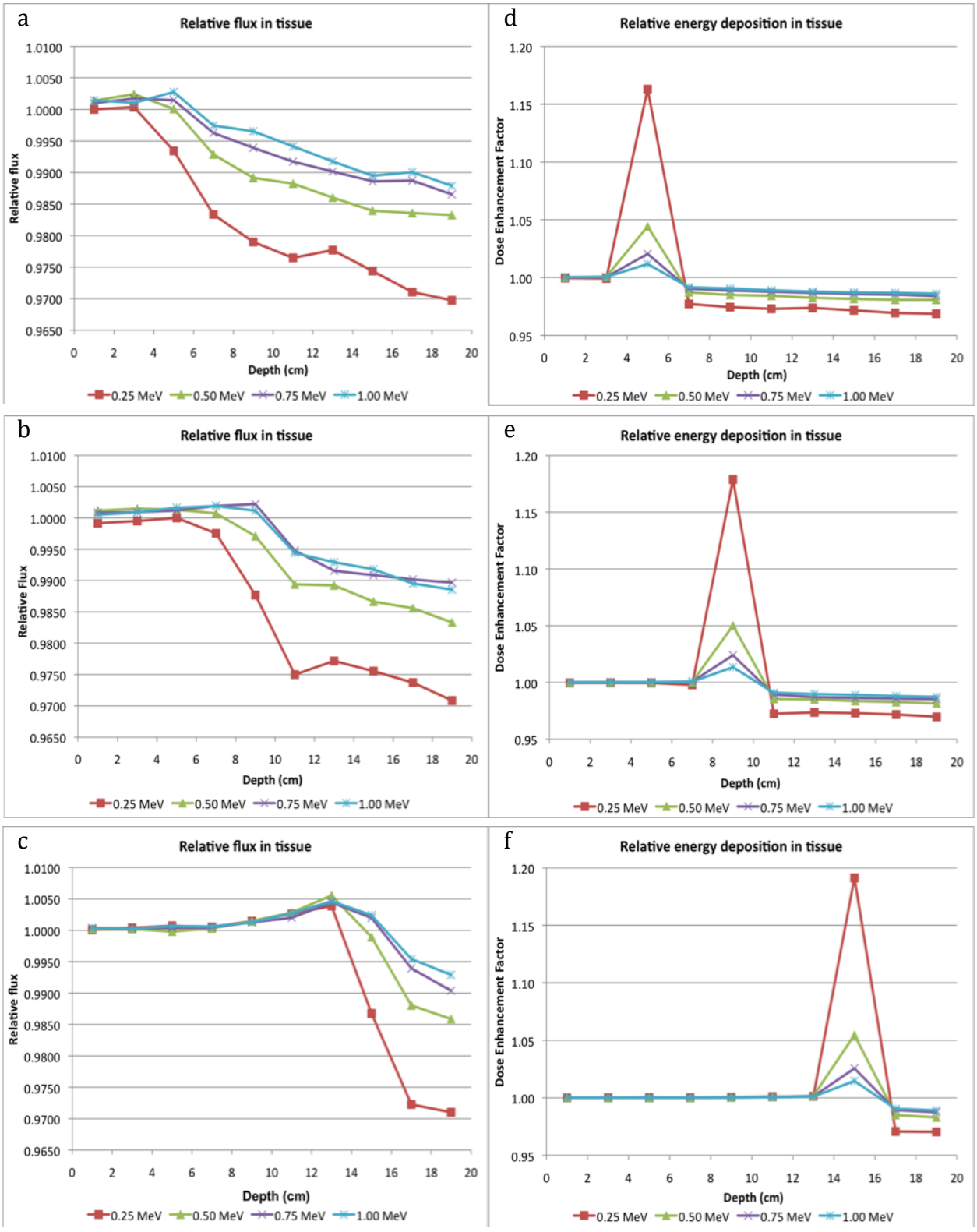

Figure 4-7. a-c: Relative flux and DEF for tumor depth dependence. Flux is plotted as a function of position with gold present at depths of 5 cm (a), 9 cm (b), and 15 cm (c). d-f: DEF is plotted as a function of position with gold present at depths of 5 cm (d), 9 cm (e), and 15 cm (f).

Although the relative flux profiles look very different depending on the depth of the gold in the tissue slab, the distribution shape of the dose enhancement factors calculated for each case look relatively similar as seen in Figs. 4-7 d-f. The obvious difference is due to the difference in gold depth, but the overall trend is the same. A DEF of 1.00 is evident in each 250 keV case until the photon beam encounters the gold after which there is an increase of more than 16% (1.163 for the 5 cm depth, 1.179 for the 9 cm depth, and 1.191 for the 15 cm depth). The increase in the DEF is due to the fact that the beam energy decreases as it travels through the tissue, which correspondingly increases the photoelectric cross section for the beam. The DEF increases for the 1.00 MeV case are significantly less pronounced (1.11, 1.13, and 1.14 respectively) perhaps due to the fact that beam does not lose a significant amount of energy in the tissue slab. The DEF for each energy level decreases between 2-3% after the photon beam interacts with the gold and does not seem dependent on the tissue depth. Again, this highlights the fact that increasing tumor depth results in an increase in the amount of healthy tissue that receives a significant radiation dose.

4.3 *in situ* gold concentration dependence

The third variable that was manipulated for the purposes of these preliminary models was the concentration of gold at the tumor sites. Using the Hainfield studies as a guide, gold concentrations in the tumor were varied from the initial 7 mg/g up to 30 mg/g in the preliminary models. Both the 7 mg/g and 12 mg/g concentrations were described and used in the Hainfield studies that demonstrated the proof-of-concept for dose enhancement. Thus, it was necessary to quantitatively determine the effects of those concentrations as described by these models in order to create a reference, to ensure that these models were relevant. The 30 mg/g concentration level was used to show the level of enhancement possible using this method with the hope that such a high intra-tumoral concentration may be possible in the future. The geometry used for this iteration of the preliminary model is the same as the model which tested photon energy dependence as is illustrated in Fig. 4-8. As mentioned earlier, Chithrani et al. demonstrated markedly

higher cellular uptake of 50 nm AuNP compared to nanospheres of smaller diameters. As a result, the 7 mg/kg gold concentration has been used here as a benchmark value only. The concentrations in the detailed model take cellular uptake enhancement into account.

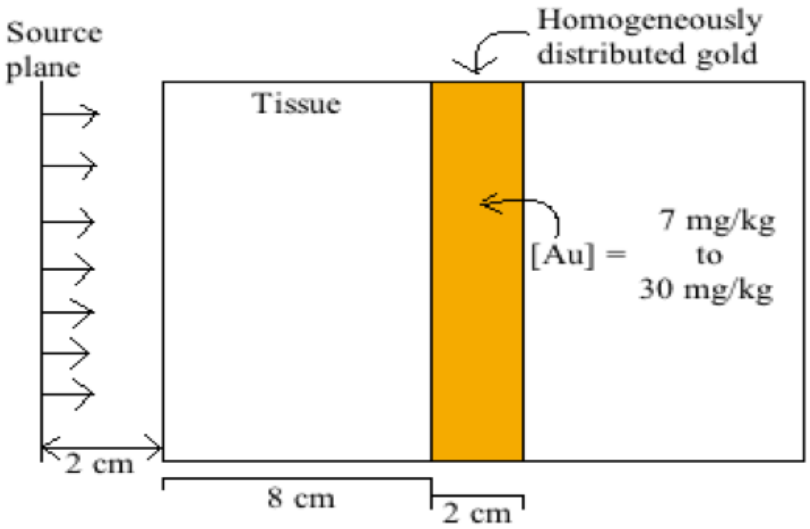

Figure 4-8: Representative geometry for *in situ* gold concentration dependence

The initial limits for this model were taken from the Hainfeld study that observed diagnostically significant improvement with a tumor-gold concentration of 7 mg/g. A maximal limit of 30 mg/g was used to highlight the substantial improvement in tissue response to radiation when the gold concentration was increased four-fold. While this upper limit may not be pharmaceutically feasible at the moment, it is conceivable that a delivery system may be developed that would be capable of delivering elevated levels of gold to tumor sites. Also, while these gold concentrations are the same as those commonly associated with the Hainfeld study, they are used here simply to illustrate the effects of tumor-gold concentrations on radiation dose enhancement. The detailed model takes into account the improvements in cellular uptake for larger nanoparticles and the tumor-gold concentration is adjusted accordingly.

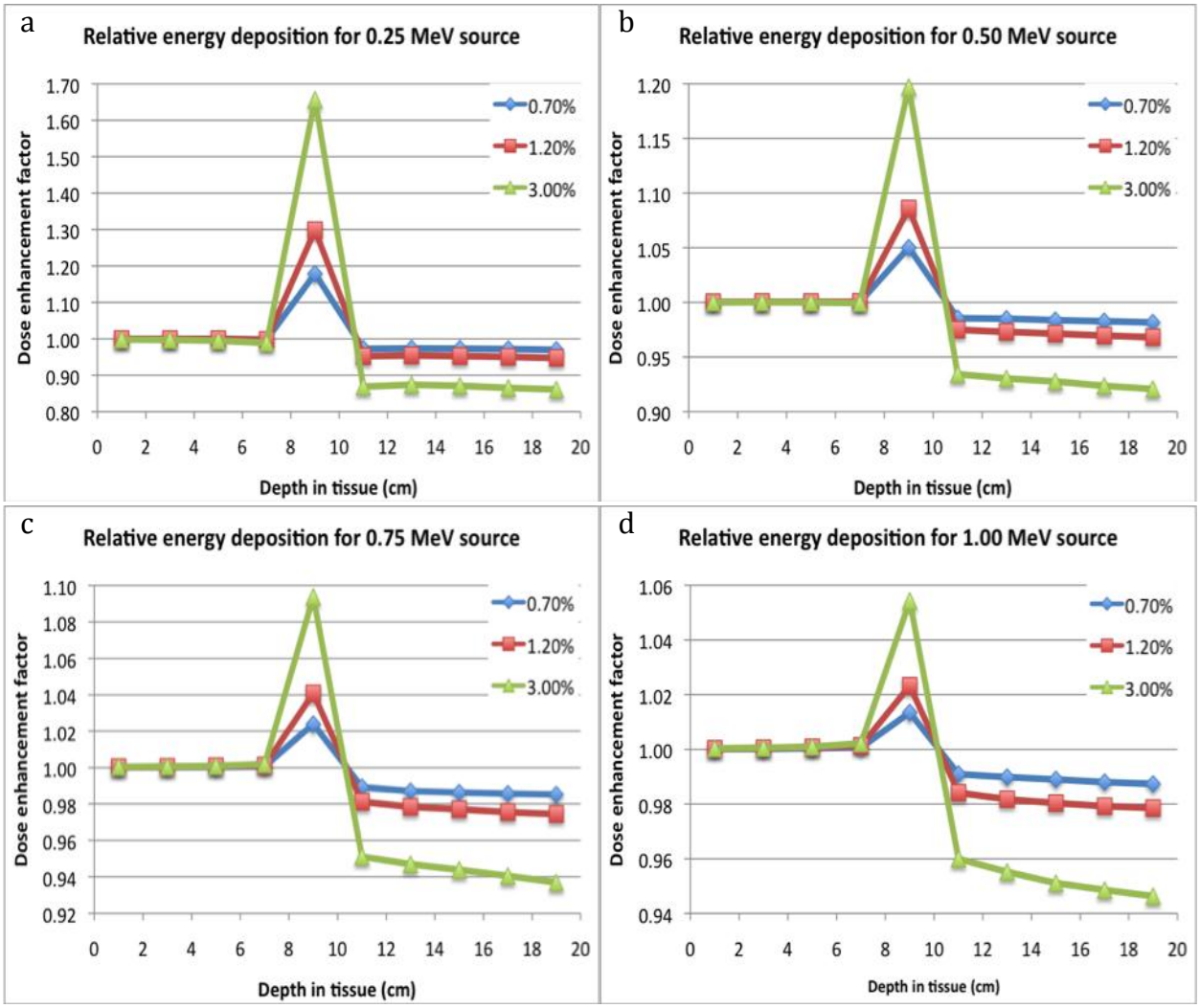

Figure 4-9: DEF for *in situ* gold concentration dependence. Graphs shown compare concentrations of 7 mg/kg, 12 mg/kg and 30 mg/kg for a photon source energy of 0.25 MeV (a), 0.50 MeV (b), 0.75 (c), and 1.00 MeV (d).

The results from this model serve simply to describe the relative effects of *in situ* gold concentrations. As seen in Figs. 4-9 a-d, increasing the concentration of gold four-fold from 0.7% (7 mg/g) to 3.0% (30 mg/g) increases the DEF by approximately the same factor of four regardless of the source beam energy. The considerable improvement is most evident with 250 keV photons where the DEF increases from 1.18 to 1.66 with a corresponding concentration increase. However, the same relative increase can be seen with 1.00 MeV photons where a 1.01 to 1.05 for the same increase in concentration.

The purpose of this model was to establish a quantitative baseline to which the results of the following model could be compared. Using established *in vivo* parameters, a determination can me made regarding the relative importance of varying different details of the model. These observations gleaned from iterations of the preliminary MC model are used to develop the more detailed model that follows. Improvements in spatial geometry, mass-photon interaction considerations, and nanoparticle distribution are all taken into account.

Chapter 5

Detailed model for gold-mediated effective dose enhancement

As mentioned earlier, the results of the preliminary model were used to define more precise geometrical models to be used in a subsequent simulation. The results of the photon energy dependence simulations confirmed an earlier hypothesis that gold would be an effective contrast agent when incident photon energy was in the range over which the total attenuation coefficients of tissue and gold differed significantly. Fig. 1-6 is reprinted here as Fig. 5-1 for ease of reference. As shown below, the difference in attenuation factors is evident in the 5keV – 1 MeV range, which lends credence to the decision to restrict incident photon energy to less than 1 MeV. Additionally, the attenuation coefficients begin to diverge at higher photon energies as well, which lends insight into the results obtained by Robar et al. as discussed earlier [73]. However, the scope of this work is restricted to the sub–1MeV photon beams due to the reasons discussed earlier in Chapter 4.

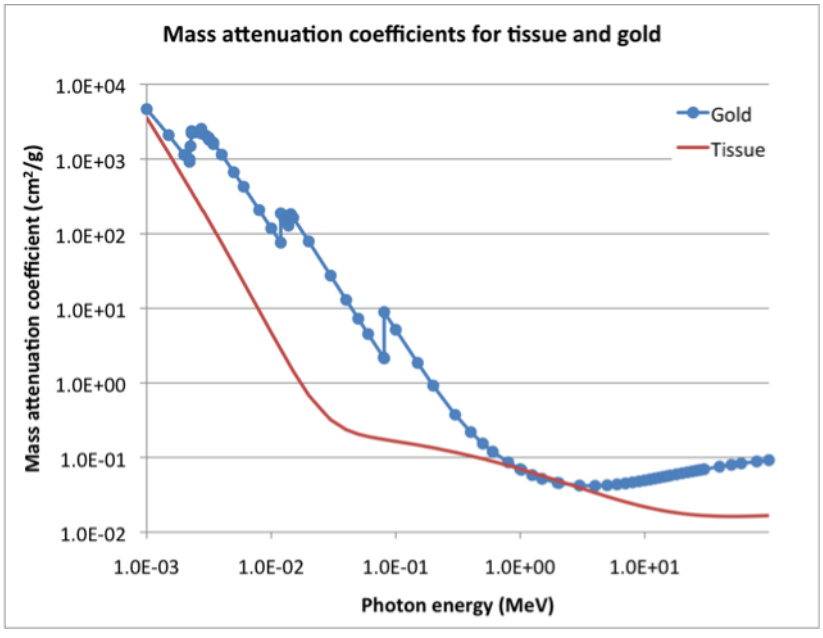

Figure 5-1: Attenuation coefficients for gold and tissue

Similar to the preliminary model, three different cases of the detailed model were simulated with the details of each model varying according to one of the conditions described below. Since the effects of gold on photon flux have been illustrated by the results of the preliminary model, the results given here focus only on the energy deposited in the different volumes. The corresponding dose enhancement factors are calculated as described by Equation 3-5 with the results of each run compared to the results with no gold present. In addition, the results of ideal cases are also presented for comparison as described in each of the cases that follow.

5.1 Updated *in situ* gold concentration

As previously mentioned, Chithrani et al. demonstrated that 50 nm nanoparticles have significantly improved cellular uptake compared to the 1.9 nm diameter nanospheres used in the Hainfeld study [79]. The Chithrani study reported total gold mass internalized by the cells that ranged from $5\times10^{-12}g$ to $9\times10^{-12}g$. By comparing the internalized gold mass to the $300\times10^{-12}g$ average mass of a HeLa cell as reported by Popescu et al., *in situ* concentrations of 1.53% to 2.77% were calculated [85]. A maximal gold concentration of 4.00% was also calculated by assuming that the maximum amount of internalized gold nanoparticles $\left(9\times10^{-12}g\right)$ occurs in the smallest cells $\left(225\times10^{-12}g\right)$. While such elevated concentrations may prove problematic in healthy cells, it is useful to note that the passively targeted AuNP only accumulate at tumor sites via the EPR pathway – the prolonged circulation times would ordinarily result in clearance through the renal system in the absence of the leaky vessels around a tumor site. Since gold uptake is dependent on nanoparticle interactions with the cell membrane, this concentration is unlikely to occur in normal physiological settings using currently available pharmaceutical techniques, but is taken here to represent the maximum concentration of gold that could conceivably be achieved in future clinical settings. The updated model is represented in Fig. 5-2.

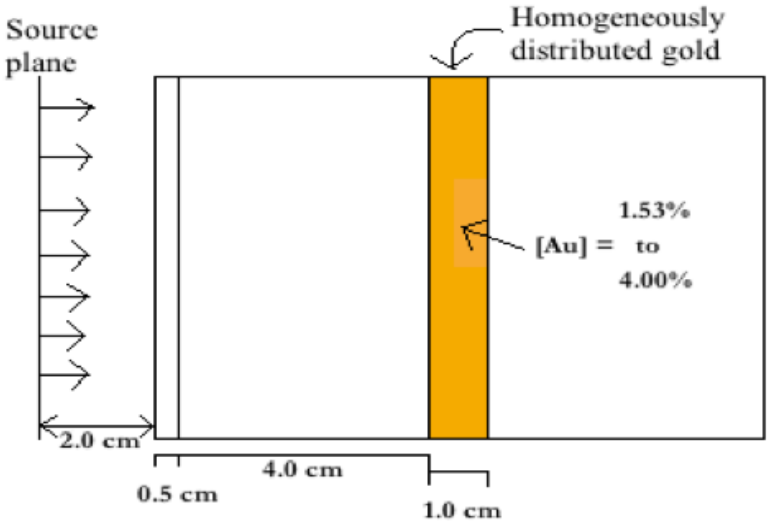

Figure 5-2: Updated gold concentration and dimensions for detailed model

As can be expected, the results of the updated gold concentration model in Fig. 5-3 illustrate the benefit of using the maximum possible gold at the tumor site. Additionally, the lower photon energies display significantly greater propensity for dose enhancement due to the incidence of photoelectric interactions. The physiologically achievable concentration of 2.77% resulted in a dose enhancement factor of 1.54 compared to 1.19 calculated using the 1.2% concentration reported by Hainfeld. The gradual decrease in DEF values within the tumor volume may be due to the inherent shielding that occurs due to the gold particles distributed in the tumor volume as discussed in Chapter 4. Since the gold is modeled as a homogenous mixture, the density of the tumor is significantly higher than the surrounding tissue, which may also contribute to this shielding effect. The conclusions drawn from the results of the preliminary model all apply to this iteration of the detailed model as well, with the notable exception being the improvement in dose enhancement even at higher photon energies and lower gold concentrations. Additionally, the upper limit for dose enhancement is raised to 76% with a gold concentration of 4.00% corresponding to 40 mg of gold per gram of tumor tissue.

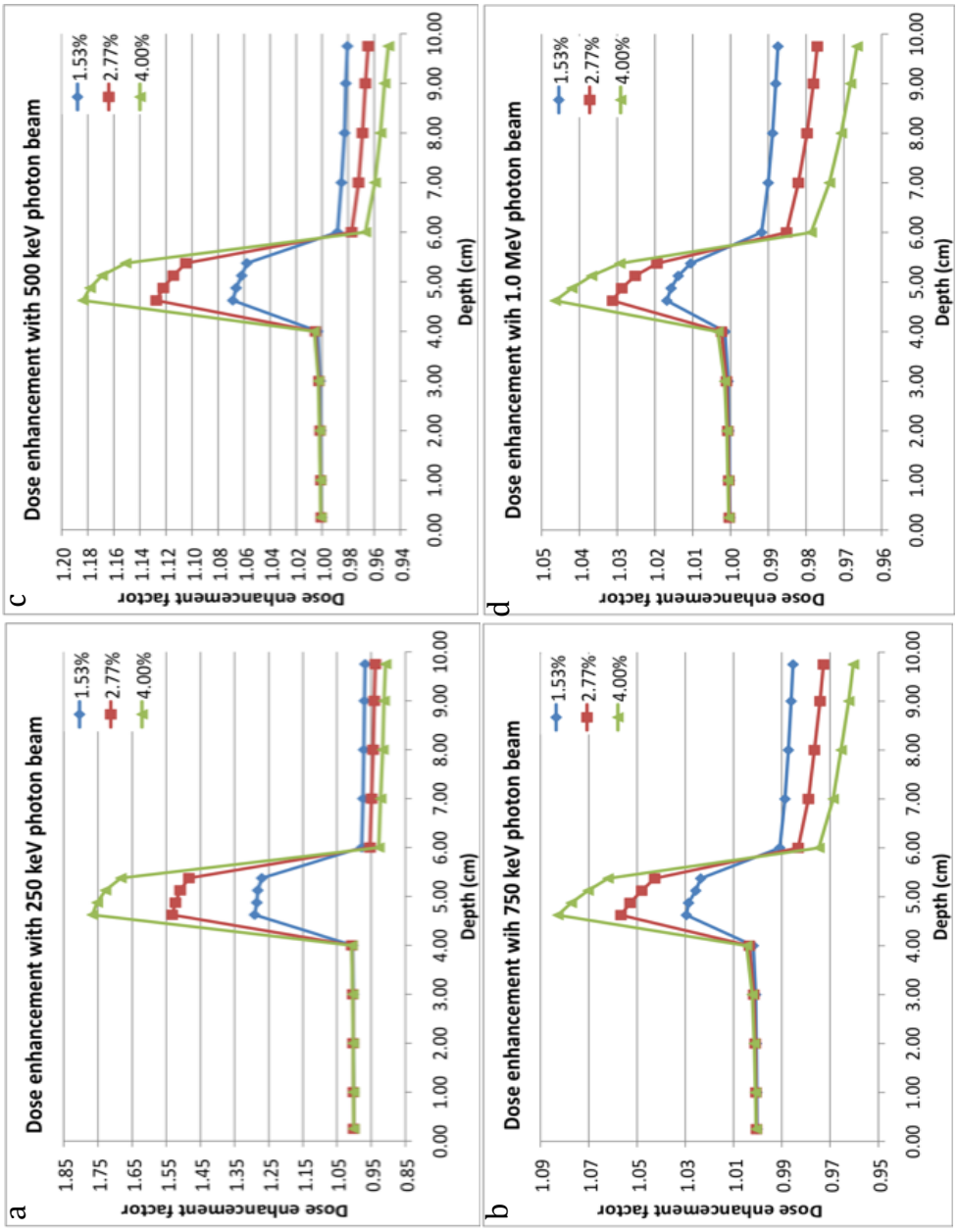

Figure 5-3: DEF profiles for updated gold concentration dependence. DEF values plotted as a function of tissue depth for photon energies of (a) 250 keV, (b) 500 keV, (c) 750 keV, and (d) 1.00 MeV are included for comparison.

5.2 Lack of nanoparticle specificity

Despite the convenience of EPR effects present at tumor sites, passive nanoparticle targeting is not perfect. The use of monoclonal antibodies and other tumor-specific markers can be used to improve the specificity with which the nanoparticles target the preferred site, but these techniques have not been used in radio-sensitivity studies this far. As a result, a certain degree of diffusivity must be accounted for when modeling the distribution of gold around a tumor site. The study by Hainfeld et al. described passive tumor targeting and diffusion was observed when the excised murine tissue was analyzed for gold content [76]. Tumor to tissue concentration rations ranging from 8.5:1 to 3.5:1 were observed in the mice treated with 1.9 nm nanoparticles. Since this work is assuming a particle diameter of 50 nm due to improved cellular uptake characteristics, it is possible that the diffusion ratio may approach the lower end of the range observed by Hainfeld.

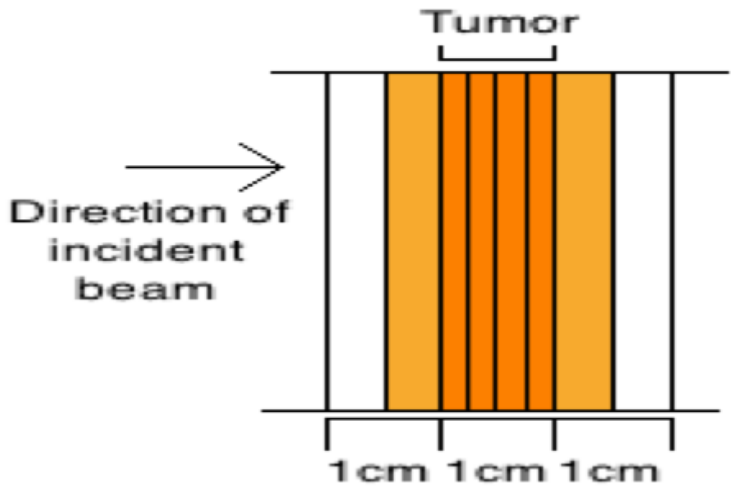

Figure 5-4: Representative geometry for gold specificity dependence. Passive diffusion results in lower concentration proximal to tumor

In order to model the effects on effective dose enhancement due to possible nanoparticle diffusion, a concentration of gold was distributed in the tissue immediately outside the simulated tumor. The tissue cells, immediately outside the tumor, were split in half with the diffusing nanoparticles in the half closer to tumor. All other geometric

details were left unchanged from the previous simulation. Fig. 5-4 illustrates the geometric distribution of the gold-bearing volumes; the overall geometry is assumed to be the same as that described in Fig. 3-2.

In order to get a lower bound on enhancement (the worst case scenario), the lowest *in situ* gold concentration of 1.53% was defined in the tumor region and a tumor to tissue ratio of 3.5:1 was used to yield a concentration of 0.44% in the immediately adjacent tissue. This was contrasted with a tumor to tissue ratio of 8.5:1 yielding a 0.18% gold concentration in the surrounding tissue. Both results then compared against the ideal tumor-targeting scenario with no diffusion of the gold into the surrounding healthy tissue. The results below show the effects of no diffusion, a diffusion ratio of 8.5:1, and a diffusion ratio of 3.5:1 with beam energies ranging from 250 keV to 1.00 MeV. Dose enhancement factors are plotted as a function of tumor depth in Fig. 5-5, and the results are focused on the tissue volumes immediately surrounding the tumor. As a result, DEF values are only given at depths ranging from 3.00 cm to 7.00 cm as the values for tissue depths outside that range are unchanged from the previous simulation.

As can be expected, the DEF profiles for each set of results is less discrete around the tumor site due to the presence of gold outside the tumor volume. While the maximum values for DEF are unchanged for all photon energies, the decrease in effective dose after the photon beam passes through the tumor volume is of interest. Since it is unlikely that gold nanoparticles would be distributed homogenously outside the tumor, it may be possible to shape the external beam geometry to reduce effective dose around the tumor. If the beam is shaped in such a way that the excess gold outside the tumor is targeted before the tumor volume, rather than after, the photons arriving at the tumor site with have lost a portion of their energy before entering the tumor volume. As a result, the gold-laden tumor will have a higher sensitivity to the photon beam due to the energy-dependence discussed above. This explanation may account for the sharper decrease in DEF values for both cases where gold is present outside the tumor volume as seen at the 6.00 cm to 7.00 cm depth in Figs. 5-5 (b), (c), and (d) below.

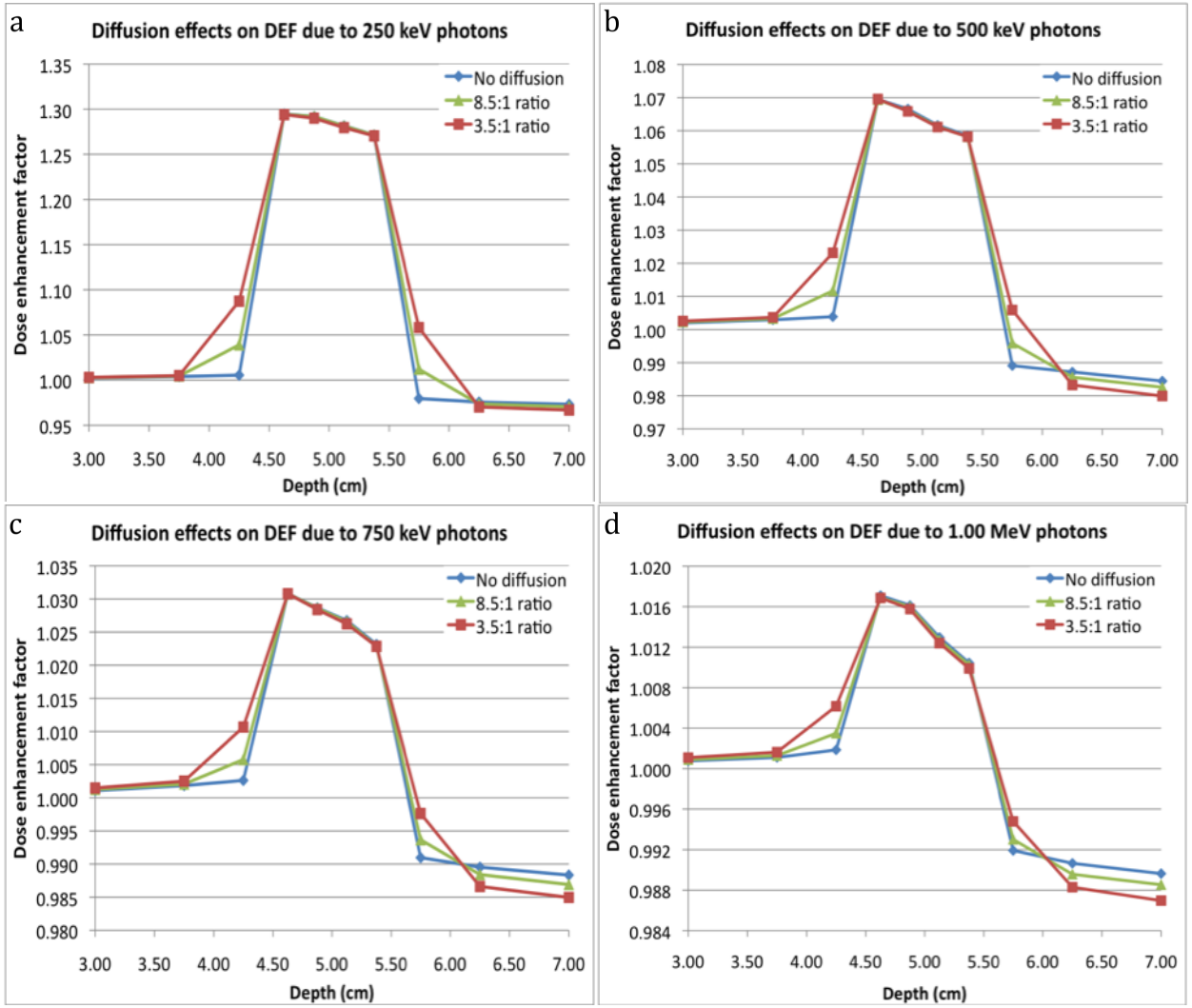

Figure 5-5: DEF profiles for gold specificity dependence. The effects of passive nanoparticle diffusion on DEF values plotted as a function of tumor depth for (a) 250 keV, (b) 500 keV, (c) 750 keV, and (d) 1.00 MeV

5.3 Non-homogeneous gold distribution

Each of the *in vivo* studies reviewed discussed the possibility that treating the gold nanoparticles as a homogenous tissue-gold mixture would result in a misrepresentation of the dose enhancement calculated in Monte Carlo simulations. As a result, a non-homogenous gold distribution was defined in the tumor slab based on the assumption that the gold nanoparticles would not be able to penetrate into the center of the tumor. The ensuing aggregation at the periphery of the tumor is defined as having the same updated gold concentration as the previous model described above. However, since EPR effects may not extend to the center of a tumor, the amount of gold at the center is reduced to a lower concentration at the edges of the tumor. This non-homogeneity is illustrated in Fig. 5-6 and the overall geometry is again assumed to be the same as described in Fig. 3-2.

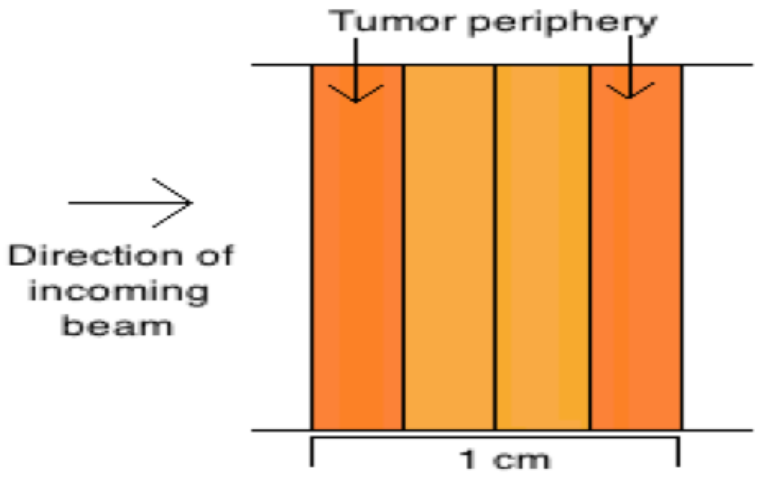

Figure 5-6: Representative geometry for homogeneity dependence. Lower concentration at center of tumor due to lack of Au penetration.

As mentioned, several studies discussed the potential issues with assuming homogeneously distributed gold nanoparticles throughout a tumor volume. In order to gain some insight into the effects of non-homogeneity, several simulations were performed under the assumption that gold nanoparticles may not fully penetrate a tumor volume. The gold concentrations from the Chithrani study were used to generate a baseline DEF curve with the assumption that the tumor gold distribution was

homogenous. Since *in vivo* tumor penetration studies have not been done to the author's knowledge, the reduction factors for the center of the tumor were taken from work described by Hainfeld et al. where passive nanoparticle diffusion was observed [76]. Although this iteration of the model does not account for diffusion into healthy cells, similar physical interactions are assumed to allow gold to reach the center of the targeted tumor. As with the specificity-dependence model described above, ratios of 8.5:1 and 3.5:1 were used to ascribe the gold concentration levels to the different tumor regions. Results are compared against the ideal scenario with homogeneously distributed gold throughout the tumor region.

It is argued above that the larger diameter nanoparticles used in this work may result in passive diffusion into untargeted healthy cells. Although the mechanism of transport for passive diffusion outside the tumor and nanoparticle penetration into the tumor will differ, the assumption is that the enhanced influx of 50 nm nanoparticles extends beyond the tumor periphery. However, in the absence of *in vivo* studies for corroboration, the results of this simulation may only provide a rough approximation of the quantitative effects of gold nanoparticles accumulating in the tumor periphery without penetrating to the core of the tumor volume.

Given below is a set of results obtained by assuming periphery to core ratios of 3.5:1 and 8.5:1 with four different photon energies and at 1.53% baseline gold concentration. Additionally, results from simulations using 250 keV and 1.00 MeV photons along with a 2.77% baseline gold concentration are included to demonstrate the similarity in DEF profiles, as only the amplitude is different. These plots are followed by a series of results obtained by combining different nanoparticle penetration ratios and passive nanoparticle diffusion outside the tumor volume.

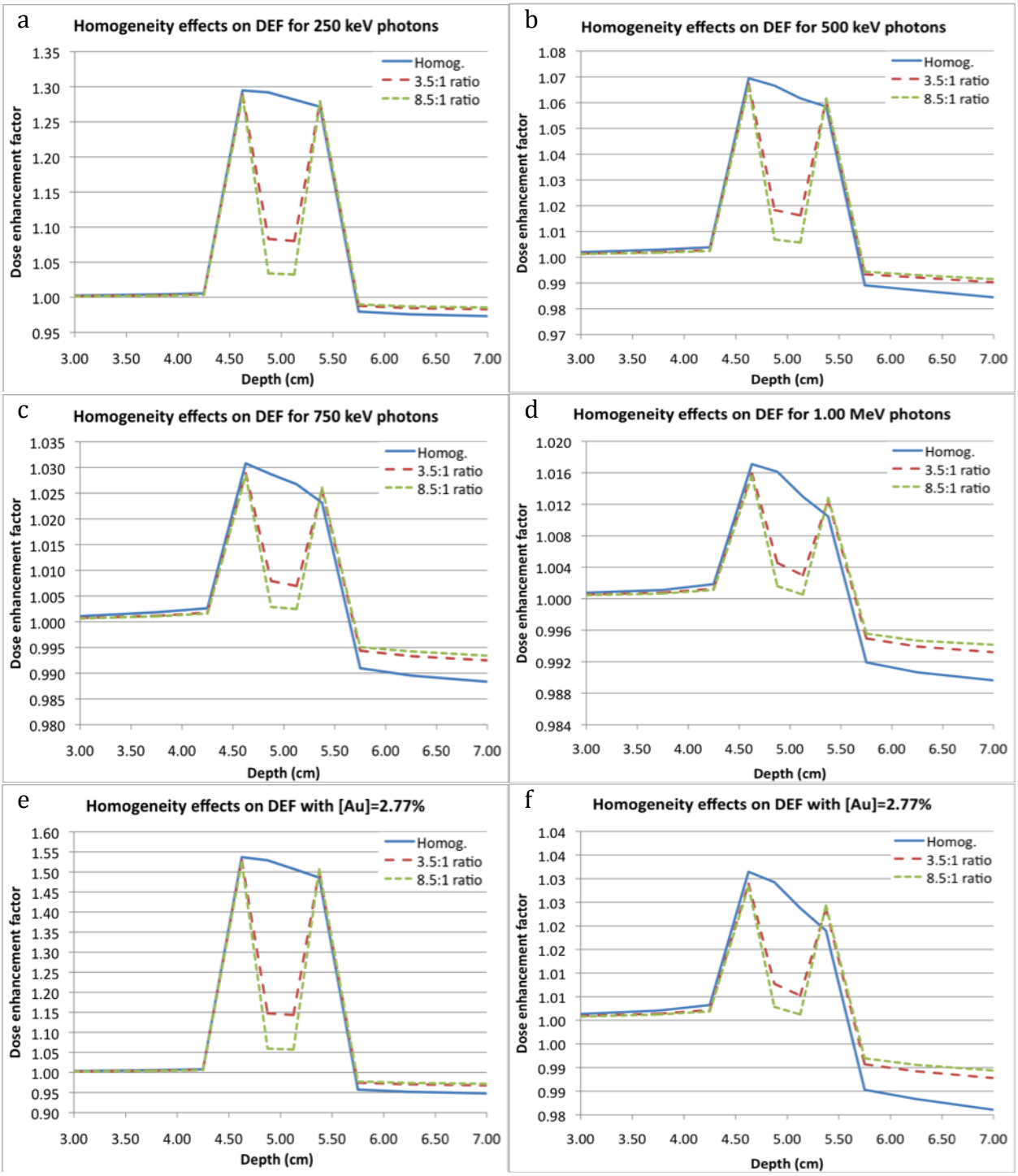

Figure 5-7: DEF profiles for homogeneity dependence. Variations within a tumor volume are shown for (a) 250 keV, (b) 500 keV, (c) 750 keV, and (d) 1.00 MeV photons. Baseline [Au] is defined as 1.53% by mass. Also included: DEF variations using baseline [Au] of 2.77% for (e) 250 keV and (f) 1.00 MeV photons.

The results plotted in Fig. 5-7 illustrate the effects of having a lower concentration of gold at the center of the tumor compared to the tumor periphery. As expected, the effective dose enhancement due to the presence of gold is reduced in the areas with lower gold concentrations. Additionally, the lack of gold results in the photon beam retaining more energy as it passes through the tumor due to the lack of high-Z material. This results in a second peak in the DEF curve when the beam interacts with the distant tumor boundary. This also accounts for the fact that the 1.00 MeV photon beam deposits more energy at the distant tumor boundary in the case with non-homogeneous gold distribution. However, averaged over the whole tumor volume, the dose enhancement is reduced as expected for the non-homogeneous case. The results of running the simulation with a baseline gold concentration of 2.77% are also included for photon energies of 250 keV and 1.00 MeV. Comparing these results to those for the lower gold concentration, it is easy to see that the DEF profiles are identical in variation. The difference arises in the amplitude of the curves as the higher gold concentration naturally results in a higher overall level of dose enhancement. Consequently, the results of the [Au]=1.53% simulation may be extended for any physiologically realistic gold concentration with similar DEF variations.

A worst-case scenario was also simulated where no gold nanoparticles penetrate to the center of the tumor volume. In this case, a 250 keV photon beam was incident on a tissue phantom with the same geometrical parameters as the previous study testing homogeneity dependence. In addition to the lack of gold transport to the tumor core, it was also assumed that non-specific uptake of the gold nanoparticles into the healthy tissue surrounding the tumor volume would occur. This case, as described, may represent a tumor atypically resistant to particle transport combined with a poorly designed tumor-targeting scheme. The results for this case are given in Fig. 5-8.

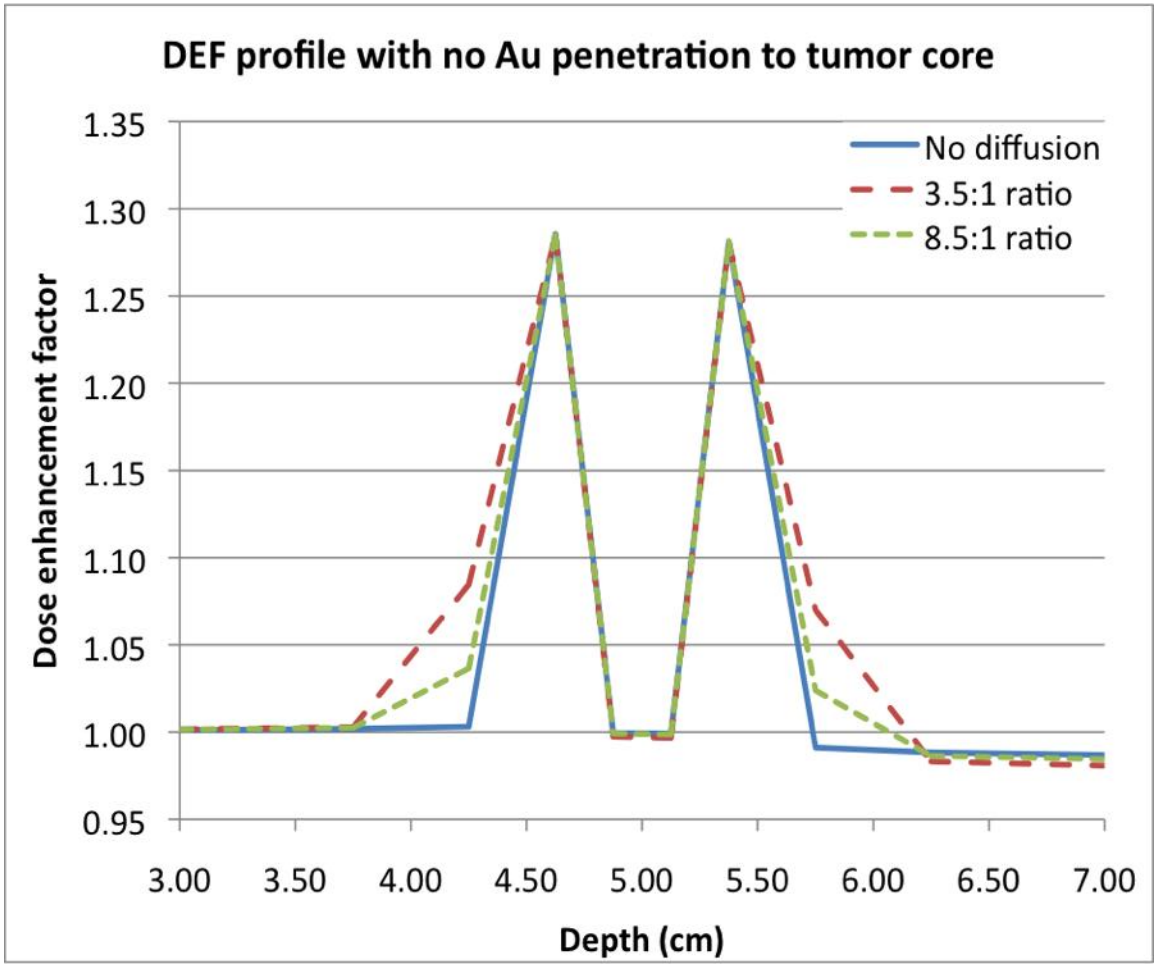

Figure 5-8: Combined effects of homogeneity and specificity dependences. DEF profiles are shown with the effects of non-specific AuNP diffusion and lack of tumor penetration.

Significant dose enhancement was observed in the gold-bearing volumes with DEF values approaching 1.30 for both tumor periphery cells. However, the results suggest that no additional dose would be deposited at the tumor core. Contrasted to the DEF values of unity at the tumor core, the passive diffusion modeled outside the tumor resulted in excess doses of 4% and 9% for the diffusion ratios tested (tumor to tissue ratios of 8.5:1 and 3.5:1 respectively). While more detailed models are needed, both at the macroscopic and microscopic levels, before any conclusive statements can be made, it is clear that tumor penetration may be a significant obstacle that must be overcome for successful and effective radiation treatments.

Given these results, it is important to note that none of the simulations take into account active targeting strategies, and that all gold is assumed to accumulate and diffuse through passive transport. The maximum limit on gold concentrations in tumor cells used in these simulations is based on published in vivo studies using unmodified gold nanoparticles. The specific concentration of intracellular gold possible using monoclonal antibody tagging has not been well established. Needless to say, implementing specific targeting strategies that incorporate the cell surface markers unique to tumor cells should result in improved effective dose enhancement.

Chapter 6
Analysis and Conclusions

Presented here is what aims to be a detailed look at the possibilities and benefits of using gold in teletherapy radiation treatment models. The results from various Monte Carlo simulations are discussed with special attention given to the radio-sensitivity dependence on photon energy, gold nanoparticle concentration, tumor depth, targeting specificity, and nanoparticle penetration. The result of the preliminary model are presented to quantitatively corroborate published *in vivo* and *in vitro* studies and expand the amount of analytical data available to direct future work. Additionally, the results of the detailed model attempt to predict some of the limitations and restrictions inherent in the application of unmodified gold nanoparticles for radio-sensitivity. The hope is that the effect of the relevant physical mechanisms described here may guide the development of enhanced targeting mechanisms and inspire future work.

6.1 Discussion of results

Based on the results obtained from the preliminary model, it is clear that the physiological response observed in Hainfeld studies was due to the effective dose enhancement observed at the tumor sites. The original study used 68 keV and 157 keV photon beams and reported that the lower energy photons showed improved tumor eliminating efficacy. While the work here did not address those specific energy levels, the energy-dependent preliminary model was designed to develop an understanding of the overall energy-dependence of effective dose enhancement. Using the 7 mg/kg gold concentration reported by Hainfeld, DEF values of over 1.60 were observed when using a 100 keV photon beam. The effective dose enhancement dropped to 1.18 using a 250 keV photon beam and 1.05 when photon energy was increased to 500 keV. The DEF values monotonically decreased as photon energy was increased and a minimum DEF of 1.003 was obtained using a 2.00 MeV photon beam. Given these results, it is easy to see that

decreasing the photon beam energy improves the effective dose enhancement at the tumor site.

Analyzing the results of the first simulation leads to the idea that the lowest possible energy should be used for tumor targeting. However, one of the primary concerns when reducing photon energy is the reduction in the penetrating ability of the photon beam. Although the lower energy photons have a higher interaction cross-section for the gold-laden tumor, the interaction cross sections of healthy tissue are not exempt from a similar increase. This property is illustrated in the depth-dependence preliminary model. The goal of this simulation was to determine whether reducing the photon beam energy would result in a reduction in energy deposition due to premature attenuation of the photon beam. The results showed that DEF had a relative lack of dependence on the depth of the tumor and doubling the tumor depth only changed the effective dose enhancement by a maximum of 3%. These results were also observed in the 100 keV photon case as shown in Fig. 6-1, which would lead to the conclusion that the low energy photons should be the ideal candidate for this work. However, the energy deposited per photon in the 100 keV case is less than 10 eV per gram of tumor tissue and the intensity of the photon beam required to deliver a lethal dose of radiation to the tumor volume would result in unacceptably large doses to surface tissues. This result agrees with the Garnica-Garza study discussed earlier, and as a result, the 100 keV photons were not included in further simulations [72].

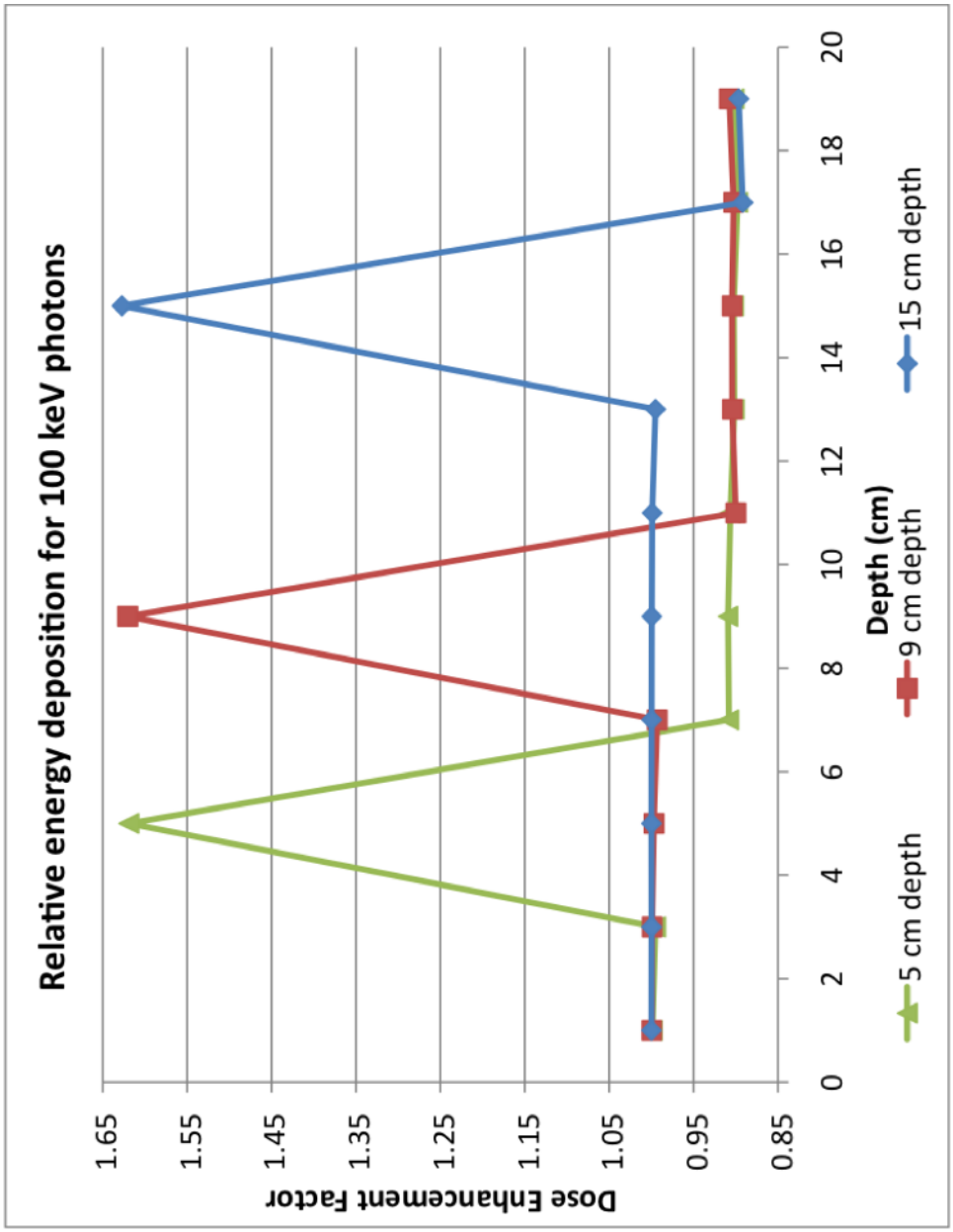

Figure 6-1: DEF profiles for 100 keV photons. Varying the depth of the tumor in the tissue slab does not change the effective dose enhancement seen when using 100 keV photons.

Finally, the last preliminary model was designed to test the effects of the *in situ* gold concentration on effective dose enhancement. The results here were largely as expected as the amount of gold at a tumor site should effectively increase the density of the target volume. In addition, an increase in the number of electrons in the target volume as a result of the increased gold concentration should improve the photoelectric cross section of the tumor. These improvements can be clearly seen as increasing the gold concentration from 7 mg/kg to 30 mg/kg led to a more than three-fold increase in the effective dose enhancement. The DEF increased from 1.18, when a 250 keV photon beam was used to irradiate a 7 mg/kg concentration of gold, to 1.66 when the same photon beam was used to irradiate the 30 mg/kg gold concentration. These results clearly indicate that radiation sensitivity is directly proportional to the amount of gold that can be accumulated at the tumor site.

The first detailed model expanded on the results of the concentration-dependent preliminary model by incorporating the results of the Chithrani study using larger diameter gold nanoparticles. Increasing the particle diameter from 1.9 nm to 50 nm resulted in increased *in situ* gold concentrations with the upper bound of the average gold concentration (27.7 mg/kg) approaching the 30 mg/kg concentration previously thought to be clinically infeasible. The maximum potentially achievable concentration was subsequently calculated to be 40 mg/kg using the larger nanoparticles. Using the higher gold concentrations yielded improved effective dose enhancements, which were significantly larger that those previously observed in the preliminary model. Using a 250 keV photon beam, the improved gold concentration yielded a DEF of 1.26 using the 15.3 mg/kg gold concentration (lower bound), and a DEF of 1.76 for the 40.0 mg/kg gold concentration (maximum concentration). In clinical terms, a DEF of 2.0 would imply that the presence of gold would effectively half the intensity of the photon beam required to treat a tumor when compared to the same treatment in the absence of gold. The results of the updated concentration model, therefore, suggest that maximizing the tumor gold concentration will significantly improve tumor treatment.

The next two simulations were conducted to determine the effect of localized non-homogeneities and inconsistencies in an attempt to approximate clinical realism. In an ideal scenario, the gold prescribed to a tumor patient would accumulate locally and exclusively at the tumor site. This would then result in sharp peaks in the effective dose enhancement profiles as seen in the previous simulations described here. However, realistically modeling of gold nanoparticle distribution in the body must account for passive uptake into the healthy cells surrounding the tumor tissue since the nanoparticles are not specifically targeted. As previously discussed, this non-specificity may be minimized or avoided completely if successful tagging using monoclonal antibodies can be achieved. The *in vivo* and *in vitro* studies reviewed, however, do not discuss the use of such active targeting strategies and consequently, retain the issues associated with non-specific targeting. As such, in order to retain the ability to corroborate the data obtained from the simulations presented here, a more realistic distribution of gold was modeled in and around the tumor site using passive nanoparticle transport mechanisms.

As mentioned, one of the issues that arise with non-specific targeting is passive uptake in the healthy cells around the tumor site. In order to model this, a concentration gradient was established across the boundary of the tumor volume. A tumor cell to healthy cell concentration ratio was defined based on the data reported by the Hainfeld study concerning gold concentrations. The results of two such ratios (3.5:1 and 8.5:1) were compared to the ideal targeting scenario to determine the relative effects of passive targeting. As expected, the effective dose in the gold-laden healthy tissue was about one-third and one-eighth the effective dose in the gold-laden tumor volume respectively. In addition, the DEF values for photon interactions in the healthy tissue after the tumor volume were lower when gold was present outside the tumor boundary. This may be attributable to the fact that the photons had lost a considerable portion of their energy in the broader gold-laden region. If accurate imaging can be performed on the tumor volume to determine the real-time distribution of the gold nanoparticles, this asymmetry in the effective dose deposition may be utilized to minimize dose to healthy cells.

Another issue that arises when quantifying nanoparticle distribution is the fact that a mechanism for tumor volume penetration has not been identified. As a result, even if active targeting strategies are used to ensure accumulation of gold at the tumor site, there is no mechanism currently discussed in the literature that would ensure a homogeneous distribution of gold in the tumor volume. In order to take this problem into account, the distribution-dependent simulation was run with the assumption that some non-ideal tumor penetration may take place. Since no specific values have been reported for *in vivo* studies, a conservative estimate was made using the same diffusion ratios used for the non-specificity simulation discussed above. In addition, a worst-case scenario was also modeled to describe the effective dose enhancement profile for the case where no gold is able to penetrate the tumor volume.

The results of this simulation were largely as expected. The lack of gold at the center of the tumor volume resulted in a bi-peaked effective dose enhancement profile. The DEF values for the tumor core were similar to those observed for the healthy tissue boundary in the diffusion-dependent case. In the ideal tumor penetration case, effective dose enhancement decreases with increasing tumor depth. In the case with no gold in the tumor core, the amplitude of second peak in the DEF profile was larger than the amplitude of the monotonically decreasing profile in the ideal case. This may be due to the fact that the homogeneous gold distribution may induce more scattering events and allow fewer photons to penetrate the tumor volume. The non-homogeneous gold distribution may not induce as many scattering events so a larger number of photons may reach greater depths in the tumor.

6.2 Relevance to other clinical applications

Since no treatment modality has yet been developed to ideally treat tumor masses, the work here attempts to elucidate the variables that may be manipulated in order to achieve the greatest level of efficacy using current radiotherapy treatments. The use of nano-scale gold is becoming increasingly common in pharmaceutical applications, so the

assumption that it may be used to develop an effective radio-sensitizing contrast agent is easily valid. Furthermore, the geometric considerations discussed in this work can be manipulated to present an improved effective geometry in clinical settings. Choosing appropriate beam angles can allow for effective control of the tumor depth. While this may not be possible for deep-seated, soft tissue tumors, sub-surface and asymmetrical tumor locations may be candidates for such depth variance. Additionally, implementing both active and passive targeting strategies can allow for precise control of the *in situ* concentration of the gold nanoparticles.

It must be said that the idea of effective dose enhancement is not limited to radiation therapy using only photons. Boron Neutron Capture Therapy (BNCT) uses boron as a contrast agent for neutron therapy as its absorption cross-section is significantly higher than the corresponding cross section for tissue. A linear accelerator or nuclear reactor is used to produce neutrons that are then shaped into a useful beam using various moderators and collimators. As the beam travels through the patient, the neutrons are attenuated and become thermal. These neutrons are then absorbed by B^{10} that subsequently decays to produce Li^{7} and He^{4}. These ions produce significant ionization locally surrounding the interaction site. This method to produce localized effective dose can be compared to the effective dose enhancement described in this work here. However, BNCT has not been shown to significantly improve upon the current radiation therapies and so has not entered widespread clinical use. The difficulties in obtaining the neutron beams contribute to the delay in the acceptance of BNCT as a clinical therapy modality as the results are not improved to a level where the capital and logistic investments are feasible. As a result, using contrast media to achieve effective dose enhancement as described here is significantly more promising in existing photon therapy applications than in neutron therapy applications.

Although the work described here uses gold as the basis for radio-sensitizing contrast agents, several other candidates may be evaluated in the future. Both iodine and gadolinium have been studied in the past and shown relative success. However, a more promising candidate for further research may be platinum. Since its atomic number (78)

is very similar to that of gold (79), the electron density-dependent interactions mechanisms should be relatively identical. In addition, several organoplatinum compounds are currently under investigation for use in chemotherapeutic applications. Cisplatin, approved by the FDA since 1978, and its analogs have a platinum core, which may prove sufficient for radio-sensitizing applications once the drug is administered. These drugs affect cell death by inducing DNA cross-linking reactions in tumor cells. If drug administration is followed by radiation doses, the drug may act as the contrast agent necessary for effective dose enhancement. While cytotoxicity issues limit the concentrations that may be achieved i*n vivo*, it is conceivable that effective dose enhancement might be seen even at low doses.

6.3 Recommendations for future work

The broadest assumption made in the development of this work is that the contrast material distributes itself homogeneously in the target volume. While this assumption yields results that are sufficient to explain the overall interaction mechanisms and the major geometric variables, more detailed modeling is necessary to achieve clinically sufficient accuracy. There are several ways the results of this work may be extended to provide additional clinical relevance as described below.

Ideally, this work will be followed up by a microscopic treatment of the gold nanoparticles in the tissue sample to accurately model the specific photoelectric interactions that occur in the tumor volume. Designing and simulating a microscopically detailed model may prove to be very computationally expensive but may be accomplished by utilizing the computing power of one of several computing clusters currently available. Additionally, the models described here may need to be modified for Monte Carlo codes that do not use the condensed particle history approach to particle transport utilized by MCNP5. A detailed transport approach may more accurately predict where particle energy will be deposited in these simulations. Additionally, modeling the photon beam to include an energy spectrum may produce large improvements in effective

dose enhancement as compared to using mono-energetic photon beams due to the strong dependence on photon energy. Investigating the use of active targeting strategies such as monoclonal antibodies may also yield improved effective dose enhancement, as the amount of gold that reaches a tumor site may be significantly higher.

It is also worth mentioning that while this study acknowledges the limitations on the minimum photon energy that would be clinically feasible, a relative benefit analysis is not included here. A logical next step from this work would be to determine accurate dose profiles resulting from low-energy photon beams interacting with healthy tissue. The use of tissue phantoms in an experimental setting may be used to quantify these profiles. Alternatively, a microscopically detailed MC analysis of surface and shallow tissue depths may be warranted to validate the choice of sub-MeV photon beams in the models described here. The results of these dose profile studies may then be used to compare the effective dose enhancement obtained using nano-scale gold to the increased effective dose deposited in surface tissues due to lower photon energies.

These potential improvements notwithstanding, it is the author's opinion that the work presented here improves on the amount of data available to aid in the design of future *in vivo* investigations and is sufficient to motivate increased investigation into the uses of gold as a radio-sensitizing contrast agent.

REFERENCES

1. World Health Organization, *Cancer Fact Sheet no. 297.* 2009.
2. Danaei, G., et al., *Causes of cancer in the world: comparative risk assessment of nine behavioural and environmental risk factors.* Lancet, 2005. **366**(9499): p. 1784-1793.
3. Guerin, C., et al., *Recent advances in brain tumor therapy: local intracerebral drug delivery by polymers.* Investigational New Drugs, 2004. **22**(1): p. 27-37.
4. Fornari, F.A., et al., *Interference by Doxorubicin with DNA unwinding in MCF-7 breast-tumor cells.* Molecular Pharmacology, 1994. **45**(4): p. 649-656.
5. Tabaczar, S., et al., *Molecular mechanisms of antitumor activity of taxanes. I. Interaction of docetaxel with microtubules.* Postepy Higieny I Medycyny Doswiadczalnej, 2010. **64**: p. 568-581.
6. Furnari, F.B., et al., *Malignant astrocytic glioma: genetics, biology, and paths to treatment.* Genes & Development, 2007. **21**(21): p. 2683-2710.
7. Coen, J.J. and A.L. Zietman, *Proton radiation for localized prostate cancer.* Nat Rev Urol, 2009. **6**(6): p. 324-330.
8. Torchilin, V.P., *Targeted pharmaceutical nanocarriers for cancer therapy and Imaging.* Aaps Journal, 2007. **9**(2): p. E128-E147.
9. Duncan, R. and Y.N. Sat, *Tumour targeting by enhanced permeability and retention (EPR) effect.* Annals of Oncology, 1998. **9**: p. 149.
10. Maeda, H., *SMANCS and polymer-conjugated macromolecular drugs: advantages in cancer chemotherapy.* Advanced Drug Delivery Reviews, 2001. **46**(1-3): p. 169-185.
11. Arap, W., R. Pasqualini, and E. Ruoslahti, *Cancer treatment by targeted drug delivery to tumor vasculature in a mouse model.* Science, 1998. **279**(5349): p. 377-380.
12. Chithrani, B.D., A.A. Ghazani, and W.C.W. Chan, *Determining the size and shape dependence of gold nanoparticle uptake into mammalian cells.* Nano Letters, 2006. **6**(4): p. 662-668.
13. Stubbs, M., et al., *Causes and consequences of tumour acidity and implications for treatment.* Molecular Medicine Today, 2000. **6**(1): p. 15-19.
14. Berger, M.J., Hubbell, J.H., Seltzer, S.M., Chang, J., Courset, J.S., Sukumar, R., Zucker, D.S., Olsen, K., *XCOM: Photon Cross Section Database (version 1.5)*. 2010, National Institute of Standards and Technology, Gaithersburg, MD.
15. ICRU, *Radiation Quantities and Units*, in *Report 33*. 1980, International Comission on Radiation Units and Measurements: Bethesda, MD.
16. Hubbell, J.H., Seltzer, S.M, *Tables of X-Ray Mass Attenuation Coefficients and Mass Energy-Absoprtion Coefficients*. 2004, National Institute of Standards and Technology, Gaihersburg, MD.
17. Brown, C.L., et al., *Colloidal metallic gold is not bio-inert.* Inflammopharmacology, 2008. **16**(3): p. 133-137.

18. Alkilany, A.M. and C.J. Murphy, *Toxicity and cellular uptake of gold nanoparticles: what we have learned so far?* Journal of Nanoparticle Research, 2010. **12**(7): p. 2313-2333.
19. Cortie, M.B., *The weird world of nanoscale gold.* Gold Bulletin, 2004. **37**(1-2): p. 12-19.
20. Liu, H.B., et al., *Melting behavior of nanometer sized gold isomers.* Surface Science, 2001. **491**(1-2): p. 88-98.
21. Mie, G., *Beitrage zur Optik truber Medien, speziell kolloidaler Metallosungen.* Annalen der Physik, 1908. **Band 25**(No. 3): p. 377-445.
22. Alvarez, M.M., et al., *Optical absorption spectra of nanocrystal gold molecules.* Journal of Physical Chemistry B, 1997. **101**(19): p. 3706-3712.
23. Daniel, M.C. and D. Astruc, *Gold nanoparticles: Assembly, supramolecular chemistry, quantum-size-related properties, and applications toward biology, catalysis, and nanotechnology.* Chemical Reviews, 2004. **104**(1): p. 293-346.
24. Enustun, B.V. and J. Turkevich, *Coagulation of colloidal gold.* Journal of the American Chemical Society, 1963. **85**(21): p. 3317-&.
25. Grabar, K.C., et al., *Nanoscale characterization of gold colloid monolayers: A comparison of four techniques.* Analytical Chemistry, 1997. **69**(3): p. 471-477.
26. Yonezawa, T. and T. Kunitake, *Practical preparation of anionic mercapto ligand-stabilized gold nanoparticles and their immobilization.* Colloids and Surfaces a-Physicochemical and Engineering Aspects, 1999. **149**(1-3): p. 193-199.
27. Brust, M., et al., *Synthesis and reactions of functionalized gold nanoparticles.* Journal of the Chemical Society-Chemical Communications, 1995(16): p. 1655-1656.
28. Gomez, S., et al., *Gold nanoparticles from self-assembled gold(I) amine precursors.* Chemical Communications, 2000(19): p. 1945-1946.
29. Franzen, S., et al., *Optical properties of dye molecules adsorbed on single gold and silver nanoparticles.* Journal of Physical Chemistry A, 2002. **106**(28): p. 6533-6540.
30. Tkachenko, A.G., et al., *Multifunctional gold nanoparticle-peptide complexes for nuclear targeting.* Journal of the American Chemical Society, 2003. **125**(16): p. 4700-4701.
31. Mirkin, C.A., *Programming the assembly of two- and three-dimensional architectures with DNA and nanoscale inorganic building blocks.* Inorganic Chemistry, 2000. **39**(11): p. 2258-2272.
32. Wang, G.L., J. Zhang, and R.W. Murray, *DNA binding of an ethidium intercalator attached to a monolayer-protected gold cluster.* Analytical Chemistry, 2002. **74**(17): p. 4320-4327.
33. Mandal, T.K., M.S. Fleming, and D.R. Walt, *Preparation of polymer coated gold nanoparticles by surface-confined living radical polymerization at ambient temperature.* Nano Letters, 2002. **2**(1): p. 3-7.
34. Ohno, K., et al., *Synthesis of gold nanoparticles coated with well-defined, high-density polymer brushes by surface-initiated living radical polymerization.* Macromolecules, 2002. **35**(24): p. 8989-8993.

35. Raula, J., et al., *Synthesis of gold nanoparticles grafted with a thermoresponsive polymer by surface-induced reversible-addition-fragmentation chain-transfer polymerization.* Langmuir, 2003. **19**(8): p. 3499-3504.
36. Kim, D.J., et al., *Formation of thermoresponsive gold nanoparticle/PNIPAAm hybrids by surface-initiated, atom transfer radical polymerization in aqueous media.* Macromolecular Chemistry and Physics, 2005. **206**(19): p. 1941-1946.
37. Li, D.X., et al., *Fabrication of pH-responsive nanocomposites of gold nanoparticles/poly(4-vinylpyridine).* Chemistry of Materials, 2007. **19**(3): p. 412-417.
38. Shan, J. and H. Tenhu, *Recent advances in polymer protected gold nanoparticles: synthesis, properties and applications.* Chemical Communications, 2007(44): p. 4580-4598.
39. Conner, S.D. and S.L. Schmid, *Regulated portals of entry into the cell.* Nature, 2003. **422**(6927): p. 37-44.
40. Villiers, C.L., et al., *Analysis of the toxicity of gold nano particles on the immune system: effect on dendritic cell functions.* Journal of Nanoparticle Research, 2010. **12**(1): p. 55-60.
41. Goodman, C.M., et al., *Toxicity of gold nanoparticles functionalized with cationic and anionic side chains.* Bioconjugate Chemistry, 2004. **15**(4): p. 897-900.
42. Pan, Y., et al., *Gold Nanoparticles of Diameter 1.4 nm Trigger Necrosis by Oxidative Stress and Mitochondrial Damage.* Small, 2009. **5**(18): p. 2067-2076.
43. Turner, M., et al., *Selective oxidation with dioxygen by gold nanoparticle catalysts derived from 55-atom clusters.* Nature, 2008. **454**(7207): p. 981-U31.
44. Chen, Y.S., et al., *Assessment of the In Vivo Toxicity of Gold Nanoparticles.* Nanoscale Research Letters, 2009. **4**(8): p. 858-864.
45. Chithrani, B.D. and W.C.W. Chan, *Elucidating the mechanism of cellular uptake and removal of protein-coated gold nanoparticles of different sizes and shapes.* Nano Letters, 2007. **7**(6): p. 1542-1550.
46. Carter, P., *Improving the efficacy of antibody-based cancer therapies.* Nature Reviews Cancer, 2001. **1**(2): p. 118-129.
47. Kean, W.F. and I.R.L. Kean, *Clinical pharmacology of gold.* Inflammopharmacology, 2008. **16**(3): p. 112-125.
48. Higby, G.J., *Gold in medicine: a review of its use in the West before 1900.* Gold Bull, 1982. **15**(4): p. 130-40.
49. Roth, J., M. Bendayan, and L. Orci, *FITC-Protein-A-gold complex for light and electron-microscopic immunocytochemistry.* Journal of Histochemistry & Cytochemistry, 1980. **28**(1): p. 55-57.
50. Panyala, N.R., E.M. Pena-Mendez, and J. Havel, *Gold and nano-gold in medicine: overview, toxicology and perspectives.* Journal of Applied Biomedicine, 2009. **7**(2): p. 75-91.
51. Faulk, W.P. and G.M. Taylor, *Immunocolloid method for electron microscope.* Immunochemistry, 1971. **8**(11): p. 1081-&.

52. Mentlein, R., C. Buchholz, and B. Krisch, *Somatostatin-binding sites on rat telencephalic astrocytes - light-microscopic and electron-micriscopic studies invitro and invivo.* Cell and Tissue Research, 1990. **262**(3): p. 431-443.
53. Brust, M. and C.J. Kiely, *Some recent advances in nanostructure preparation from gold and silver particles: a short topical review.* Colloids and Surfaces a-Physicochemical and Engineering Aspects, 2002. **202**(2-3): p. 175-186.
54. Murphy, C.J., et al., *Gold Nanoparticles in Biology: Beyond Toxicity to Cellular Imaging.* Accounts of Chemical Research, 2008. **41**(12): p. 1721-1730.
55. Kumar, S., et al., *Plasmonic nanosensors for imaging intracellular biomarkers in live cells.* Nano Letters, 2007. **7**(5): p. 1338-1343.
56. Jiang, W., et al., *Nanoparticle-mediated cellular response is size-dependent.* Nature Nanotechnology, 2008. **3**(3): p. 145-150.
57. Eghtedari, M., et al., *Engineering of Hetero-Functional Gold Nanorods for the in vivo Molecular Targeting of Breast Cancer Cells.* Nano Letters, 2009. **9**(1): p. 287-291.
58. Boisselier, E. and D. Astruc, *Gold nanoparticles in nanomedicine: preparations, imaging, diagnostics, therapies and toxicity.* Chem Soc Rev, 2009. **38**(6): p. 1759-82.
59. Feldherr, C.M. and D. Akin, *Variations in signal-mediated nuclear transport during the cell-cycle in BALB/C 3T3 cells.* Experimental Cell Research, 1994. **215**(1): p. 206-210.
60. Feldherr, C.M. and D. Akin, *Signal-mediated nuclear transport in proliferating and growth-arrested BALB/C 3T3 cells.* Journal of Cell Biology, 1991. **115**(4): p. 933-939.
61. Feldherr, C.M. and D. Akin, *The location of the transport gate in the nuclear pore complex.* Journal of Cell Science, 1997. **110**: p. 3065-3070.
62. Feldherr, C.M. and D. Akin, *Signal-mediated nuclear transport in the amoeba.* Journal of Cell Science, 1999. **112**(12): p. 2043-2048.
63. Zhang, F., et al., *A transfecting peptide derived from adenovirus fiber protein.* Gene Therapy, 1999. **6**(2): p. 171-181.
64. Jain, P.K., et al., *Calculated absorption and scattering properties of gold nanoparticles of different size, shape, and composition: Applications in biological imaging and biomedicine.* Journal of Physical Chemistry B, 2006. **110**(14): p. 7238-7248.
65. Elghanian, R., et al., *Selective colorimetric detection of polynucleotides based on the distance-dependent optical properties of gold nanoparticles.* Science, 1997. **277**(5329): p. 1078-1081.
66. Han, M.S., et al., *Colorimetric screening of DNA-binding molecules with gold nanoparticle probes.* Angewandte Chemie-International Edition, 2006. **45**(11): p. 1807-1810.
67. Medley, C.D., et al., *Gold nanoparticle-based colorimetric assay for the direct detection of cancerous cells.* Analytical Chemistry, 2008. **80**(4): p. 1067-1072.
68. Matsudaira, H., A.M. Ueno, and I. Furuno, *Iodine contrast-medium sensitizes cultured mammalian-cells to x-rays but not to gamma-rays.* Radiation Research, 1980. **84**(1): p. 144-148.

69. Nath, R., P. Bongiorni, and S. Rockwell, *Iododeoxyuridine radiosensitization by low-energy and high-energy photons for brachytherapy dose-rates.* Radiation Research, 1990. **124**(3): p. 249-258.
70. Mello, R.S., et al., *Radiation-dose enhancement in tumors with iodine.* Medical Physics, 1983. **10**(1): p. 75-78.
71. Rose, J.H., et al., *First radiotherapy of human metastatic brain tumors delivered by a computerized tomography scanner (CTRx).* International Journal of Radiation Oncology Biology Physics, 1999. **45**(5): p. 1127-1132.
72. Garnica-Garza, H.M., *Treatment planning considerations in contrast-enhanced radiotherapy: energy and beam aperture optimization.* Physics in Medicine and Biology, 2011. **56**(2): p. 341-355.
73. Robar, J.L., S.A. Riccio, and M.A. Martin, *Tumour dose enhancement using modified megavoltage photon beams and contrast media.* Physics in Medicine and Biology, 2002. **47**(14): p. 2433-2449.
74. Cho, S.H., *Estimation of tumour dose enhancement due to gold nanoparticles during typical radiation treatments: a preliminary Monte Carlo study.* Physics in Medicine and Biology, 2005. **50**(15): p. N163-N173.
75. McMahon, S.J., et al., *Radiotherapy in the presence of contrast agents: a general figure of merit and its application to gold nanoparticles.* Physics in Medicine and Biology, 2008. **53**(20): p. 5635-5651.
76. Hainfeld, J.F., D.N. Slatkin, and H.M. Smilowitz, *The use of gold nanoparticles to enhance radiotherapy in mice.* Physics in Medicine and Biology, 2004. **49**(18): p. N309-N315.
77. Hainfeld, J.F., et al., *Gold nanoparticles: a new X-ray contrast agent.* British Journal of Radiology, 2006. **79**(939): p. 248-253.
78. Butterworth, K.T., et al., *Evaluation of cytotoxicity and radiation enhancement using 1.9 nm gold particles: potential application for cancer therapy.* Nanotechnology, 2010. **21**(29).
79. Chithrani, D.B., et al., *Gold Nanoparticles as Radiation Sensitizers in Cancer Therapy.* Radiation Research, 2010. **173**(6): p. 719-728.
80. Zhang, S.X., et al., *Quantifying tumor-selective radiation dose enhancements using gold nanoparticles: a monte carlo simulation study.* Biomedical Microdevices, 2009. **11**(4): p. 925-933.
81. Cho, S.H., B.L. Jones, and S. Krishnan, *The dosimetric feasibility of gold nanoparticle-aided radiation therapy (GNRT) via brachytherapy using low-energy gamma-/x-ray sources.* Physics in Medicine and Biology, 2009. **54**(16): p. 4889-4905.
82. Team, X.-M.C., *MCNP - A General Monte Carlo N-Particle Transport Code LA-UR-03-1987*. 2003, Los Alamos National Laboratory: Los Alamos, NM.
83. Van den Heuvel, F., J.P. Locquet, and S. Nuyts, *Beam energy considerations for gold nano-particle enhanced radiation treatment.* Physics in Medicine and Biology, 2010. **55**(16): p. 4509-4520.
84. ICRP, *Basic Anatomical and Physiological Data for Use in Radiological Protection Reference Values*, in *Ann. ICRP 32 (3-4)*. 2002, International Commission on Radiation Protection.

85. Popescu, G., et al., *Optical imaging of cell mass and growth dynamics.* American Journal of Physiology-Cell Physiology, 2008. **295**(2): p. C538-C544.

APPENDIX A

Detailed geometries for MC models

Given here are detailed representations of the geometries used in the input files that follow. Although an attempt has been made to accurately scale the tissue volume, the distance between the source plane and the tissue volume is not drawn to scale. The distance between the source plane and the tissue volume is kept constant at 2 cm in all models and has been omitted from these diagrams purely for the sake of clarity to avoid obscuring the detailed rendering of the tissue volume.

Fig. A-1 below describes the overall geometry for the preliminary model with overall dimensions of 20 cm by 20 cm by 20 cm. The slabs are 2 cm thick throughout the tissue volume, and the tumor slab designation depends on the specific model being run.

Fig. A-2 below describes the overall geometry for the detailed model with overall dimensions of 10 cm by 10 cm by 10 cm. The slabs throughout the volume are 1 cm thick, and the tumor slab is further divided into 0.25 cm slices. For the detailed model, the tumor slab was kept at a constant depth of 4.5 cm, and a 0.5 cm skin layer was also modeled.

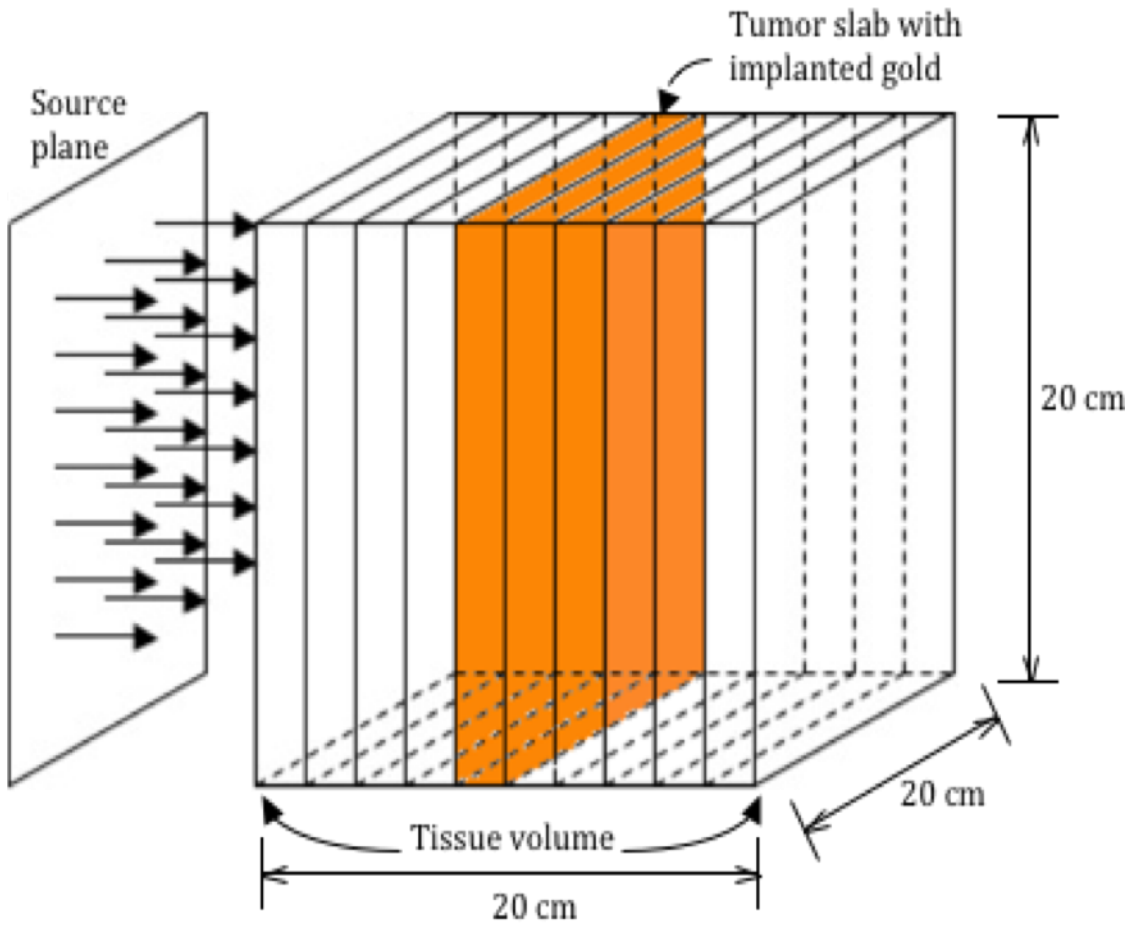

Figure A-1: Explicitly defined geometry for preliminary model. Tissue volume is not shown to scale.

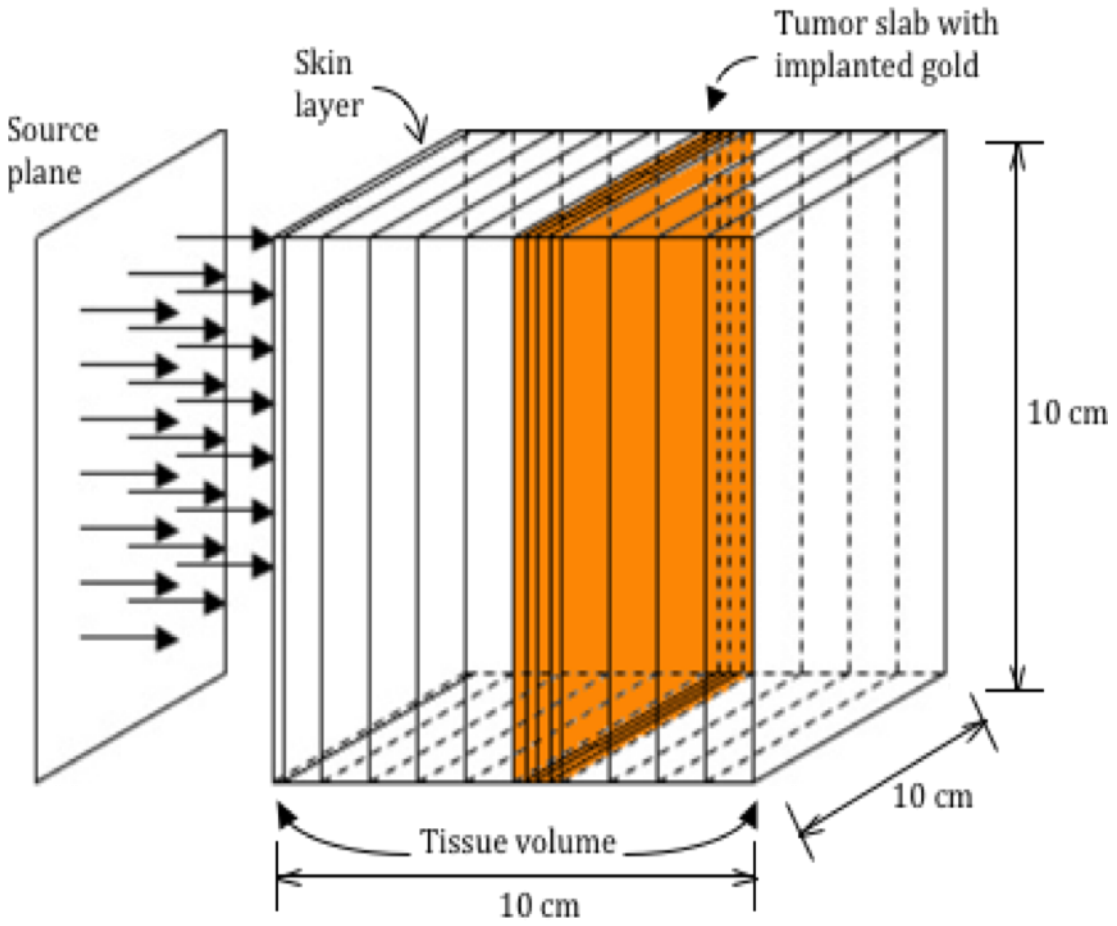

Figure A-2: Explicitly defined geometry for detailed model. Tissue volume is not shown to scale.

APPENDIX B

Sample input and output files from MCNP5 simulations

Given below are sample input files for the simulations run in this work. One input file is included for each model with the relevant variables marked in bold.

Preliminary model – Sample input:

```
c Gamma ray beam source with Au
c
c Input simulates gamma ray source 2 cm left of origin
c Gamma ray source strength = 0.10 MeV [Varied for source dependence]
c Au concentration in tissue = 0.7%  [Varied for concentration dependence]
c Tumor depth in tissue = 5 cm [Varied for depth dependence]
c Last edited on: Wednesday, February 2, 2011
c
c ----------------------  Cells, regions definition ---------------------------
c The source is assumed to be planar, aimed at the left edge of the tissue
c The cells are defined as inside the boundary box and left/right of
c the different y-planes slicing through at 2 cm intervals.
c Density: Healthy tissue    m1 =  1.07 g/cm3
c          Tumor with Au     m2 =  1.1977 g/cm3
c
   1  0           -1  -2      $ Vacuum behind source plane
   2  0           -1   2  -3  $ Source on the left edge of cell
   3  1  -1.07    -1   3  -4  $ Healthy tissue
   4  1  -1.07    -1   4  -5  $ Healthy tissue
   5  1  -1.07    -1   5  -6  $ Healthy tissue
   6  1  -1.07    -1   6  -7  $ Healthy tissue
   7  2  -1.1977  -1   7  -8  $ Tumor with 0.70% Au
   8  1  -1.07    -1   8  -9  $ Healthy tissue
   9  1  -1.07    -1   9  -10 $ Healthy tissue
  10  1  -1.07    -1  10  -11 $ Healthy tissue
  11  1  -1.07    -1  11  -12 $ Healthy tissue
  12  1  -1.07    -1  12      $ Healthy tissue
  13  0           1           $ Vacuum outside problem boundary [outside box]

c ----------------------       Surfaces / Bodies    ----------------------
  1  RPP  -10 10  -2.001 20  -10 10  $ Box macro-body, L=W=H=20
  2  py  -2.0                       $ Surface plane
  3  py   0.0                       $ Slices in the y-plane
  4  py   2.0                       $
  5  py   4.0                       $
  6  py   6.0                       $
  7  py   8.0                       $
  8  py  10.0                       $
  9  py  12.0                       $
 10  py  14.0                       $
 11  py  16.0                       $
 12  py  18.0                       $

c ----------------------     Problem definition     ----------------------
```

```
c        1 2 3 4 5 6 7 8 9 0 1 2 3    $ Cell numbering
  imp:p  0 1 1 1 1 1 1 1 1 1 1 1 0    $ photons disappear at boundary
  mode p                              $ Photon transport (no secondary e)
  nps 150000                          $ Number of histories
c
c ----------------------    Source definition     ------------------------
  sdef par = 2             $ Photon source
       erg = 0.10          $ Energy level [MeV]
       sur = 2             $ Source points sampled over surface 2 at y = -2
       vec = 0 1 0         $ Reference vector (Source in +y direction)
       dir = 1             $ Cos of angle between vec and beam vector
       pos = 0 -2 0        $ Center of sampling range (0,-2,0)
       rad = d1            $ Beam width distribution
  SI1 0 10                 $ Source sampled over r=0 to r=10
  SP1 -21 1                $ Power rule with a=1 (Constant sampling)
c
c ----------------------    Response functions    ------------------------
  f14:p   3 4 5 6 7 8 9 10 11 12   $ Average p flux in cells 3-12 [num/cm2]
  f16:p   3 4 5 6 7 8 9 10 11 12   $ Energy deposition in  3-12 [MeV/g]
c
c ----------------------    Materials             ------------------------
c Composition of bodily materials
c
  m1    1000.04p       -0.1020         $ Healthy tissue
        6000.04p       -0.1430
        7000.04p       -0.0340
        8000.04p       -0.7100
       11000.04p       -0.0010
       15000.04p       -0.0020
       16000.04p       -0.0030
       17000.04p       -0.0010
       19000.04p       -0.0040
c
  m2    1000.04p       -0.1013        $ "Tumor" layer with diffused Au
        6000.04p       -0.1420
        7000.04p       -0.0337
        8000.04p       -0.7050
       11000.04p       -0.0010
       15000.04p       -0.0020
       16000.04p       -0.0030
       17000.04p       -0.0010
       19000.04p       -0.0040
       79000.04p       -0.0070        $ 0.70 % mass fraction of gold
```

Preliminary model – Sample output file

```
          Thread Name & Version = MCNP5_RSICC, 1.51

                                  _
            ._ _    _  ._   ._   |_
            | | |  (_  | |  |_)   _)
                           |

  +---------------------------------------------------------------------+
  | Copyright 2008. Los Alamos National Security, LLC.  All rights      |
  | reserved.                                                           |
  |   This material was produced under U.S. Government contract         |
  | DE-AC52-06NA25396 for Los Alamos National Laboratory, which is      |
  | operated by Los Alamos National Security, LLC, for the U.S.         |
  | Department of Los Energy. The Government is granted for itself and  |
  | others acting on its behalf a paid-up, nonexclusive, irrevocable    |
  | worldwide license in this material to reproduce, prepare derivative |
  | works, and perform publicly and display publicly. Beginning five    |
  | (5) years after 2008, subject to additional five-year worldwide     |
  | renewals, the Government is granted for itself and others acting on |
  | its behalf a paid-up, nonexclusive, irrevocable worldwide license   |
  | in this material to reproduce, prepare derivative works, distribute |
  | copies to the public, perform publicly and display publicly, and to |
  | permit others to do so. NEITHER THE UNITED STATES NOR THE UNITED    |
  | STATES DEPARTMENT OF ENERGY, NOR LOS ALAMOS NATIONAL SECURITY, LLC, |
  | NOR ANY OF THEIR EMPLOYEES, MAKES ANY WARRANTY, EXPRESS OR IMPLIED, |
  | OR ASSUMES ANY LEGAL LIABILITY OR RESPONSIBILITY FOR THE ACCURACY,  |
  | COMPLETENESS, OR USEFULNESS OF ANY INFORMATION, APPARATUS, PRODUCT, |
  | OR PROCESS DISCLOSED, OR REPRESENTS THAT ITS USE WOULD NOT INFRINGE |
  | PRIVATELY OWNED RIGHTS.                                             |
  +---------------------------------------------------------------------+

1mcnp     version 5     ld=01232009                    02/02/11 17:05:54
 ***********************************************************************                probid =  02/02/11 17:05:54
 i=010Au.txt o=r010a.txt

      1-       c Gamma ray beam source with Au
      2-       c
      3-       c Input simulates gamma ray source 2 cm left of origin
      4-       c Gamma ray source strength = 0.10 MeV
      5-       c Au concentration in tissue = 0.70%
      6-       c Tumor:tissue Au ratio = No diffusion
      7-       c Last edited on: Wednesday, February 2, 2011
      8-       c
      9-       c ----------------------   Cells, regions definition ----------------------------
     10-       c The source is assumed to be planar, aimed at the left edge of the tissue
```

```
c The cells are defined as inside the boundary box and left/right of
c the different y-planes slicing through at 2 cm intervals.
c Density: Healthy tissue    m1 =  1.07 g/cm3
c          Blood with Au     m2 =  1.05 g/cm3
c          Tumor with Au     m3 =  1.07 g/cm3
c          Tissue with Au    m4 =  1.1977 g/cm3
c
   1  0          -1  -2      $ Vacuum behind source plane
   2  0          -1   2  -3  $ Source on the left edge of cell
   3  1  -1.07   -1   3  -4  $ Healthy tissue
   4  1  -1.07   -1   4  -5  $ Healthy tissue
   5  1  -1.07   -1   5  -6  $ Healthy tissue
   6  1  -1.07   -1   6  -7  $ Healthy tissue
   7  3  -1.1977 -1   7  -8  $ Tissue with 0.70% Au
   8  1  -1.07   -1   8  -9  $ Healthy tissue
   9  1  -1.07   -1   9  -10 $ Healthy tissue
  10  1  -1.07   -1  10  -11 $ Healthy tissue
  11  1  -1.07   -1  11  -12 $ Healthy tissue
  12  1  -1.07   -1  12      $ Healthy tissue
  13  0          1           $ Vacuum outside problem boundary [outside box]

c ----------------------       Surfaces / Bodies    ----------------------
  1  RPP  -10 10  -2.001 20  -10 10  $ Box macro-body, L=W=H=20
  2  py  -2.0                       $ Surface plane
  3  py   0.0                       $ Slices in the y-plane
  4  py   2.0                       $
  5  py   4.0                       $
  6  py   6.0                       $
  7  py   8.0                       $
  8  py  10.0                       $
  9  py  12.0                       $
 10  py  14.0                       $
 11  py  16.0                       $
 12  py  18.0                       $

c ----------------------     Problem definition     ----------------------
c        1 2 3 4 5 6 7 8 9 0 1 2 3    $ Cell numbering
  imp:p  0 1 1 1 1 1 1 1 1 1 1 1 0    $ photons disappear at boundary
  mode p                              $ Photon transport (no secondary e)
  nps 150000                          $ Number of histories
c
c ----------------------    Source definition     ------------------------
  sdef par = 2            $ Photon source
       erg = 0.10         $ Energy level [MeV]
       sur = 2            $ Source points sampled over surface 2 at y = -2
       vec = 0 1 0        $ Reference vector (Source in +y direction)
```

```
     57-              dir = 1            $ Cos of angle between vec and beam vector
     58-              pos = 0 -2 0       $ Center of sampling range (0,-2,0)
     59-              rad = d1           $ Beam width distribution
     60-         SI1 0 10                $ Source sampled over r=0 to r=10
     61-         SP1 -21 1               $ Power rule with a=1 (Constant sampling)
     62-       c
     63-       c ----------------------    Response functions    ------------------------
     64-         f14:p   3 4 5 6 7 8 9 10 11 12   $ Average p flux in cells 3-12 [num/cm2]
     65-         f16:p   3 4 5 6 7 8 9 10 11 12   $ Energy deposition in  3-12 [MeV/g]
     66-       c
     67-       c ----------------------    Materials             ------------------------
     68-       c Composition of bodily materials
     69-       c
     70-         m1    1000.04p       -0.1020         $ Healthy tissue
     71-               6000.04p       -0.1430
     72-               7000.04p       -0.0340
     73-               8000.04p       -0.7100
     74-              11000.04p       -0.0010
     75-              15000.04p       -0.0020
     76-              16000.04p       -0.0030
     77-              17000.04p       -0.0010
     78-              19000.04p       -0.0040
     79-       c
     80-         m3    1000.04p       -0.1013        $ "Tumor" layer with diffused Au
     81-               6000.04p       -0.1420
     82-               7000.04p       -0.0337
     83-               8000.04p       -0.7050
     84-              11000.04p       -0.0010
     85-              15000.04p       -0.0020
     86-              16000.04p       -0.0030
     87-              17000.04p       -0.0010
     88-              19000.04p       -0.0040
     89-              79000.04p       -0.0070        $ 0.70 % mass fraction of gold
1cells                                                                          print table 60

                    atom        gram                                    photon
      cell  mat    density     density     volume       mass     pieces importance

     1     1    0  0.00000E+00 0.00000E+00 4.00000E-01 0.00000E+00     0  0.0000E+00
     2     2    0  0.00000E+00 0.00000E+00 8.00000E+02 0.00000E+00     0  1.0000E+00
     3     3    1  1.03249E-01 1.07000E+00 8.00000E+02 8.56000E+02     0  1.0000E+00
     4     4    1  1.03249E-01 1.07000E+00 8.00000E+02 8.56000E+02     0  1.0000E+00
     5     5    1  1.03249E-01 1.07000E+00 8.00000E+02 8.56000E+02     0  1.0000E+00
     6     6    1  1.03249E-01 1.07000E+00 8.00000E+02 8.56000E+02     0  1.0000E+00
     7     7    3  1.14795E-01 1.19770E+00 8.00000E+02 9.58160E+02     0  1.0000E+00
     8     8    1  1.03249E-01 1.07000E+00 8.00000E+02 8.56000E+02     0  1.0000E+00
```

```
     9     9    1  1.03249E-01 1.07000E+00 8.00000E+02 8.56000E+02     0  1.0000E+00
    10    10    1  1.03249E-01 1.07000E+00 8.00000E+02 8.56000E+02     0  1.0000E+00
    11    11    1  1.03249E-01 1.07000E+00 8.00000E+02 8.56000E+02     0  1.0000E+00
    12    12    1  1.03249E-01 1.07000E+00 8.00000E+02 8.56000E+02     0  1.0000E+00
    13    13    0  0.00000E+00 0.00000E+00 0.00000E+00 0.00000E+00     0  0.0000E+00

 total                                    8.80040E+03 8.66216E+03

    minimum source weight = 1.0000E+00    maximum source weight = 1.0000E+00

 ************************************************
 * Random Number Generator  =                   1 *
 * Random Number Seed       =       19073486328125 *
 * Random Number Multiplier =       19073486328125 *
 * Random Number Adder      =                   0 *
 * Random Number Bits Used  =                  48 *
 * Random Number Stride     =              152917 *
 ************************************************

1cross-section tables                                                                    print table 100

     table    length

                        tables from file mcplib04

   1000.04p    1898  ENDF/B-VI Release 8 Photoatomic Data for 1-H                  mat 100      02/07/03
   6000.04p    3152  ENDF/B-VI Release 8 Photoatomic Data for 6-C                  mat 600      02/07/03
   7000.04p    3194  ENDF/B-VI Release 8 Photoatomic Data for 7-N                  mat 700      02/07/03
   8000.04p    3272  ENDF/B-VI Release 8 Photoatomic Data for 8-O                  mat 800      02/07/03
  11000.04p    3995  ENDF/B-VI Release 8 Photoatomic Data for 11-NA                mat1100      02/07/03
  15000.04p    4498  ENDF/B-VI Release 8 Photoatomic Data for 15-P                 mat1500      02/07/03
  16000.04p    4654  ENDF/B-VI Release 8 Photoatomic Data for 16-S                 mat1600      02/07/03
  17000.04p    4738  ENDF/B-VI Release 8 Photoatomic Data for 17-CL                mat1700      02/07/03
  19000.04p    5047  ENDF/B-VI Release 8 Photoatomic Data for 19-K                 mat1900      02/07/03
  79000.04p    9881  ENDF/B-VI Release 8 Photoatomic Data for 79-AU                mat7900      02/07/03

  total       44329

 maximum photon energy set to  100.0 mev (maximum electron energy)

                        tables from file el03

   1000.03e    2329                                                                    6/6/98
   6000.03e    2333                                                                    6/6/98
   7000.03e    2333                                                                    6/6/98
   8000.03e    2333                                                                    6/6/98
```

```
  11000.03e    2337                                                                                    6/6/98
  15000.03e    2339                                                                                    6/6/98
  16000.03e    2339                                                                                    6/6/98
  17000.03e    2339                                                                                    6/6/98
  19000.03e    2343                                                                                    6/6/98
  79000.03e    2371                                                                                    6/6/98

 ************************************************************************************************************************

 dump no.    1 on file runtpf     nps =           0     coll =              0     ctm =        0.00    nrn =
    0
1problem summary

      run terminated when      150000  particle histories were done.
+                                                                                          02/02/11 17:06:00
      c Gamma ray beam source with Au                                                probid =  02/02/11 17:05:54
0
 photon creation     tracks      weight        energy           photon loss         tracks      weight        energy
                                 (per source particle)                                         (per source particle)

 source              150000    1.0000E+00    1.0000E-01         escape              116622    7.7748E-01    5.6739E-02
                                                                 energy cutoff            0    0.            8.8690E-07
                                                                 time cutoff              0    0.            0.
 weight window            0    0.            0.                 weight window            0    0.            0.
 cell importance          0    0.            0.                 cell importance          0    0.            0.
 weight cutoff            0    0.            0.                 weight cutoff            0    0.            0.
 e or t importance        0    0.            0.                 e or t importance        0    0.            0.
 dxtran                   0    0.            0.                 dxtran                   0    0.            0.
 forced collisions        0    0.            0.                 forced collisions        0    0.            0.
 exp. transform           0    0.            0.                 exp. transform           0    0.            0.
 from neutrons            0    0.            0.                 compton scatter          0    0.            2.9043E-02
 bremsstrahlung         263    1.7533E-03    9.8518E-06         capture              40622    2.7081E-01    1.6365E-02
 p-annihilation           0    0.            0.                 pair production          0    0.            0.
 photonuclear             0    0.            0.                 photonuclear abs         0    0.            0.
 electron x-rays          0    0.            0.
 1st fluorescence      5991    3.9940E-02    2.0706E-03
 2nd fluorescence       990    6.6000E-03    6.7989E-05
     total           157244    1.0483E+00    1.0215E-01             total           157244    1.0483E+00    1.0215E-01

   number of photons banked                    1253        average time of (shakes)              cutoffs
   photon tracks per source particle      1.0483E+00         escape            6.0104E-02         tco   1.0000E+33
   photon collisions per source particle  3.3349E+00         capture           6.0101E-02         eco   1.0000E-03
   total photon collisions                   500228         capture or escape 6.0104E-02         wc1  -5.0000E-01
                                                            any termination   6.0104E-02         wc2  -2.5000E-01

 computer time so far in this run     0.10 minutes           maximum number ever in bank         2
```

```
 computer time in mcrun               0.09 minutes            bank overflows to backup file       0
 source particles per minute            1.6099E+06
 random numbers generated                  8412307            most random numbers used was         356 in history      113022

 range of sampled source weights = 1.0000E+00 to 1.0000E+00
1photon   activity in each cell                                                                          print table 126
```

cell	tracks entering	population	collisions	collisions * weight (per history)	number weighted energy	flux weighted energy	average track weight (relative)	average track mfp (cm)
2	189152	150002	0	0.0000E+00	9.1367E-02	9.1367E-02	1.0000E+00	0.0000E+00
3	185402	150051	93212	6.2141E-01	8.7074E-02	8.7074E-02	1.0000E+00	5.2192E+00
4	162932	127418	88662	5.9108E-01	8.3794E-02	8.3794E-02	1.0000E+00	5.1310E+00
5	135996	105572	76685	5.1123E-01	8.1699E-02	8.1699E-02	1.0000E+00	5.0723E+00
6	109955	85949	63770	4.2513E-01	8.0156E-02	8.0156E-02	1.0000E+00	5.0296E+00
7	86205	69362	66320	4.4213E-01	7.8968E-02	7.8968E-02	1.0000E+00	3.7591E+00
8	61672	48988	36673	2.4449E-01	7.7500E-02	7.7500E-02	1.0000E+00	4.9536E+00
9	47154	37810	28466	1.8977E-01	7.6700E-02	7.6700E-02	1.0000E+00	4.9274E+00
10	35310	28865	21296	1.4197E-01	7.6107E-02	7.6107E-02	1.0000E+00	4.9060E+00
11	25603	21966	15237	1.0158E-01	7.6262E-02	7.6262E-02	1.0000E+00	4.9092E+00
12	17174	16488	9907	6.6047E-02	7.7841E-02	7.7841E-02	1.0000E+00	4.9550E+00
total	1056555	842471	500228	3.3349E+00				

```
1tally  14        nps =      150000
          tally type 4    track length estimate of particle flux.      units   1/cm**2
          tally for  photons

          volumes
                  cell:        3            4            5            6            7            8            9
                       8.00000E+02  8.00000E+02  8.00000E+02  8.00000E+02  8.00000E+02  8.00000E+02  8.00000E+02
                  cell:       10           11           12
                       8.00000E+02  8.00000E+02  8.00000E+02

 cell  3
                 3.98781E-03 0.0019

 cell  4
                 3.73219E-03 0.0025

 cell  5
                 3.19293E-03 0.0030

 cell  6
                 2.61679E-03 0.0035
```

```
 cell  7
                1.96796E-03 0.0040

 cell  8
                1.48015E-03 0.0051

 cell  9
                1.13719E-03 0.0060

 cell  10
                8.49315E-04 0.0070

 cell  11
                6.07439E-04 0.0082

 cell  12
                4.02034E-04 0.0094
```

```
============================================================================================================================================

           results of 10 statistical checks for the estimated answer for the tally fluctuation chart (tfc) bin of tally  14

 tfc bin     --mean--      ---------relative error---------      ----variance of the variance----      --figure of merit--     -
pdf-
 behavior    behavior      value   decrease   decrease rate      value   decrease   decrease rate       value     behavior
slope

 desired      random       <0.10      yes      1/sqrt(nps)       <0.10      yes        1/nps           constant    random
>3.00
 observed     random        0.00      yes          yes            0.00      yes         yes            constant    random
10.00
 passed?        yes          yes      yes          yes              yes      yes         yes               yes        yes
yes

============================================================================================================================================


 this tally meets the statistical criteria used to form confidence intervals: check the tally fluctuation chart to verify.
 the results in other bins associated with this tally may not meet these statistical criteria.

 ----- estimated confidence intervals:  -----
```

```
 estimated asymmetric confidence interval(1,2,3 sigma): 3.9802E-03 to 3.9955E-03; 3.9725E-03 to 4.0032E-03; 3.9648E-03 to 4.0108E-
03
 estimated  symmetric confidence interval(1,2,3 sigma): 3.9801E-03 to 3.9955E-03; 3.9725E-03 to 4.0031E-03; 3.9648E-03 to 4.0108E-
03

1analysis of the results in the tally fluctuation chart bin (tfc) for tally  14 with nps =      150000  print table 160


 normed average tally per history  = 3.98781E-03          unnormed average tally per history  = 3.19025E+00
 estimated tally relative error    = 0.0019               estimated variance of the variance  = 0.0001
 relative error from zero tallies  = 0.0000               relative error from nonzero scores  = 0.0019

 number of nonzero history tallies =      150000          efficiency for the nonzero tallies  = 1.0000
 history number of largest  tally  =       88926          largest  unnormalized history tally = 3.25361E+01
 (largest  tally)/(average tally)  = 1.01986E+01          (largest  tally)/(avg nonzero tally)= 1.01986E+01

 (confidence interval shift)/mean  = 0.0000               shifted confidence interval center  = 3.98784E-03


 if the largest  history score sampled so far were to occur on the next history, the tfc bin quantities would change as follows:

      estimated quantities           value at nps           value at nps+1           value(nps+1)/value(nps)-1.

      mean                            3.98781E-03             3.98805E-03                    0.000061
      relative error                  1.92268E-03             1.92353E-03                    0.000440
      variance of the variance        9.56346E-05             9.64533E-05                    0.008560
      shifted center                  3.98784E-03             3.98784E-03                    0.000000
      figure of merit                 2.90339E+06             2.90084E+06                   -0.000880

 the estimated slope of the 200 largest  tallies starting at  1.91771E+01 appears to be decreasing at least exponentially.
 the large score tail of the empirical history score probability density function appears to have no unsampled regions.

 fom = (histories/minute)*(f(x) signal-to-noise ratio)**2 = (1.610E+06)*( 1.343E+00)**2 = (1.610E+06)*(1.803E+00) = 2.903E+06

1tally  16        nps =      150000
           tally type 6    track length estimate of heating.            units   mev/gram
           tally for  photons

           masses
                   cell:       3           4           5           6           7           8           9
                         8.56000E+02 8.56000E+02 8.56000E+02 8.56000E+02 9.58160E+02 8.56000E+02 8.56000E+02
                   cell:      10          11          12
                         8.56000E+02 8.56000E+02 8.56000E+02


 cell  3
                9.36895E-06 0.0018
```

```
 cell  4
                8.66764E-06 0.0024

 cell  5
                7.37399E-06 0.0029

 cell  6
                6.01796E-06 0.0034

 cell  7
                7.75445E-06 0.0041

 cell  8
                3.38455E-06 0.0051

 cell  9
                2.60160E-06 0.0060

 cell  10
                1.94780E-06 0.0070

 cell  11
                1.39566E-06 0.0082

 cell  12
                9.26255E-07 0.0093


================================================================================================================================

           results of 10 statistical checks for the estimated answer for the tally fluctuation chart (tfc) bin of tally  16

 tfc bin     --mean--      ---------relative error---------      ----variance of the variance----      --figure of merit--     -
pdf-
 behavior    behavior      value    decrease    decrease rate      value    decrease    decrease rate       value     behavior
slope

 desired      random       <0.10       yes       1/sqrt(nps)       <0.10       yes         1/nps           constant    random
>3.00
 observed     random        0.00       yes           yes            0.00       yes          yes            constant    random
10.00
 passed?        yes           yes      yes           yes              yes      yes          yes               yes         yes
yes
```

```
================================================================================================================================

 this tally meets the statistical criteria used to form confidence intervals: check the tally fluctuation chart to verify.
 the results in other bins associated with this tally may not meet these statistical criteria.

 ----- estimated confidence intervals:  -----

 estimated asymmetric confidence interval(1,2,3 sigma): 9.3526E-06 to 9.3855E-06; 9.3361E-06 to 9.4019E-06; 9.3196E-06 to 9.4184E-
06
 estimated  symmetric confidence interval(1,2,3 sigma): 9.3525E-06 to 9.3854E-06; 9.3360E-06 to 9.4019E-06; 9.3196E-06 to 9.4183E-
06

1analysis of the results in the tally fluctuation chart bin (tfc) for tally  16 with nps =      150000  print table 160


 normed average tally per history  = 9.36895E-06          unnormed average tally per history  = 8.01982E-03
 estimated tally relative error    = 0.0018               estimated variance of the variance  = 0.0001
 relative error from zero tallies  = 0.0000               relative error from nonzero scores  = 0.0018

 number of nonzero history tallies =      150000          efficiency for the nonzero tallies  = 1.0000
 history number of largest  tally  =       70280          largest  unnormalized history tally = 9.54591E-02
 (largest  tally)/(average tally)  = 1.19029E+01          (largest  tally)/(avg nonzero tally)= 1.19029E+01

 (confidence interval shift)/mean  = 0.0000               shifted confidence interval center  = 9.36902E-06


 if the largest  history score sampled so far were to occur on the next history, the tfc bin quantities would change as follows:

      estimated quantities           value at nps           value at nps+1           value(nps+1)/value(nps)-1.

      mean                            9.36895E-06             9.36963E-06                    0.000073
      relative error                  1.75661E-03             1.75798E-03                    0.000776
      variance of the variance        1.17050E-04             1.19540E-04                    0.021274
      shifted center                  9.36902E-06             9.36902E-06                    0.000000
      figure of merit                 3.47831E+06             3.47292E+06                   -0.001551

 the estimated slope of the 200 largest  tallies starting at  4.70539E-02 appears to be decreasing at least exponentially.
 the large score tail of the empirical history score probability density function appears to have no unsampled regions.

 fom = (histories/minute)*(f(x) signal-to-noise ratio)**2 = (1.610E+06)*( 1.470E+00)**2 = (1.610E+06)*(2.161E+00) = 3.478E+06

1status of the statistical checks used to form confidence intervals for the mean for each tally bin
```

tally   result of statistical checks for the tfc bin (the first check not passed is listed) and error magnitude check for all bins

   14   passed the 10 statistical checks for the tally fluctuation chart bin result
        passed all bin error check: 10 tally bins all have relative errors less than 0.10 with no zero bins

   16   passed the 10 statistical checks for the tally fluctuation chart bin result
        passed all bin error check: 10 tally bins all have relative errors less than 0.10 with no zero bins

the 10 statistical checks are only for the tally fluctuation chart bin and do not apply to other tally bins.

1tally fluctuation charts

	tally 14					tally 16				
nps	mean	error	vov	slope	fom	mean	error	vov	slope	fom
8000	4.0439E-03	0.0084	0.0017	10.0	2817486	9.4979E-06	0.0078	0.0022	10.0	3307360
16000	4.0269E-03	0.0059	0.0008	10.0	2853801	9.4593E-06	0.0054	0.0011	10.0	3380634
24000	3.9979E-03	0.0048	0.0006	10.0	2910696	9.3926E-06	0.0044	0.0007	10.0	3466736
32000	3.9980E-03	0.0042	0.0004	10.0	2892825	9.3930E-06	0.0038	0.0005	10.0	3449289
40000	3.9924E-03	0.0037	0.0003	10.0	2898709	9.3814E-06	0.0034	0.0004	10.0	3461969
48000	3.9839E-03	0.0034	0.0003	10.0	2897788	9.3639E-06	0.0031	0.0004	10.0	3455642
56000	3.9811E-03	0.0031	0.0003	10.0	2900041	9.3583E-06	0.0029	0.0003	10.0	3460406
64000	3.9901E-03	0.0029	0.0002	10.0	2895697	9.3771E-06	0.0027	0.0003	10.0	3460384
72000	3.9829E-03	0.0028	0.0002	10.0	2914746	9.3610E-06	0.0025	0.0002	10.0	3483988
80000	3.9857E-03	0.0026	0.0002	10.0	2914481	9.3648E-06	0.0024	0.0002	10.0	3492919
88000	3.9868E-03	0.0025	0.0002	10.0	2910851	9.3659E-06	0.0023	0.0002	10.0	3494097
96000	3.9866E-03	0.0024	0.0001	10.0	2911094	9.3653E-06	0.0022	0.0002	10.0	3493433
104000	3.9865E-03	0.0023	0.0001	10.0	2897698	9.3646E-06	0.0021	0.0002	10.0	3478046
112000	3.9907E-03	0.0022	0.0001	10.0	2891644	9.3737E-06	0.0020	0.0002	10.0	3468398
120000	3.9913E-03	0.0022	0.0001	10.0	2893811	9.3762E-06	0.0020	0.0001	10.0	3464632
128000	3.9883E-03	0.0021	0.0001	10.0	2898569	9.3698E-06	0.0019	0.0001	10.0	3471951
136000	3.9894E-03	0.0020	0.0001	10.0	2898623	9.3728E-06	0.0018	0.0001	10.0	3468225
144000	3.9884E-03	0.0020	0.0001	10.0	2895763	9.3705E-06	0.0018	0.0001	10.0	3466658
150000	3.9878E-03	0.0019	0.0001	10.0	2903393	9.3690E-06	0.0018	0.0001	10.0	3478314

****

dump no.   2 on file runtpf   nps =   150000   coll =   500228   ctm =   0.09   nrn =
8412307

run terminated when   150000 particle histories were done.

computer time =   0.10 minutes

mcnp   version 5   01232009   02/02/11 17:06:00   probid = 02/02/11 17:05:54

Detailed model – Sample input file:

```
c Gamma ray beam source with Au in tumor and diffusion around the tumor site.
c Cells directly adjacent to tumor have a ___:1 tumor:tissue ratio for Au
c diffusion.  [Varied for specificity dependence]
c
c Input simulates gamma ray source 2 cm left of origin
c Gamma ray source strength = 0.25 MeV
c Au concentration in tissue = -- [Varied for concentration dependence]
c Last edited on: Monday, February 21, 2011
c
c ---------------------  Cells, regions definition --------------------------
c The source is assumed to be planar, aimed at the left edge of the tissue.
c Target cells are defined as 1 cm slabs orthogonal to the source plane.  Tumor
c is defined as a 1 cm thick slab at a depth of 4.50 cm.
c
c Density: Skin tissue               m1 =  1.09   g/cm3 [ICRU 46]
c          Healthy tissue            m2 =  1.0700 g/cm3
c
c          "Tumor" with 0.70% Au     m3 =  1.3491 g/cm3
c          Tissue with 3.5:1 ratio   m4 =  1.1497 g/cm3
c          Tissue with 8.5:1 ratio   m5 =  1.1028 g/cm3
c
c          "Tumor" with 1.20% Au     m6 =  1.5752 g/cm3
c          Tissue with 3.5:1 ratio   m7 =  1.2144 g/cm3
c          Tissue with 8.5:1 ratio   m8 =  1.1294 g/cm3
c
c          "Tumor" with 3.000% Au    m9 =  1.7996 g/cm3
c          Tissue with 3.5:1 ratio   m10=  1.2785 g/cm3
c          Tissue with 8.5:1 ratio   m11=  1.1558 g/cm3
c
   1  0          -1  -2      $ Vacuum behind source plane
   2  0          -1   2  -3  $ Source on the left edge of cell
   3  1  -1.09   -1   3  -4  $ Skin layer
   4  2  -1.07   -1   4  -5  $ Healthy tissue
   5  2  -1.07   -1   5  -6  $ Healthy tissue
   6  2  -1.07   -1   6  -7  $ Healthy tissue
   7  2  -1.07   -1   7  -8  $ Healthy tissue
   8  2  -1.07   -1   8  -9  $ Tumor tissue [Concentration reduced
   9  2  -1.07   -1   9  -10 $ Tumor tissue  in center to account for
  10  2  -1.07   -1  10  -11 $ Tumor tissue  penetration dependence]
  11  2  -1.07   -1  11  -12 $ Tumor tissue
  12  2  -1.07   -1  12  -13 $ Healthy tissue
  13  2  -1.07   -1  13  -14 $ Healthy tissue
  14  2  -1.07   -1  14  -15 $ Healthy tissue
  15  2  -1.07   -1  15  -16 $ Healthy tissue
  16  2  -1.07   -1  16      $ Healthy tissue
  17  0          1           $ Vacuum outside problem boundary [outside box]

c ----------------------       Surfaces / Bodies    ----------------------
  1  RPP -5.0 5.0  -2.001 10.0  -5.0 5.0  $ Box macro-body, L=W=H=20
  2  py  -2.0                             $ Surface plane
  3  py   0.0                             $ Slices in the y-plane
  4  py   0.5                             $
  5  py   1.5                             $
  6  py   2.5                             $
  7  py   3.5                             $
  8  py   4.5                             $
  9  py   4.75                            $ Tumor sliced into four 0.25 cm
 10  py   5.00                            $ slabs for better spatial resolution
 11  py   5.25                            $
```

```
 12  py   5.50                          $
 13  py   6.5                           $
 14  py   7.5                           $
 15  py   8.5                           $
 16  py   9.5                           $

c ----------------------     Problem definition     ---------------------------
c         1 2 3 4 5 6 7 8 9 0              $ Cell numbering
  imp:p,e 0 1 1 1 1 1 1 1 1 1 &
          1 1 1 1 1 1 0                    $ Photons disappear at boundary
  mode p e                                 $ Photon transport
  nps 150000                               $ Number of histories
c
c ----------------------    Source definition     ----------------------------
  sdef par = 2            $ Photon source
       erg = 0.25         $ Energy level [MeV]
       sur = 2            $ Source points sampled over surface 2 at y = -2
       vec = 0 1 0        $ Reference vector (Source in +y direction)
       dir = 1            $ Cos of angle between vec and beam vector
       pos = 0 -2 0       $ Center of sampling range (0,-2,0)
       rad = d1           $ Beam width distribution
  SI1 0 5                 $ Source sampled over r=0 to r=5
  SP1 -21 1               $ Power rule with a=1 (Constant sampling)
c
c ----------------------    Response functions    ----------------------------
  f6:p    3  4  5  6  7  8  9  10  11  12  13  14  15  16       $ Heating number approx.
[MeV/g]
  *f8:p  3 4 5 6 7 8 9 10 11 12 13 14 15 16     $ Modified pulse height  [MeV]
c
c ----------------------    Materials             ----------------------------
c Composition of bodily materials
c
c Skin tissue
  m1    1000.04p       -0.100
        6000.04p       -0.204
        7000.04p       -0.042
        8000.04p       -0.645
       11000.04p       -0.002
       15000.04p       -0.001
       16000.04p       -0.002
       17000.04p       -0.003
       19000.04p       -0.001
c
c Healthy tissue
  m2    1000.04p       -0.1020
        6000.04p       -0.1430
        7000.04p       -0.0340
        8000.04p       -0.7100
       11000.04p       -0.0010
       15000.04p       -0.0020
       16000.04p       -0.0030
       17000.04p       -0.0010
       19000.04p       -0.0040
c ---------------------------------------------------------------------------
c Material for 1.53% Au with diffusion
c ---------------------------------------------------------------------------
c "Tumor" layer Au
  m3    1000.04p       -0.1004
        6000.04p       -0.1408
        7000.04p       -0.0335
        8000.04p       -0.6991
       11000.04p       -0.0010
       15000.04p       -0.0020
```

```
       16000.04p       -0.0030
       17000.04p       -0.0010
       19000.04p       -0.0039
       79000.04p       -0.0153        $ 1.53 % mass fraction of gold
c
c Tissue with diffused Au at 3.5:1 ratio
  m4    1000.04p       -0.1016
        6000.04p       -0.1424
        7000.04p       -0.0339
        8000.04p       -0.7067
       11000.04p       -0.0010
       15000.04p       -0.0020
       16000.04p       -0.0030
       17000.04p       -0.0010
       19000.04p       -0.0040
       79000.04p       -0.0044        $ 0.44 % mass fraction of gold
c
c Tissue with diffused Au at 8.5:1 ratio
  m5    1000.04p       -0.1018
        6000.04p       -0.1427
        7000.04p       -0.0339
        8000.04p       -0.7088
       11000.04p       -0.0010
       15000.04p       -0.0020
       16000.04p       -0.0030
       17000.04p       -0.0010
       19000.04p       -0.0040
       79000.04p       -0.0018        $ 0.18 % mass fraction of gold
c ---------------------------------------------------------------------------
c Material for 2.77% Au with diffusion
c ---------------------------------------------------------------------------
c "Tumor" layer Au
  m6    1000.04p       -0.0992
        6000.04p       -0.1390
        7000.04p       -0.0331
        8000.04p       -0.6902
       11000.04p       -0.0010
       15000.04p       -0.0019
       16000.04p       -0.0029
       17000.04p       -0.0010
       19000.04p       -0.0039
       79000.04p       -0.0277        $ 2.77 % mass fraction of gold
c
c Tissue with diffused Au at 3.5:1 ratio
  m7    1000.04p       -0.1012
        6000.04p       -0.1419
        7000.04p       -0.0337
        8000.04p       -0.7043
       11000.04p       -0.0010
       15000.04p       -0.0020
       16000.04p       -0.0030
       17000.04p       -0.0010
       19000.04p       -0.0040
       79000.04p       -0.0079        $ 0.79 % mass fraction of gold
c
c Tissue with diffused Au at 8.5:1 ratio
  m8    1000.04p       -0.1017
        6000.04p       -0.1425
        7000.04p       -0.0339
        8000.04p       -0.7076
       11000.04p       -0.0010
       15000.04p       -0.0020
       16000.04p       -0.0030
```

```
       17000.04p       -0.0010
       19000.04p       -0.0040
       79000.04p       -0.0033        $ 0.33 % mass fraction of gold
c ---------------------------------------------------------------------------
c Material for 4.00% Au with diffusion
c ---------------------------------------------------------------------------
c "Tumor" layer Au
  m9    1000.04p       -0.0979
        6000.04p       -0.1373
        7000.04p       -0.0326
        8000.04p       -0.6816
       11000.04p       -0.0010
       15000.04p       -0.0019
       16000.04p       -0.0029
       17000.04p       -0.0010
       19000.04p       -0.0038
       79000.04p       -0.0400        $ 4.00 % mass fraction of gold
c
c Tissue with diffused Au at 3.5:1 ratio
  m10   1000.04p       -0.1008
        6000.04p       -0.1414
        7000.04p       -0.0336
        8000.04p       -0.7018
       11000.04p       -0.0010
       15000.04p       -0.0020
       16000.04p       -0.0030

       17000.04p       -0.0010
       19000.04p       -0.0040
       79000.04p       -0.0114        $ 1.14 % mass fraction of gold
c
c Tissue with diffused Au at 8.5:1 ratio
  m11   1000.04p       -0.1015
        6000.04p       -0.1423
        7000.04p       -0.0338
        8000.04p       -0.7067
       11000.04p       -0.0010
       15000.04p       -0.0020
       16000.04p       -0.0030
       17000.04p       -0.0010
       19000.04p       -0.0040
       79000.04p       -0.0047        $ 0.47 % mass fraction of gold
```

Detailed model – Sample output file

```
         Thread Name & Version = MCNP5_RSICC, 1.51

                                  _
            ._ _    _  ._   ._   |_
            | | |  (_  | |  |_)   _)
                                 |

  +---------------------------------------------------------------------+
  | Copyright 2008. Los Alamos National Security, LLC.  All rights      |
  | reserved.                                                           |
  |   This material was produced under U.S. Government contract         |
  | DE-AC52-06NA25396 for Los Alamos National Laboratory, which is      |
  | operated by Los Alamos National Security, LLC, for the U.S.         |
  | Department of Los Energy. The Government is granted for itself and  |
  | others acting on its behalf a paid-up, nonexclusive, irrevocable    |
  | worldwide license in this material to reproduce, prepare derivative |
  | works, and perform publicly and display publicly. Beginning five    |
  | (5) years after 2008, subject to additional five-year worldwide     |
  | renewals, the Government is granted for itself and others acting on |
  | its behalf a paid-up, nonexclusive, irrevocable worldwide license   |
  | in this material to reproduce, prepare derivative works, distribute |
  | copies to the public, perform publicly and display publicly, and to |
  | permit others to do so. NEITHER THE UNITED STATES NOR THE UNITED    |
  | STATES DEPARTMENT OF ENERGY, NOR LOS ALAMOS NATIONAL SECURITY, LLC, |
  | NOR ANY OF THEIR EMPLOYEES, MAKES ANY WARRANTY, EXPRESS OR IMPLIED, |
  | OR ASSUMES ANY LEGAL LIABILITY OR RESPONSIBILITY FOR THE ACCURACY,  |
  | COMPLETENESS, OR USEFULNESS OF ANY INFORMATION, APPARATUS, PRODUCT, |
  | OR PROCESS DISCLOSED, OR REPRESENTS THAT ITS USE WOULD NOT INFRINGE |
  | PRIVATELY OWNED RIGHTS.                                             |
  +---------------------------------------------------------------------+

1mcnp     version 5     ld=01232009                    03/30/11 11:15:46
 ***********************************************************************                  probid =  03/30/11 11:15:46
 i=025B.txt o=025A0.txt

      1-       c Gamma ray beam source with Au in tumor and diffusion around the tumor site.
      2-       c Cells directly adjacent to tumor have a ___:1 tumor:tissue ratio for Au
      3-       c diffusion.
      4-       c
      5-       c Input simulates gamma ray source 2 cm left of origin
      6-       c Gamma ray source strength = 0.25 MeV
      7-       c Au concentration in tissue = --
      8-       c Last edited on: Monday, February 21, 2011
      9-       c
     10-       c ----------------------  Cells, regions definition ----------------------------
```

```
c The source is assumed to be planar, aimed at the left edge of the tissue.
c Target cells are defined as 1 cm slabs orthogonal to the source plane.  Tumor
c is defined as a 1 cm thick slab at a depth of 4.50 cm.
c
c Density: Skin tissue               m1 =  1.09   g/cm3 [ICRU 46]
c          Healthy tissue            m2 =  1.0700 g/cm3
c
c          "Tumor" with 1.53% Au     m3 =  1.3491 g/cm3
c          Tissue with 3.5:1 ratio   m4 =  1.1497 g/cm3
c          Tissue with 8.5:1 ratio   m5 =  1.1028 g/cm3
c
c          "Tumor" with 2.77% Au     m6 =  1.5752 g/cm3
c          Tissue with 3.5:1 ratio   m7 =  1.2144 g/cm3
c          Tissue with 8.5:1 ratio   m8 =  1.1294 g/cm3
c
c          "Tumor" with 4.00% Au     m9 =  1.7996 g/cm3
c          Tissue with 3.5:1 ratio   m10=  1.2785 g/cm3
c          Tissue with 8.5:1 ratio   m11=  1.1558 g/cm3
c
   1  0          -1  -2      $ Vacuum behind source plane
   2  0          -1   2  -3  $ Source on the left edge of cell
   3  1  -1.09   -1   3  -4  $ Skin layer
   4  2  -1.07   -1   4  -5  $ Healthy tissue
   5  2  -1.07   -1   5  -6  $ Healthy tissue
   6  2  -1.07   -1   6  -7  $ Healthy tissue
   7  2  -1.07   -1   7  -8  $ Healthy tissue
   8  2  -1.07   -1   8  -9  $ Tumor
   9  2  -1.07   -1   9  -10 $ Tumor
  10  2  -1.07   -1  10  -11 $ Tumor
  11  2  -1.07   -1  11  -12 $ Tumor
  12  2  -1.07   -1  12  -13 $ Healthy tissue
  13  2  -1.07   -1  13  -14 $ Healthy tissue
  14  2  -1.07   -1  14  -15 $ Healthy tissue
  15  2  -1.07   -1  15  -16 $ Healthy tissue
  16  2  -1.07   -1  16      $ Healthy tissue
  17  0          1           $ Vacuum outside problem boundary [outside box]

c ----------------------       Surfaces / Bodies    ----------------------
  1  RPP -5.0 5.0  -2.001 10.0  -5.0 5.0  $ Box macro-body, L=W=H=20
  2  py  -2.0                             $ Surface plane
  3  py   0.0                             $ Slices in the y-plane
  4  py   0.5                             $
  5  py   1.5                             $
  6  py   2.5                             $
  7  py   3.5                             $
  8  py   4.5                             $
```

```
 57-         9  py   4.75                          $
 58-        10  py   5.00                          $
 59-        11  py   5.25                          $
 60-        12  py   5.50                          $
 61-        13  py   6.5                           $
 62-        14  py   7.5                           $
 63-        15  py   8.5                           $
 64-        16  py   9.5                           $
 65-
 66-       c ----------------------     Problem definition     ----------------------------
 67-       c         1 2 3 4 5 6 7 8 9 0             $ Cell numbering
 68-         imp:p,e 0 1 1 1 1 1 1 1 1 1 &
 69-                 1 1 1 1 1 1 0                   $ Photons disappear at boundary
 70-         mode p e                                $ Photon transport
 71-         nps 150000                              $ Number of histories
 72-       c
 73-       c ----------------------    Source definition     ------------------------------
 74-         sdef par = 2            $ Photon source
 75-              erg = 0.25         $ Energy level [MeV]
 76-              sur = 2            $ Source points sampled over surface 2 at y = -2
 77-              vec = 0 1 0        $ Reference vector (Source in +y direction)
 78-              dir = 1            $ Cos of angle between vec and beam vector
 79-              pos = 0 -2 0       $ Center of sampling range (0,-2,0)
 80-              rad = d1           $ Beam width distribution
 81-         SI1 0 5                 $ Source sampled over r=0 to r=5
 82-         SP1 -21 1               $ Power rule with a=1 (Constant sampling)
 83-       c
 84-       c ----------------------    Response functions    ------------------------------
 85-         f6:p   3 4 5 6 7 8 9 10 11 12 13 14 15 16     $ Heating number approx. [MeV/g]
 86-         *f8:p  3 4 5 6 7 8 9 10 11 12 13 14 15 16     $ Modified pulse height  [MeV]
 87-       c
 88-       c ----------------------    Materials             ------------------------------
 89-       c Composition of bodily materials
 90-       c
 91-       c Skin tissue
 92-         m1    1000.04p       -0.100
 93-               6000.04p       -0.204
 94-               7000.04p       -0.042
 95-               8000.04p       -0.645
 96-              11000.04p       -0.002
 97-              15000.04p       -0.001
 98-              16000.04p       -0.002
 99-              17000.04p       -0.003
100-              19000.04p       -0.001
101-       c
102-       c Healthy tissue
```

```
  103-         m2    1000.04p       -0.1020
  104-               6000.04p       -0.1430
  105-               7000.04p       -0.0340
  106-               8000.04p       -0.7100
  107-              11000.04p       -0.0010
  108-              15000.04p       -0.0020
  109-              16000.04p       -0.0030
  110-              17000.04p       -0.0010
  111-              19000.04p       -0.0040
  112-       c ---------------------------------------------------------------------------
  113-       c Material for 1.53% Au with diffusion
  114-       c ---------------------------------------------------------------------------
  115-       c "Tumor" layer Au
  116-         m3    1000.04p       -0.1004
warning.  material   3 is not used in the problem.
  117-               6000.04p       -0.1408
  118-               7000.04p       -0.0335
  119-               8000.04p       -0.6991
  120-              11000.04p       -0.0010
  121-              15000.04p       -0.0020
  122-              16000.04p       -0.0030
  123-              17000.04p       -0.0010
  124-              19000.04p       -0.0039
  125-              79000.04p       -0.0153        $ 1.53 % mass fraction of gold
  126-       c
  127-       c Tissue with diffused Au at 3.5:1 ratio
  128-         m4    1000.04p       -0.1016
warning.  material   4 is not used in the problem.
  129-               6000.04p       -0.1424
  130-               7000.04p       -0.0339
  131-               8000.04p       -0.7067
  132-              11000.04p       -0.0010
  133-              15000.04p       -0.0020
  134-              16000.04p       -0.0030
  135-              17000.04p       -0.0010
  136-              19000.04p       -0.0040
  137-              79000.04p       -0.0044        $ 0.44 % mass fraction of gold
  138-       c
  139-       c Tissue with diffused Au at 8.5:1 ratio
  140-         m5    1000.04p       -0.1018
warning.  material   5 is not used in the problem.
  141-               6000.04p       -0.1427
  142-               7000.04p       -0.0339
  143-               8000.04p       -0.7088
  144-              11000.04p       -0.0010
  145-              15000.04p       -0.0020
```

```
  146-              16000.04p       -0.0030
  147-              17000.04p       -0.0010
  148-              19000.04p       -0.0040
  149-              79000.04p       -0.0018        $ 0.18 % mass fraction of gold
  150-       c ---------------------------------------------------------------------------
  151-       c Material for 2.77% Au with diffusion
  152-       c ---------------------------------------------------------------------------
  153-       c "Tumor" layer Au
  154-         m6    1000.04p       -0.0992
warning.  material   6 is not used in the problem.
  155-              6000.04p       -0.1390
  156-              7000.04p       -0.0331
  157-              8000.04p       -0.6902
  158-             11000.04p       -0.0010
  159-             15000.04p       -0.0019
  160-             16000.04p       -0.0029
  161-             17000.04p       -0.0010
  162-             19000.04p       -0.0039
  163-             79000.04p       -0.0277        $ 1.20 % mass fraction of gold
  164-       c
  165-       c Tissue with diffused Au at 3.5:1 ratio
  166-         m7    1000.04p       -0.1012
warning.  material   7 is not used in the problem.
  167-              6000.04p       -0.1419
  168-              7000.04p       -0.0337
  169-              8000.04p       -0.7043
  170-             11000.04p       -0.0010
  171-             15000.04p       -0.0020
  172-             16000.04p       -0.0030
  173-             17000.04p       -0.0010
  174-             19000.04p       -0.0040
  175-             79000.04p       -0.0079        $ 0.79 % mass fraction of gold
  176-       c
  177-       c Tissue with diffused Au at 8.5:1 ratio
  178-         m8    1000.04p       -0.1017
warning.  material   8 is not used in the problem.
  179-              6000.04p       -0.1425
  180-              7000.04p       -0.0339
  181-              8000.04p       -0.7076
  182-             11000.04p       -0.0010
  183-             15000.04p       -0.0020
  184-             16000.04p       -0.0030
  185-             17000.04p       -0.0010
  186-             19000.04p       -0.0040
  187-             79000.04p       -0.0033        $ 0.3 % mass fraction of gold
  188-       c ---------------------------------------------------------------------------
```

```
    189-       c Material for 4.00% Au with diffusion
    190-       c ---------------------------------------------------------------------------
    191-       c "Tumor" layer Au
    192-         m9    1000.04p       -0.0979
  warning.  material   9 is not used in the problem.
    193-               6000.04p       -0.1373
    194-               7000.04p       -0.0326
    195-               8000.04p       -0.6816
    196-              11000.04p       -0.0010
    197-              15000.04p       -0.0019
    198-              16000.04p       -0.0029
    199-              17000.04p       -0.0010
    200-              19000.04p       -0.0038
    201-              79000.04p       -0.0400        $ 4.00 % mass fraction of gold
    202-       c
    203-       c Tissue with diffused Au at 3.5:1 ratio
    204-         m10   1000.04p       -0.1008
  warning.  material  10 is not used in the problem.
    205-               6000.04p       -0.1414
    206-               7000.04p       -0.0336
    207-               8000.04p       -0.7018
    208-              11000.04p       -0.0010
    209-              15000.04p       -0.0020
    210-              16000.04p       -0.0030
    211-              17000.04p       -0.0010
    212-              19000.04p       -0.0040
    213-              79000.04p       -0.0114        $ 1.14 % mass fraction of gold
    214-       c
    215-       c Tissue with diffused Au at 8.5:1 ratio
    216-         m11   1000.04p       -0.1015
  warning.  material  11 is not used in the problem.
    217-               6000.04p       -0.1423
    218-               7000.04p       -0.0338
    219-               8000.04p       -0.7067
    220-              11000.04p       -0.0010
    221-              15000.04p       -0.0020
    222-              16000.04p       -0.0030
    223-              17000.04p       -0.0010
    224-              19000.04p       -0.0040
    225-              79000.04p       -0.0047        $ 0.47 % mass fraction of gold
1cells                                                                          print table 60

                     atom        gram                                      photon     electron
        cell  mat    density     density     volume       mass     pieces importance importance

         1     1    0  0.00000E+00 0.00000E+00 1.00000E-01 0.00000E+00     0  0.0000E+00 0.0000E+00
```

```
     2     2    0  0.00000E+00 0.00000E+00 2.00000E+02 0.00000E+00     0  1.0000E+00 1.0000E+00
     3     3    1  1.04892E-01 1.09000E+00 5.00000E+01 5.45000E+01     0  1.0000E+00 1.0000E+00
     4     4    2  1.03249E-01 1.07000E+00 1.00000E+02 1.07000E+02     0  1.0000E+00 1.0000E+00
     5     5    2  1.03249E-01 1.07000E+00 1.00000E+02 1.07000E+02     0  1.0000E+00 1.0000E+00
     6     6    2  1.03249E-01 1.07000E+00 1.00000E+02 1.07000E+02     0  1.0000E+00 1.0000E+00
     7     7    2  1.03249E-01 1.07000E+00 1.00000E+02 1.07000E+02     0  1.0000E+00 1.0000E+00
     8     8    2  1.03249E-01 1.07000E+00 2.50000E+01 2.67500E+01     0  1.0000E+00 1.0000E+00
     9     9    2  1.03249E-01 1.07000E+00 2.50000E+01 2.67500E+01     0  1.0000E+00 1.0000E+00
    10    10    2  1.03249E-01 1.07000E+00 2.50000E+01 2.67500E+01     0  1.0000E+00 1.0000E+00
    11    11    2  1.03249E-01 1.07000E+00 2.50000E+01 2.67500E+01     0  1.0000E+00 1.0000E+00
    12    12    2  1.03249E-01 1.07000E+00 1.00000E+02 1.07000E+02     0  1.0000E+00 1.0000E+00
    13    13    2  1.03249E-01 1.07000E+00 1.00000E+02 1.07000E+02     0  1.0000E+00 1.0000E+00
    14    14    2  1.03249E-01 1.07000E+00 1.00000E+02 1.07000E+02     0  1.0000E+00 1.0000E+00
    15    15    2  1.03249E-01 1.07000E+00 1.00000E+02 1.07000E+02     0  1.0000E+00 1.0000E+00
    16    16    2  1.03249E-01 1.07000E+00 5.00000E+01 5.35000E+01     0  1.0000E+00 1.0000E+00
    17    17    0  0.00000E+00 0.00000E+00 0.00000E+00 0.00000E+00     0  0.0000E+00 0.0000E+00

 total                                    1.20010E+03 1.07100E+03

    minimum source weight = 1.0000E+00    maximum source weight = 1.0000E+00

 ************************************************
 * Random Number Generator  =                   1 *
 * Random Number Seed       =       19073486328125 *
 * Random Number Multiplier =       19073486328125 *
 * Random Number Adder      =                   0 *
 * Random Number Bits Used  =                  48 *
 * Random Number Stride     =              152917 *
 ************************************************


         9 warning messages so far.
1cross-section tables                                                                    print table 100

     table    length

                        tables from file mcplib04

   1000.04p    1898  ENDF/B-VI Release 8 Photoatomic Data for 1-H                        mat 100      02/07/03
   6000.04p    3152  ENDF/B-VI Release 8 Photoatomic Data for 6-C                        mat 600      02/07/03
   7000.04p    3194  ENDF/B-VI Release 8 Photoatomic Data for 7-N                        mat 700      02/07/03
   8000.04p    3272  ENDF/B-VI Release 8 Photoatomic Data for 8-O                        mat 800      02/07/03
  11000.04p    3995  ENDF/B-VI Release 8 Photoatomic Data for 11-NA                      mat1100      02/07/03
  15000.04p    4498  ENDF/B-VI Release 8 Photoatomic Data for 15-P                       mat1500      02/07/03
  16000.04p    4654  ENDF/B-VI Release 8 Photoatomic Data for 16-S                       mat1600      02/07/03
  17000.04p    4738  ENDF/B-VI Release 8 Photoatomic Data for 17-CL                      mat1700      02/07/03
```

```
 19000.04p    5047  ENDF/B-VI Release 8 Photoatomic Data for 19-K                                  mat1900      02/07/03

 total       34448

maximum photon energy set to  100.0 mev (maximum electron energy)

                      tables from file el03

  1000.03e    2329                                                                                          6/6/98
  6000.03e    2333                                                                                          6/6/98
  7000.03e    2333                                                                                          6/6/98
  8000.03e    2333                                                                                          6/6/98
 11000.03e    2337                                                                                          6/6/98
 15000.03e    2339                                                                                          6/6/98
 16000.03e    2339                                                                                          6/6/98
 17000.03e    2339                                                                                          6/6/98
 19000.03e    2343                                                                                          6/6/98

************************************************************************************************************************

 dump no.    1 on file runtpe     nps =           0     coll =             0     ctm =        0.00   nrn =
    0

         9 warning messages so far.
1problem summary

      run terminated when      150000  particle histories were done.
+                                                                                          03/30/11 11:16:31
      c Gamma ray beam source with Au in tumor and diffusion around the tumor site.        probid =  03/30/11 11:15:46
0
 photon creation     tracks      weight        energy           photon loss         tracks      weight        energy
                                 (per source particle)                                        (per source particle)

 source              150000    1.0000E+00    2.5000E-01         escape              148709    9.9139E-01    1.8342E-01
                                                                 energy cutoff            0    0.            1.8583E-06
                                                                 time cutoff              0    0.            0.
 weight window            0    0.            0.                 weight window            0    0.            0.
 cell importance          0    0.            0.                 cell importance          0    0.            0.
 weight cutoff            0    0.            0.                 weight cutoff            0    0.            0.
 e or t importance        0    0.            0.                 e or t importance        0    0.            0.
 dxtran                   0    0.            0.                 dxtran                   0    0.            0.
 forced collisions        0    0.            0.                 forced collisions        0    0.            0.
 exp. transform           0    0.            0.                 exp. transform           0    0.            0.
 from neutrons            0    0.            0.                 compton scatter          0    0.            6.5605E-02
 bremsstrahlung         652    4.3467E-03    3.7355E-05         capture               1958    1.3053E-02    1.0114E-03
 p-annihilation           0    0.            0.                 pair production          0    0.            0.
```

```
 photonuclear              0    0.            0.                  photonuclear abs         0    0.            0.
 electron x-rays          13    8.6667E-05    2.8667E-07
 1st fluorescence          2    1.3333E-05    3.9441E-08
 2nd fluorescence          0    0.            0.
     total            150667    1.0044E+00    2.5004E-01              total           150667    1.0044E+00    2.5004E-01

   number of photons banked                      665        average time of (shakes)              cutoffs
   photon tracks per source particle       1.0044E+00          escape            4.0286E-02          tco   1.0000E+33
   photon collisions per source particle   1.4191E+00          capture           4.1428E-02          eco   1.0000E-03
   total photon collisions                    212860          capture or escape 4.0300E-02          wc1  -5.0000E-01
                                                              any termination   4.0300E-02          wc2  -2.5000E-01
0
 electron creation   tracks      weight        energy            electron loss       tracks      weight        energy
                                 (per source particle)                                           (per source particle)

 source                    0    0.            0.                  escape                  65    4.3333E-04    2.4454E-05
                                                                    energy cutoff       958342    6.3889E+00    6.2486E-03
                                                                    time cutoff              0    0.            0.
 weight window             0    0.            0.                  weight window            0    0.            0.
 cell importance           0    0.            0.                  cell importance          0    0.            0.
 weight cutoff             0    0.            0.                  weight cutoff            0    0.            0.
 e or t importance         0    0.            0.                  e or t importance        0    0.            0.
 pair production           0    0.            0.                  scattering               0    0.            7.3625E-02
 compton recoil       203955    1.3597E+00    6.5591E-02          bremsstrahlung           0    0.            3.7355E-05
 photo-electric         1957    1.3047E-02    1.0107E-03          p-annihilation           0    0.            0.
 photon auger             27    1.8000E-04    6.4926E-07
 electron auger          112    7.4667E-04    2.6932E-06
 knock-on             752356    5.0157E+00    1.3330E-02
     total            958407    6.3894E+00    7.9935E-02              total           958407    6.3894E+00    7.9935E-02

   number of electrons banked                    958407                                              cutoffs
   electron tracks per source particle      6.3894E+00                                                tco   1.0000E+33
   electron sub-steps per source particle   3.3061E+02                                                eco   1.0000E-03
   total electron sub-steps                  49591400                                                 wc1   0.0000E+00
                                                                                                      wc2   0.0000E+00

 computer time so far in this run      0.74 minutes          maximum number ever in bank        30
 computer time in mcrun                0.73 minutes          bank overflows to backup file       0
 source particles per minute             2.0573E+05
 random numbers generated                 318764386          most random numbers used was       12476 in history       43510

 range of sampled source weights = 1.0000E+00 to 1.0000E+00
1photon   activity in each cell                                                                        print table 126

                tracks     population   collisions   collisions     number        flux        average      average
        cell    entering                             * weight     weighted     weighted   track weight   track mfp
```

					(per history)	energy	energy	(relative)	(cm)
2	2	170068	150006	0	0.0000E+00	2.3255E-01	2.3255E-01	1.0000E+00	0.0000E+00
3	3	169729	150043	13863	9.2420E-02	2.2311E-01	2.2311E-01	1.0000E+00	6.9987E+00
4	4	165504	146237	28015	1.8677E-01	2.1797E-01	2.1797E-01	1.0000E+00	7.0488E+00
5	5	156166	137569	27097	1.8065E-01	2.1396E-01	2.1396E-01	1.0000E+00	6.9984E+00
6	6	145582	128234	25687	1.7125E-01	2.1123E-01	2.1123E-01	1.0000E+00	6.9642E+00
7	7	133931	118535	23887	1.5925E-01	2.0948E-01	2.0948E-01	1.0000E+00	6.9421E+00
8	8	123458	108556	5641	3.7607E-02	2.0872E-01	2.0872E-01	1.0000E+00	6.9314E+00
9	9	120612	106136	5521	3.6807E-02	2.0839E-01	2.0839E-01	1.0000E+00	6.9264E+00
10	10	117745	103788	5496	3.6640E-02	2.0797E-01	2.0797E-01	1.0000E+00	6.9215E+00
11	11	114839	101456	5250	3.5000E-02	2.0800E-01	2.0800E-01	1.0000E+00	6.9219E+00
12	12	110395	99145	19828	1.3219E-01	2.0775E-01	2.0775E-01	1.0000E+00	6.9182E+00
13	13	98576	89854	17638	1.1759E-01	2.0863E-01	2.0863E-01	1.0000E+00	6.9307E+00
14	14	87248	81298	15709	1.0473E-01	2.1004E-01	2.1004E-01	1.0000E+00	6.9498E+00
15	15	75835	73172	13528	9.0187E-02	2.1340E-01	2.1340E-01	1.0000E+00	6.9928E+00
16	16	66025	65716	5700	3.8000E-02	2.1875E-01	2.1875E-01	1.0000E+00	7.0608E+00
total		1855713	1659745	212860	1.4191E+00				

1electron activity in each cell print table 126

cell	tracks entering	population	substeps	substeps * weight (per history)	number weighted energy	flux weighted energy	average track weight (relative)	average track mfp (cm)
2	10	10	0	0.0000E+00	1.7894E-02	2.8085E-02	1.0000E+00	0.0000E+00
3	19	66208	3402351	2.2682E+01	4.5820E-02	5.7839E-02	1.0000E+00	3.0481E-04
4	79	132084	6787527	4.5250E+01	4.5271E-02	5.7392E-02	1.0000E+00	3.0808E-04
5	81	123253	6368821	4.2459E+01	4.4590E-02	5.6655E-02	1.0000E+00	3.0195E-04
6	77	114119	5920258	3.9468E+01	4.3890E-02	5.5884E-02	1.0000E+00	2.9565E-04
7	75	106025	5481105	3.6541E+01	4.4290E-02	5.6515E-02	1.0000E+00	3.0237E-04
8	77	24960	1289750	8.5983E+00	4.3836E-02	5.5667E-02	1.0000E+00	2.9297E-04
9	90	24029	1256744	8.3783E+00	4.3577E-02	5.5658E-02	1.0000E+00	2.9503E-04
10	70	23618	1228120	8.1875E+00	4.2763E-02	5.4303E-02	1.0000E+00	2.8063E-04
11	77	23032	1193667	7.9578E+00	4.3756E-02	5.5605E-02	1.0000E+00	2.9203E-04
12	63	86846	4513883	3.0093E+01	4.3622E-02	5.5670E-02	1.0000E+00	2.9458E-04
13	56	77346	4017562	2.6784E+01	4.3364E-02	5.5240E-02	1.0000E+00	2.9025E-04
14	50	69668	3608070	2.4054E+01	4.3672E-02	5.5650E-02	1.0000E+00	2.9388E-04
15	45	60691	3133367	2.0889E+01	4.3689E-02	5.5499E-02	1.0000E+00	2.9196E-04
16	27	27270	1390175	9.2678E+00	4.4875E-02	5.6520E-02	1.0000E+00	2.9878E-04
total	896	959159	49591400	3.3061E+02				

1tally 6 nps = 150000
tally type 6 track length estimate of heating. units mev/gram
tally for photons

```
          masses
                  cell:       3           4           5           6           7           8           9
                        5.45000E+01 1.07000E+02 1.07000E+02 1.07000E+02 1.07000E+02 2.67500E+01 2.67500E+01
                  cell:      10          11          12          13          14          15          16
                        2.67500E+01 2.67500E+01 1.07000E+02 1.07000E+02 1.07000E+02 1.07000E+02 5.35000E+01

cell  3
                8.62707E-05 0.0011

cell  4
                8.49287E-05 0.0011

cell  5
                8.04830E-05 0.0013

cell  6
                7.49356E-05 0.0015

cell  7
                6.88536E-05 0.0018

cell  8
                6.48968E-05 0.0023

cell  9
                6.33554E-05 0.0024

cell  10
                6.19342E-05 0.0024

cell  11
                6.02999E-05 0.0025

cell  12
                5.65748E-05 0.0023

cell  13
                5.06716E-05 0.0025

cell  14
                4.50454E-05 0.0028

cell  15
                3.93693E-05 0.0030
```

```
 cell  16
                3.49694E-05 0.0034


==========================================================================================================================================

           results of 10 statistical checks for the estimated answer for the tally fluctuation chart (tfc) bin of tally   6

 tfc bin     --mean--      ---------relative error---------      ----variance of the variance----      --figure of merit--     -
pdf-
 behavior    behavior      value   decrease   decrease rate      value   decrease   decrease rate       value     behavior
slope

 desired      random       <0.10      yes      1/sqrt(nps)       <0.10      yes        1/nps           constant    random
>3.00
 observed     random        0.00      yes          yes            0.00      yes         yes            constant    random
10.00
 passed?        yes          yes      yes          yes              yes      yes         yes               yes        yes
yes

==========================================================================================================================================


 this tally meets the statistical criteria used to form confidence intervals: check the tally fluctuation chart to verify.
 the results in other bins associated with this tally may not meet these statistical criteria.

 ----- estimated confidence intervals:  -----

 estimated asymmetric confidence interval(1,2,3 sigma): 8.6181E-05 to 8.6363E-05; 8.6090E-05 to 8.6453E-05; 8.5999E-05 to 8.6544E-
05
 estimated  symmetric confidence interval(1,2,3 sigma): 8.6180E-05 to 8.6362E-05; 8.6089E-05 to 8.6452E-05; 8.5998E-05 to 8.6543E-
05

1analysis of the results in the tally fluctuation chart bin (tfc) for tally   6 with nps =      150000  print table 160


 normed average tally per history  = 8.62707E-05          unnormed average tally per history  = 4.70175E-03
 estimated tally relative error    = 0.0011               estimated variance of the variance  = 0.0007
 relative error from zero tallies  = 0.0000               relative error from nonzero scores  = 0.0011

 number of nonzero history tallies =      150000          efficiency for the nonzero tallies  = 1.0000
 history number of largest  tally  =       39846          largest  unnormalized history tally = 5.63679E-02
 (largest  tally)/(average tally)  = 1.19887E+01          (largest  tally)/(avg nonzero tally)= 1.19887E+01
```

(confidence interval shift)/mean = 0.0000 shifted confidence interval center = 8.62716E-05

if the largest history score sampled so far were to occur on the next history, the tfc bin quantities would change as follows:

estimated quantities	value at nps	value at nps+1	value(nps+1)/value(nps)-1.
mean	8.62707E-05	8.62770E-05	0.000073
relative error	1.05369E-03	1.05615E-03	0.002334
variance of the variance	6.80330E-04	6.96840E-04	0.024267
shifted center	8.62716E-05	8.62716E-05	0.000000
figure of merit	1.23533E+06	1.22958E+06	-0.004651

the estimated slope of the 200 largest tallies starting at 2.57536E-02 appears to be decreasing at least exponentially.
the large score tail of the empirical history score probability density function appears to have no unsampled regions.

fom = (histories/minute)*(f(x) signal-to-noise ratio)**2 = (2.057E+05)*(2.450E+00)**2 = (2.057E+05)*(6.005E+00) = 1.235E+06

1tally 8 nps = 150000
tally type 8* energy deposition units mev
tally for photons electrons

cell 3
4.67281E-03 0.0109

cell 4
9.19588E-03 0.0078

cell 5
8.57509E-03 0.0080

cell 6
7.91361E-03 0.0083

cell 7
7.34262E-03 0.0087

cell 8
1.73419E-03 0.0175

cell 9
1.67700E-03 0.0177

cell 10
1.63365E-03 0.0178

```
 cell  11
                1.58730E-03 0.0182

 cell  12
                5.98502E-03 0.0096

 cell  13
                5.34617E-03 0.0102

 cell  14
                4.78621E-03 0.0109

 cell  15
                4.20307E-03 0.0116

 cell  16
                1.90366E-03 0.0171


================================================================================================================================

          results of 10 statistical checks for the estimated answer for the tally fluctuation chart (tfc) bin of tally   8

 tfc bin     --mean--      ---------relative error---------      ----variance of the variance----      --figure of merit--     -
pdf-
 behavior    behavior      value    decrease    decrease rate      value    decrease    decrease rate       value     behavior
slope

 desired      random       <0.10      yes      1/sqrt(nps)       <0.10      yes        1/nps           constant    random
>3.00
 observed     random        0.01      yes          yes            0.00      yes         yes            constant    random
3.35
 passed?        yes          yes      yes          yes              yes      yes         yes               yes        yes
yes


================================================================================================================================


 this tally meets the statistical criteria used to form confidence intervals: check the tally fluctuation chart to verify.
 the results in other bins associated with this tally may not meet these statistical criteria.

 ----- estimated confidence intervals:  -----

 estimated asymmetric confidence interval(1,2,3 sigma): 4.6220E-03 to 4.7242E-03; 4.5709E-03 to 4.7754E-03; 4.5198E-03 to 4.8265E-
```

```
03
 estimated  symmetric confidence interval(1,2,3 sigma): 4.6217E-03 to 4.7239E-03; 4.5706E-03 to 4.7750E-03; 4.5195E-03 to 4.8261E-
03

1analysis of the results in the tally fluctuation chart bin (tfc) for tally   8 with nps =      150000  print table 160


 normed average tally per history  = 4.67281E-03          unnormed average tally per history  = 4.67281E-03
 estimated tally relative error    = 0.0109               estimated variance of the variance  = 0.0002
 relative error from zero tallies  = 0.0000               relative error from nonzero scores  = 0.0109

 number of nonzero history tallies =      150000          efficiency for the nonzero tallies  = 1.0000
 history number of largest  tally  =        3918          largest  unnormalized history tally = 2.50000E-01
 (largest  tally)/(average tally)  = 5.35010E+01          (largest  tally)/(avg nonzero tally)= 5.35010E+01

 (confidence interval shift)/mean  = 0.0001               shifted confidence interval center  = 4.67313E-03


 if the largest  history score sampled so far were to occur on the next history, the tfc bin quantities would change as follows:

      estimated quantities           value at nps           value at nps+1          value(nps+1)/value(nps)-1.

      mean                            4.67281E-03             4.67445E-03                    0.000350
      relative error                  1.09371E-02             1.09388E-02                    0.000155
      variance of the variance        1.79152E-04             1.79808E-04                    0.003662
      shifted center                  4.67313E-03             4.67313E-03                    0.000000
      figure of merit                 1.14659E+04             1.14623E+04                   -0.000310

 the estimated inverse power slope of the 200 largest  tallies starting at 1.40587E-01 is 3.3471
 the empirical history score probability density function appears to be increasing at the largest  history scores:
 please examine. see print table 161.
 the large score tail of the empirical history score probability density function appears to have no unsampled regions.

 fom = (histories/minute)*(f(x) signal-to-noise ratio)**2 = (2.057E+05)*( 2.361E-01)**2 = (2.057E+05)*(5.573E-02) = 1.147E+04

1status of the statistical checks used to form confidence intervals for the mean for each tally bin


 tally   result of statistical checks for the tfc bin (the first check not passed is listed) and error magnitude check for all bins

     6   passed the 10 statistical checks for the tally fluctuation chart bin result
         passed all bin error check:    14 tally bins all have relative errors less than 0.10 with no zero bins

     8   passed the 10 statistical checks for the tally fluctuation chart bin result
         passed all bin error check:    14 tally bins all have relative errors less than 0.10 with no zero bins
```

the 10 statistical checks are only for the tally fluctuation chart bin and do not apply to other tally bins.

1tally fluctuation charts

	tally 6					tally 8				
nps	mean	error	vov	slope	fom	mean	error	vov	slope	fom
8000	8.6138E-05	0.0047	0.0185	2.8	1164765	4.5229E-03	0.0481	0.0035	10.0	10987
16000	8.6281E-05	0.0033	0.0075	5.2	1174900	4.4932E-03	0.0342	0.0018	6.5	10979
24000	8.6312E-05	0.0026	0.0044	10.0	1234859	4.5292E-03	0.0280	0.0012	3.3	10958
32000	8.6283E-05	0.0023	0.0034	10.0	1224697	4.6178E-03	0.0239	0.0009	2.4	11258
40000	8.6315E-05	0.0021	0.0028	10.0	1215549	4.6164E-03	0.0214	0.0007	2.5	11303
48000	8.6326E-05	0.0019	0.0023	10.0	1201724	4.6370E-03	0.0195	0.0006	2.8	11344
56000	8.6321E-05	0.0018	0.0021	10.0	1182300	4.6393E-03	0.0180	0.0005	4.1	11365
64000	8.6409E-05	0.0016	0.0018	10.0	1183462	4.6460E-03	0.0168	0.0004	8.0	11402
72000	8.6371E-05	0.0016	0.0015	10.0	1187350	4.6710E-03	0.0158	0.0004	10.0	11472
80000	8.6407E-05	0.0015	0.0014	10.0	1174052	4.6771E-03	0.0150	0.0003	8.6	11485
88000	8.6419E-05	0.0014	0.0012	10.0	1167691	4.7036E-03	0.0142	0.0003	7.5	11554
96000	8.6404E-05	0.0014	0.0011	10.0	1161158	4.7119E-03	0.0136	0.0003	5.6	11582
104000	8.6339E-05	0.0013	0.0010	10.0	1181898	4.7012E-03	0.0131	0.0003	4.2	11554
112000	8.6356E-05	0.0012	0.0009	10.0	1184461	4.7169E-03	0.0126	0.0002	4.3	11573
120000	8.6363E-05	0.0012	0.0009	10.0	1199715	4.6944E-03	0.0122	0.0002	4.1	11532
128000	8.6313E-05	0.0012	0.0008	10.0	1210982	4.6933E-03	0.0118	0.0002	3.9	11511
136000	8.6312E-05	0.0011	0.0008	10.0	1216575	4.6986E-03	0.0114	0.0002	3.5	11520
144000	8.6293E-05	0.0011	0.0007	10.0	1227995	4.6837E-03	0.0111	0.0002	3.4	11486
150000	8.6271E-05	0.0011	0.0007	10.0	1235330	4.6728E-03	0.0109	0.0002	3.3	11466

****

dump no. 2 on file runtpe nps = 150000 coll = 49804260 ctm = 0.73 nrn = 318764386

9 warning messages so far.

run terminated when 150000 particle histories were done.

computer time = 0.74 minutes

mcnp version 5 01232009 03/30/11 11:16:31 probid = 03/30/11 11:15:46

APPENDIX C
Elemental compositions used in simulations

Given below are the relevant tissue compositions used in the MCNP5 simulations given in this work. All data is referenced from Report 46 of the ICRU [13].

Table C-1 **Elemental composition of materials used in simulations** (% by mass)

Organ / Tissue	H	C	N	O	Na	P	S	Cl	K	Other
Blood	10.2	11.0	3.3	74.5	0.1	0.1	0.2	0.3	0.2	0.1 Fe
Skin	10.0	20.4	4.2	64.5	0.2	0.1	0.2	0.3	0.1	-
Muscle tissue	10.2	14.3	3.4	71.0	0.1	0.2	0.3	0.1	0.4	-
Bulk soft tissue	10.5	25.6	2.7	60.2	0.1	0.2	0.3	0.2	0.2	-

Given below are the different concentrations of gold used for each of the models used in this work. No gold concentration was assumed in normal tissue unless indicated below.

Table C-2 **Different gold concentrations used in simulations**

		Tumor volume	Other
Preliminary model	Source dependence	0.7 %	-
	Depth dependence	0.7 %	-
	Concentration dependence – Hainfeld values	0.7 %, 1.2 %, 3.0 %	-
Detailed model	Concentration dependence – Chithrani values	1.53 %, 2.77 %, 4.00 %	-
	Penetration (homogeneity) dependence	1.53 % [a]	0.44% (3.5:1 ratio) [b] 0.18% (8.5:1 ratio) [b]
		2.77 % [a]	0.79% (3.5:1 ratio) [b] 0.33% (8.5:1 ratio) [b]
	Specificity dependence	1.53 %	0.44% (3.5:1 ratio) [c] 0.18% (8.5:1 ratio) [c]

a. Concentration at tumor periphery; b. Tumor periphery to core ratio; c. Tumor to tissue ratio
1 % = 10 mg Au per kg of targeted tissue

APPENDIX D

Mass attenuation coefficients

Listed here are the mass attenuation coefficients for gold and tissue separately, followed by a comparison of the two over orthovoltage and low megavoltage photon energy levels. The tables below list the electron shell energies and Figs. D-1, D-2, and D-3 are plotted over the discussed energy range for easy visualization of the physical processes that dominate in each energy range. All attenuation coefficient data given below was obtained from [83].

Table D-1: Absorption edge energy and cross sections for pure gold

Energy (MeV)	Total attenuation cross section (cm^2/g)	Absorption edge
2.21E-03	9.94E+02	M5
2.29E-03	2.36E+03	M4
2.74E-03	2.54E+03	M3
3.15E-03	1.93E+03	M2
3.43E-03	1.65E+03	M1
1.19E-02	1.87E+02	L3
1.37E-02	1.76E+02	L2
1.50E-02	1.64E+02	L1
8.07E-02	8.90E+00	K

Table D-2: Absorption edge energy and cross sections for healthy tissue

Energy (MeV)	Total attenuation cross section (cm^2/g)	Absorption edge
1.07E-03	2.97E+03	K edge for Na
2.15E-03	4.39E+02	K edge for P
2.47E-03	2.96E+02	K edge for S
2.82E-03	2.06E+02	K edge for Cl
3.61E-03	1.02E+02	K edge for K

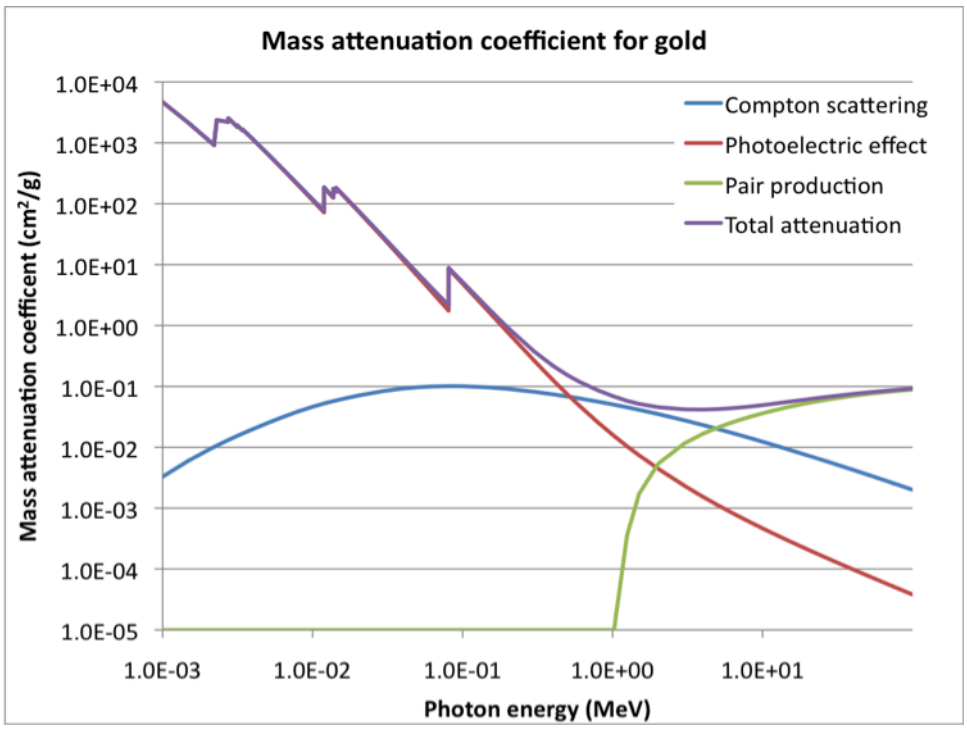

Figure D-1: Mass attenuation coefficients for gold separated by interaction type

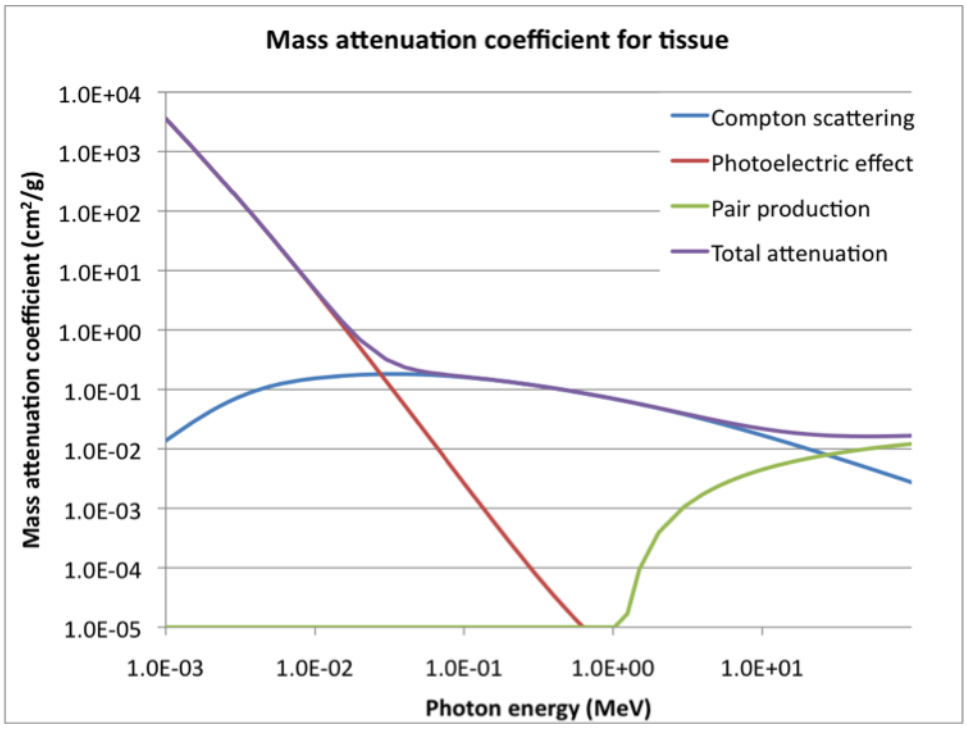

Figure D-2: Mass attenuation coefficients for tissue separated by interaction type

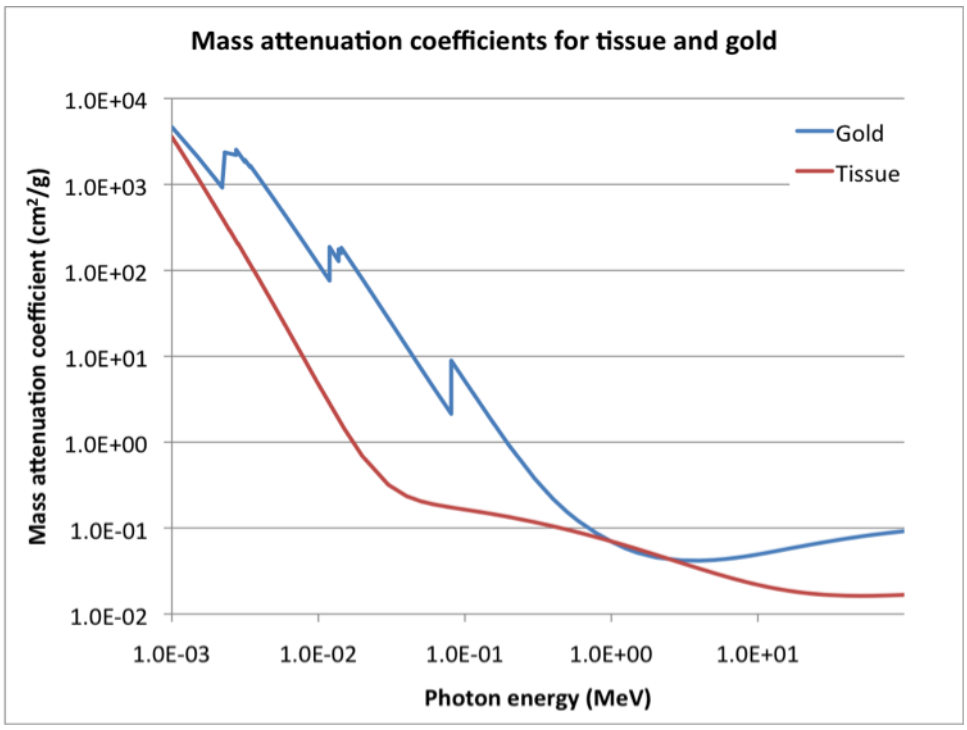

Figure D-3: Comparing mass attenuation coefficients for healthy tissue and gold

Discussion concerning the difference in attenuation coefficients for gold and tissue is included in Chapter 1. A brief mention was made at the end of Chapter 1 concerning the difference between the mass attenuation coefficient and the mass-energy absorption coefficient. The equation relating the two is reprinted here with the necessary equations for the g factors for the photoelectric effect, Compton scattering, and pair production available in [14].

$$\mu_{en}/\rho = (1-g)\mu_{tr}/\rho \qquad \text{(1-6 reprint)}$$

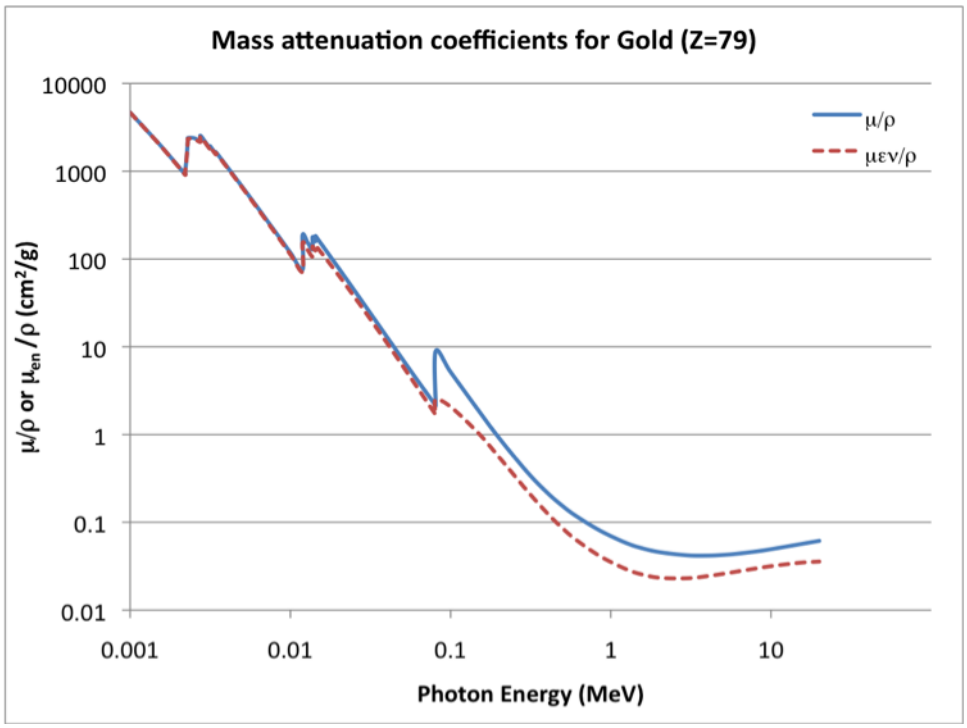

Figure D-4: Difference in mass attenuation and mass-energy absorption coefficients.

While the mass attenuation approximation is sufficient to understand the physical significance of the variables included in the model, the inherent error becomes apparent at photon energies between 100 keV and 10 MeV as shown in Fig. D-4. As a result, the radiation emitted, and the corresponding energy deposited, due to the secondary charged particles travelling through the medium cannot be ignored for microscopically accurate simulations. The work given here assumed macroscopic accuracy and ignored the effects of the *g* correction factor. Future work will need to be more accurate in order to make use of the modified F8 detector tally.

AUTHOR'S BIOGRAPHY

Nabeel Ahmed was born on June 22, 1984 in Ames, IA and grew up in Islamabad, Pakistan and Rockford, Illinois. He attended the University of Illinois at Urbana-Champaign and received a Bachelor of Science degree in Nuclear Engineering in 2006 with minor emphases in Chemistry and Biomedical Engineering. After graduation, Nabeel joined the 2006 Teach For America corps in Saint Louis and taught secondary mathematics at Beaumont High School for three years. He returned to Illinois for graduate studies and obtained his MS in Nuclear, Plasma, and Radiological Engineering in 2011. After completion of graduate work, Nabeel plans to pursue a career in the healthcare IT industry.